7-7-2020

Design of Materials and Processing Methods for High Temperature Composites

Chris Monteleone
University of Connecticut - Storrs, chris.monteleone@uconn.edu

Design of Materials and Processing Methods for High Temperature Composites

Chris Monteleone, Ph.D.

University of Connecticut, 2020

In this dissertation, various studies are described which seek to improve the properties of high temperature ceramic-matrix and carbon-matrix composites. Processes were developed and optimized to control the compositions, microstructures, and morphologies of ceramic materials. Focus was on the chemical vapor infiltration (CVI) of coatings on continuous fiber substrates. Other processes were involved as well, such as polymer impregnation & pyrolysis (PIP) and silicon melt infiltration (SMI). Both carbon and SiC fibers were used as substrates. Materials deposited using CVI include carbon, SiC, TiC, BN, and B_4C. Characterization methods include scanning electron microscopy, mechanical testing, X-ray diffraction, and others.

A brief introduction of high temperature composite materials is outlined in the first chapter. Chapter 2 explains how the CVI parameters for depositing TiC onto carbon fibers was optimized. The TiC layer serves to prevent chemical degradation of the fibers. In Chapter 3, carbon fibers are given different CVI coatings to explore ways of protecting them from molten silicon during the SMI process. BN was determined to be beneficial for providing protection and also improved mechanical properties. An effort was made in Chapter 4 to perform CVI of a mixed B_4C-Carbon matrix material to optimize thermal properties of carbon/carbon composites. Coatings with different compositions and structures were produced which may be useful for different applications of CMCs. A CMC with a ferromagnetic matrix was developed in Chapter 5 using the PIP method. This was done by dissolving cobalt salts in the preceramic polymer. The final chapter was devoted to suggesting how this work may be continued by future researchers to further improve these materials. Partial studies which show promise for CMC research are also presented.

Design of Materials and Processing Methods for High Temperature Composites

Chris Monteleone

B.S.E., University of Connecticut, 2014

A Dissertation

Submitted in Partial Fulfillment of the

Requirements for the Degree of

Doctor of Philosophy

at the

University of Connecticut

2020

Approval Page

Doctor of Philosophy Dissertation

Design of Materials and Processing Methods for High Temperature Composites

Presented by

Chris Monteleone, B.S.E.

Major Advisor _____
Steven L. Suib

Associate Advisor _____
S. Pamir Alpay

Associate Advisor _____
Rainer Hebert

University of Connecticut

2020

Acknowledgements

Great thanks are given to my major advisor, Dr. Steven Suib for providing me with the resources and connections necessary for completing this dissertation. He is truly an accomplished scientist, great leader, and someone I have much respect for.

Special thanks are given to my senior mentors Dr. Michael A. Kmetz and Dr. Tod Policandriotes. Both are extremely accomplished composites researchers who have provided me with much technical and personal support. Dr. Kmetz is responsible for pushing and inspiring me to pursue my graduate studies in this field. Dr. Policandriotes is responsible for providing me with the knowledge and experience to enter the CMC industry.

I would like to thank my advisory committee, Dr. S. Pamir Alpay, Dr. Rainer Hebert, Dr. Rajeswari M. Kasi, and Dr. Richard Parnas.

I would like to thank my graduate mentors, Dr. Timothy Coons, Dr. Justin Reutenaur, Dr. Samuel Frueh, and Dr. Gavin Richards for laying the foundation for the work that takes place in our lab. Dr. Richards was especially supportive as a liaison from Collins Aerospace by providing me with many research ideas and guiding my studies.

I would like to thank my fellow graduate students, Dr. Rebecca E. Gottlieb, Dr. Shannon Poges, Dr. Kenneth Petroski, Peter Kerns, Zachary Tobin, Jon Smolen, Pascal Riel Nathaniel Nisly, Seth Shuster, and Analyse Giordano. Especially Shannon and Ken who have gone to great lengths to prevent me from accidently harming myself and others.

I would like to thank my fellow Suib group members, especially Dr. Steven Murphy, Dr. Curtis Guild, and Jared Fee for assisting me in my studies. I would also like to thank my undergraduate assistant, Sean Purcell.

Special thanks are given to the people who continuously keep our lab running, machinist Dan Daleb and Chemistry Building managers Josh Strecker and Tyler Cardinal.

I would like to thank Collins Aerospace and Pratt & Whitney for funding and directing the work performed by myself and other students in the Suib research group.

Acknowledgement is given to the UCONN/Thermo Fisher Scientific Center for Advanced Microscopy and Materials Analysis (CAMMA).

Dedicated to my family,
Mom, Dad, Nick, Laurie, Jeff, Emily, and my grandparents

and to my friends,
Andrew, Greg, Morris, and my high school cross country teammates

Table of Contents

List of Figures

List of Tables

Chapter 1

Introduction

1.1 High Temperature Composites

In the past few decades of the modern history of composite materials, the field of high temperature (>800 °C) ceramic-matrix and carbon-matrix composites (CMCs) has steadily grown to a point of great real world and commercial value. We are at the onset of a time when CMCs will become a relatively common part of daily life in the forms of transportation, power generation, and more.

High temperature CMCs are advanced materials exhibiting combinations of properties which other materials have not been able to achieve. Compared to metals, ceramics are lightweight while still remaining mechanically strong. Unlike monolithic ceramics, reinforced CMCs have fracture toughness and can resist catastrophic failure. Better yet, they are able to maintain these impressive properties at temperatures beyond the capabilities of polymers and most metals, making them refractory materials [1-3]. As of now, CMCs are less established than these other classes of materials, difficult to manufacture, and costly.

Part of what gives CMCs their impressive properties are the components that they comprise. In general, CMCs are made up of strong reinforcing fibers which hold together a ceramic matrix. Without the fibers you would have a weak and brittle monolith. Without the matrix you would have loose unprotected fibers without structure. Oftentimes, the fibers are coated with thin films to control the fiber-matrix interface. These components are made of materials which can withstand extreme conditions such as borides, carbides, nitrides, and oxides. Two materials which stand out amongst the rest are carbon and silicon carbide.

Some of the first high temperature composites developed were carbon fiber reinforced carbon composites (C/C) [1]. NASA and the US military, which could afford the expensive material, found them quite useful in applications that demanded high temperature capabilities and low densities such as on rockets and missiles. They have also found commercial use as brakes in aircraft and high-end cars [4, 5]. In recent years, SiC/SiC and oxide/oxide CMCs have become highly sought after due to their oxidation resistance at high temperatures [2, 5, 6]. The jet engine industry, which has high commercial and military value, has been a massive driving force for the development of SiC/SiC composites. They are also being studied for use in nuclear power plants as high temperature radiation absorbing materials [7].

A number of methods have been used in the processing and manufacturing of CMCs. Carbon based pitches and polymers were used to make the original carbon fibers and matrices. This polymer-based approach is still commonly used today and has since been expanded for carbides and nitrides, especially SiC. Reactive melt infiltration (RMI) is another liquid-based approach which involves the reaction between a molten metal or alloy and carbon. Chemical vapor deposition (CVD) is a more advanced method, which can be used to grow ceramic films from the decomposition of gases and vapors. Solid ceramic precursors can be used as well, such as powders, slurries, and gels, which can be sintered together.

1.2 Continuous Fibers

Fibers of all aspect ratios have been used in composite materials, but continuous fibers which span the length and width of the CMC part provide the most strength. They are the most common type of fiber considered for use in high temperature structural applications and the only type discussed in this dissertation. Fibers are the load-bearing component of the CMC and need to be properly protected from mechanical, thermal, and chemical degradation. Cracks which

form in the matrix should be halted at the fiber. Common materials used for ceramic fibers are carbon, SiC, and alumina. Boron and silicon nitride fibers have been encountered as well. Carbon is impressively strong and thermally resistant, but can start to oxidize around 450 °C [4, 5, 8-10]. Alumina fibers are essentially oxidation-proof, but have poor creep resistance at elevated temperatures [1]. SiC provides a good balance of strength, thermal stability, and oxidation resistance [1, 6].

Ceramic fibers range in diameter ~5-15 μm. They are spun and bundled together into fiber tows of hundreds to thousands of fibers. The fibers are often held together by a polymeric sizing to keep them from fraying before use. The tows can be woven into 2-D textile fabrics used to make multilayered composites. Tows and fabrics can also be made into 3-D fiber preforms. The weave pattern and preform architecture can have a strong influence on the mechanical properties of the composite, especially in the tensile and shear directions. This system of bundled fibers and woven tows creates a multi-modal distribution of pores throughout the composite. Narrow pores are seen between the fibers and larger pores between the tows [1]. Poorly constructed preforms can also have large pores between fabric layers resulting in low shear strength and delamination of the composite. Pore size control is important for proper matrix infiltration.

1.3 Ceramic and Carbon Matrices

The ceramic matrix is regarded as mechanically weak compared to the fibers, but is necessary to transfer the load between fibers. Cracking in the matrix is unavoidable during use and even during fabrication from mechanical and thermomechanical stresses. As long as the fibers remain intact, the composite will maintain its strength. Carbon and SiC matrices should

have minimal porosity to maximize the mechanical properties of the CMC [2, 11]. In oxide matrices such as alumina, porosity is unavoidable so this must be controlled [3].

The matrix acts as a layer of defense to the fibers. It shields them from oxidation, oftentimes by becoming oxidized itself. A SiC matrix is expected to oxidize to form silica to some extent. A silica passivation layer can build up and minimize further oxidation of the matrix and fibers [2, 12]. Sometimes an environmental barrier coating (EBC) made of silica or other materials is manually applied to the outside of the composite during fabrication. This is especially important for a carbon matrix, which oxidizes at a lower temperature into CO and CO_2 rather than building up its own passivation layer. Additives are sometimes included in the matrix for various reasons. For example, crystalline SiC particles can be used to encourage proper crystalline growth of the matrix when applied. Other additives can provide thermal and mechanical benefits to the material.

1.4 Interphase Coatings and Fracture Toughness

The bond between fiber and matrix is important to control for providing fracture toughness to the CMC as a whole. If the two components are bound together too strongly then cracks in the matrix can easily propagate through the fibers, making the CMC brittle. Thin film interphase coatings are often applied to the fibers to control this interfacial bond [9, 13]. This is most commonly done using CVD. The interphase coatings give rise to certain toughening mechanisms, which give the material its fracture toughness. These include crack deflection, crack splitting, and fiber pull-out, which are shown in **Figure 1.1** [13]. When a matrix crack reaches the fiber, the interphase coating provides a path for which the crack can travel more easily around or along the fiber. The weak bond from the interphase coating allows the matrix to separate from the fiber more easily than a crack going through the fiber. Crack deflection occurs

when the crack is redirected towards a different path. Crack splitting is when multiple smaller cracks are created from the original crack. The longer path length around the fiber perimeter means energy is absorbed that would have otherwise propagated the crack farther into the CMC. Energy is also absorbed by debonding of the fiber and matrix. The fiber is left intact and the crack length has been shortened. When fibers do break, they are then able to slide out from their position in the matrix relatively easily in a process known as fiber pull-out. This sliding results in the absorption of frictional energy, again minimizing the effect of cracks.

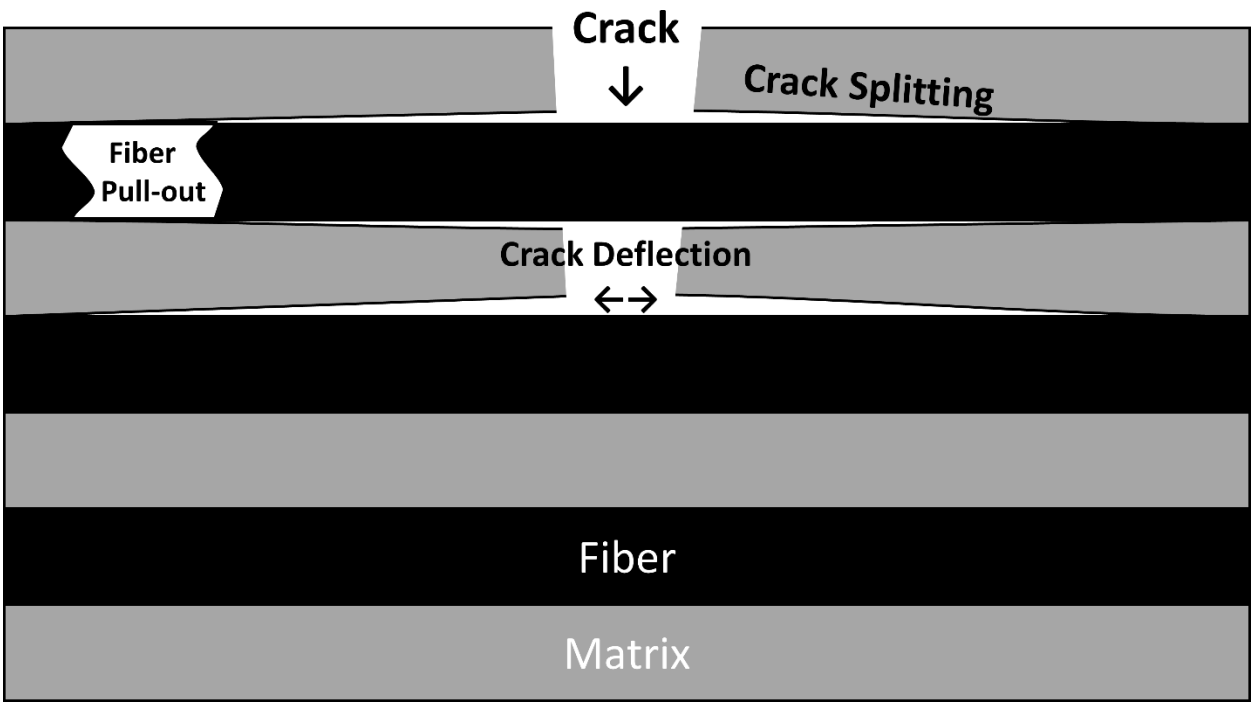

Figure 1.1 Diagram of CMC toughening mechanisms.

The two most common fiber interphase coatings are pyrolytic carbon (pyC) [9, 14, 15] and hexagonal boron nitride [9, 13, 16]. PyC has a similar structure to graphite, but with more microstructural disorder and its graphene planes are covalently bonded together. The graphitic structure allows the 2-D planes to separate and slide relatively easily, which weakens the bond

between the fiber and matrix. Unfortunately, when the pyC oxidizes voids are left behind, which weakens the CMC. Hexagonal BN also has a graphitic structure that is able to provide the same benefit as pyC. However, BN is more oxidation resistant than pyC and decomposes into solid B_2O_3 which can act as a passivating layer to protect the fiber and prevent further oxidation [9, 10]. Both materials are relatively elastic compared to SiC and carbon fibers making them less brittle [13].

In the case of oxide CMCs, interphase coatings are often not used. Instead, cracks are dealt with by controlling the size and distribution of pores in the matrix [3]. When a crack meets a pore the crack energy is distributed around the outside of the pore, similar to how cracks are split around the fibers in non-oxide CMCs. A higher pore curvature maximizes this effect, so they should be as close to spherical as possible. Pores should be homogeneously distributed for optimal performance throughout the material. Oxide interphase coatings have been used before, such as monazite, scheelite, and ZnO [3, 17]. The main purpose is to prevent the alumina fibers and alumina matrix from bonding together at elevated temperatures through grain growth.

Interphase coatings can be used for chemical protection of the fibers as well [8, 10, 13, 14]. Duplex interphase coatings consisting of both BN and SiC thin films have been demonstrated to increase oxidation resistance of the fiber. Boron oxide from the BN and silica from the SiC together form borosilicate glass [10]. This material will melt at elevated temperatures and flow into cracks, thereby sealing in the fibers from oxygen. Borosilicate is also known to have a low coefficient of thermal expansion, so less thermomechanical stress arises from heating and cooling of the CMC. Chemical attack of the fibers can also come from the processing methods. Many CVD precursors and byproducts are corrosive towards carbon fibers,

such as HCl gas [9]. Carbon fibers may be coated with pyC prior to other coating processes to both act as a chemical barrier and provide toughness to the composite [14].

1.5 PIP and Pre-Ceramic Polymers

Polymer infiltration & pyrolysis (PIP) is a method of producing ceramic matrices in which a pre-ceramic polymer is infiltrated into a fiber preform, often using vacuum suction. The polymer is then chemically and/or thermally cured into a solid to produce a "green-body" composite. The green composite is then heated to higher temperatures to pyrolyze the polymer into a ceramic. At this point a very porous matrix has been produced. Many voids are left behind from the evolution of solvents and decomposition gases during the curing and pyrolysis steps. Multiple infiltration/cure/pyrolysis cycles are performed until the density of the CMC is maximized [1, 2].

PIP is a relatively simple process that allows for a lot of control. The polymer concentration can be controlled by using more or less solvent to optimize the viscosity for the part being infiltrated. This allows large and/or complex parts to be adequately infiltrated [15]. Unfortunately, a fully dense CMC cannot be achieved by PIP alone since voids are always left behind [11]. For this reason, it is important to maximize the ceramic yield of the polymer, or the mass percentage of the ceramic produced from the polymer used. Polymer slurries can also be made using powders in order to minimize the void space. It is sometimes possible to fill in the remaining porosity using other matrix fabrication methods.

Pre-ceramic polymers have been developed for the synthesis of carbon, SiC, Si_3N_4, BN, and other matrices [1, 2, 4, 15, 18-20]. Most organic polymers will decompose into carbon at some temperature, so many polymers are available for carbon composites. Common examples are pitches, phenolics, furan resins, polyimides, polyarylacetylenes, and polyphenylenes [1, 4].

SiC and Si_3N_4 producing pre-ceramic polymers are typically inorganic in nature, meaning they contain silicon in the backbone. The most commonly used SiC polymers are polycarbosilanes, which alternate Si and C in the backbone [2, 15]. Different organic side groups can be used to alter the properties of the polymer and the resulting SiC material. Amorphous SiC is produced at pyrolysis temperatures <1100 °C. Subsequent annealing steps up to 1500-1600 °C are required to crystallize the SiC to the β phase. Polysilazanes and polycarbosilazanes, which alternate Si and N in the backbone can be pyrolyzed into SiC, Si_3N_4, or SiCN depending on pyrolysis conditions [2, 20].

1.6 Chemical Vapor Deposition

Chemical vapor deposition (CVD) is a process used in multiple industries but it goes hand in hand with CMCs. CVD is a broad category of techniques involving the decomposition and/or reactions of gases to deposit a new material onto a substrate. The term CVD is usually used when the substrate is an external surface. Chemical vapor infiltration (CVI) is a subset of CVD involving the deposition of material into a porous substrate, such as fiber preforms. Epitaxy, a way of controlling crystallinity, is another variation in which the deposited material takes on the crystal structure of the substrate. Atomic layer deposition (ALD) is the CVD of a monolayer of material. Various types of CVD have been developed according to the control of parameters. Isothermal CVD refers to a process done at a single temperature, but temperature gradient CVD is possible as well. Similarly, isobaric and pressure gradient CVD have been done before. Plasma-enhanced and microwave plasma-enhanced CVD refers processes in which the precursor gases are ionized. Laser CVD involves the use of EM radiation to assist in the breakdown of gases [2].

Many materials can be produced using CVD including metals, ceramics, glasses, polymers, semiconductors, graphene, diamond, etc. Common CVD precursors are halides and hydrides of the material being deposited, amongst others. Room temperature liquids can be used by evaporating them or carrying the vapors by bubbling a carrier gas [2]. The CVD of carbon can be done using a wide variety of hydrocarbons [1]. Natural gas, methane, propane, and propylene are some more common carbon precursors due to their availability. For SiC, a very common precursor is methyltrichlorosilane (MTS) [2, 21]. It has the benefit of being a "single source" precursor, so the silicon and carbon both come from the MTS molecule which simplifies the process. CVD of SiC can also be done using silane or halogenated silanes with hydrocarbons. High purity SiC with good microstructural properties and high crystallinity can be produced using CVD at relatively low temperatures (<1100°C). BN is also produced using CVD, typically using boron trichloride and ammonia [9, 13, 16]. Without the enhancement of plasmas, etc. it is difficult to deposit a highly crystalline hexagonal BN. BN is typically turbostratic, which is similar but involves more disorder amongst the 2-D BN planes. In CMCs, both interphase coatings and matrix materials can be deposited using CVI.

A CVD setup can involve a lot of complex and expensive equipment [2]. At the heart of it is a heated environmentally controlled chamber. The type of heating can fit into two categories, hot wall or cold wall. A hot wall furnace is resistively heated, which heats the gases directly. A cold wall furnace heats the substrate directly and gases do not become hot until they reach the substrate surface. This can be done using magnetic induction, current through conductive substrates, or EM radiation. Gas flow into the chamber involves many components such as pressure regulators, valves, flow controllers, and leak-resistant tube fittings. Most CVD reactions are done at low pressure, which involves a vacuum pump. Pressure can be controlled

using a combination of pressure transducers and control valves. CVD parameters than can be controlled are temperature, pressure, and gas flow rates. These can have strong influences on the deposited material such as deposition rate, morphology, microstructure, crystallinity, stoichiometry, etc. A common problem encountered in the CVI of matrix materials is the "canning-off" of pores, which leaves behind sealed in, inaccessible porosity in the CMC [11]. This blockage of pores is a result of the multi-modal distribution of pore sizes in fiber preforms. Canning-off can be minimized by optimizing the preform architecture and reducing deposition rate, but canning-off is usually unavoidable. CMC machining can be done in between CVI steps to open up surface porosity.

1.7 Reactive Melt Infiltration

RMI is a relatively new method of CMC matrix fabrication [2, 4, 11, 22]. RMI starts with the PIP or CVI infiltration of a fiber preform with a porous carbon layer. Molten metal or alloy is then wicked into the preform to react with the carbon, forming a metal carbide matrix. This was first demonstrated with SiC using silicon melt (SMI) [11]. RMI has also been done using zirconium, molybdenum, niobium, etc. This method is able to achieve low matrix porosity due to the good wetting characteristics between metals and metal carbides and the volume expansive reaction that takes place. However, this method suffers from the presence of unreacted carbon and/or metal. Additionally, the high temperatures required to melt the metals can be damaging to the fibers, especially carbon fibers, which can react with the metals.

1.8 Objectives of this Work

In this dissertation, key shortcomings of CMCs including their materials and processing are targeted for improvement. Chapters 2 and 3 focus on developing and identifying fiber interphase coatings, which are used to protect carbon fibers, particularly during matrix infiltration. Chapters 4 and 5 seek to enhance the capabilities of ceramic matrices beyond what they have already been proven to do. The final chapter is a collection of partial studies, which are considered important and valuable to the field and may be continued by future researchers. These include CVI processing conditions, CVI byproducts analyses, pre-ceramic polymer synthesis, and post-CVI materials processing.

Chapter 2

Atmospheric Pressure Chemical Vapor Infiltration of a Titanium Carbide Interphase Coating on Carbon Fiber

2.1 Introduction

Carbon fibers are highly desired for use in composite materials due to exceptionally high strength, Young's modulus, and thermal conductivity as well as low density and coefficient of thermal expansion [23-26]. These composite materials are being developed for many industries, including aerospace and nuclear power where they see high temperatures in oxidizing conditions. Carbon is considered a high temperature material, but in oxidizing environments degradation will begin around 400 °C [10]. Furthermore, molten metals such as magnesium, aluminum, and silicon, which are used in the fabrication of metal and ceramic matrix composites are reactive towards carbon fibers. As the primary load bearing component of composites, it is important to maintain the integrity of these fibers. This is why a lot of focus has gone towards developing high temperature protective interphase coatings for carbon fibers.

One such coating is titanium carbide (TiC)—a material typically regarded for having remarkably high hardness. TiC is thermally stable in excess of 3000 °C and chemically stable with most molten metals [27]. TiC coatings on carbon fiber inhibit fiber oxidation and promote wetting by molten metals for improved interfacial properties [10, 28]. Unfortunately, these benefits come at the cost of diminished tensile strength of the fiber [28, 29]. The synthesis of thin-film TiC coatings on carbon fiber has been done by means of chemical vapor infiltration (CVI) [8, 30, 31] and molten salt synthesis (MSS) [29, 32] methods. TiC CVI from a $TiCl_4$

precursor has been disparaged for having high temperatures which can degrade fibers, lengthy reaction times, and for the cracked and poorly adhered coatings produced on carbon fiber substrates [10, 28, 31]. Baklanova et al. [8] reported on a reactive-CVI method in which CF_4 converts titanium to TiF_n gases, which then react with the carbon in the fibers at 927-1027 °C for 0.5 hours to form a TiC coating. This resulted in a uniform, crack-free coating with good fiber adhesion, but the coating suffered from titanium silicide contamination from the walls of the quartz reaction vessel. Additionally, the fluorinated species in the reaction are known to produce toxic HF on contact with water. Li et al. [32] first demonstrated the MSS of TiC on carbon, in which titanium metal was dissolved in a 900-950 °C molten salt mixture (KCl, LiCl, KF). Fibers were immersed in the solution for 1-5 hours while the titanium reacted with the carbon on the fiber surfaces before the solution was cooled and residual salt was removed by washing. This produced a smooth, crack-free coating with controllable thickness. This method has been reproduced by Wang et al. [29].

The common ground between the reactive-CVI and MSS methods is that both form TiC using carbon from the fiber surface. This results in good coating-fiber adhesion, but the fiber is weakened in the process. Degradation to the fibers (which are the load-bearing component of continuous fiber composites) should be avoided, especially since the purpose of these coatings is to protect the fibers from attack by molten metals. Furthermore, the quality of the coating will depend on the condition of the carbon in the fiber and that different brand fibers will produce coatings of varying morphology, stoichiometry, crystallinity, etc. This also restricts the possibility of other fiber surface treatments, such as additional interphase coatings that may be applied prior to the TiC coating. TiC CVI from a $TiCl_4$ precursor uses methane as the carbon

source, so these drawbacks are not present. Instead of converting the surface layer from carbon to TiC, the TiC coating is grown from the fiber surface outward.

In this work, the $TiCl_4$-based CVI approach was revisited to see if the reported drawbacks could be overcome. The coatings were deposited at atmospheric pressure, which simplifies the CVI setup. Coating times and temperatures should be comparable to reactive-CVI and MSS methods to remain competitive. The goal is to produce a TiC coating that is smooth, uniform, stoichiometric, and crack-free while fully covering the carbon fibers. The CVI parameters were optimized to control these coating properties. Finally, the tensile strengths were measured with and without the coating.

2.2 Experimental

2.2.1 Materials

Titanium (IV) chloride ($TiCl_4$, 99.0%) was purchased from Alfa Aesar. Hydrogen (H_2, ultra-high purity, 99.999%) and methane (CH_4, ultra-high purity, 99.99%) were purchased from Airgas. The substrate used for all depositions was T300 ex-PAN 3K continuous carbon fiber supplied by TORAYCA®.

2.2.2 TiC CVI

The $TiCl_4$ precursor was stored in an air-free glass bubbler and warmed to 50 °C with heating tape. Hydrogen and methane flow rates were controlled using digital mass flow controllers. Hydrogen bubbled through the $TiCl_4$ and into a 2.5 cm OD quartz tube, which was heated by a horizontal tube furnace. The methane flow intersected the hydrogen/$TiCl_4$ flow before entering the quartz tube. Heating was done at 20 °C/min under flowing hydrogen. The quartz tube was lined with graphite foil and carbon fiber substrates were loaded inside. Exhaust

gases were flowed through a hydrocarbon oil bath followed by a 1 M solution of sodium hydroxide. This setup can be seen in **Figure 2.1**.

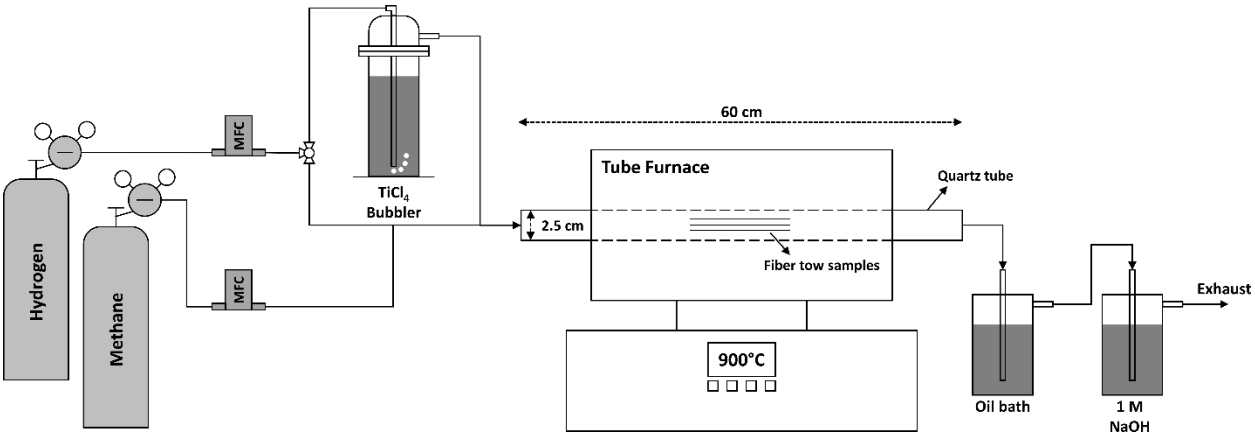

Figure 2.1 Diagram of TiC CVI reactor setup.

In order to optimize the TiC coating, the following CVI parameters were independently varied: temperature, total flow rate (sum of hydrogen and methane flow rates), and flow ratio (the ratio of hydrogen flow rate to methane flow rate). The temperature optimization was done first by performing runs between 750 °C and 1050 °C. The total flow rate was then optimized by using the previously determined optimal temperature and varying the flow from 37.5 to 150 standard cubic centimeters per minute (sccm). The final optimization of the flow ratio was done by using the other two optimized parameters and varying the ratio from 1:2 to 4:1 sccm H_2/sccm CH_4.

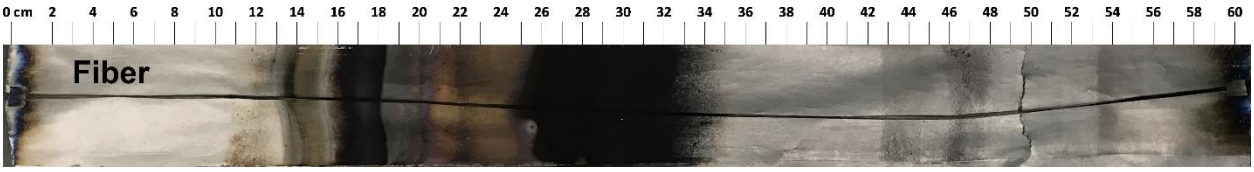

Figure 2.2 Image of the graphite foil liner showing the deposition profile after TiC deposition. The deposition zone is the dark area from 25-34 cm.

After each deposition, the coated fibers were removed from the quartz tube for sample preparation. The best TiC coatings were typically produced within a ~10 cm region in the center of the furnace, referred to as the *deposition zone* (**Figure 2.2**). Multiple cross-sectional samples of the coated fibers were taken along the deposition zone for scanning electron microscopy (SEM) analysis. The SEM micrographs were used to observe the morphology and quality of the coatings.

2.2.3 Characterization

Micrographs of the coated fibers were taken using a ThermoFisher TeneoLoVac Field Emission SEM operated at 10-20 kV and 0.4 nA. Qualitative elemental analysis was performed using Energy Dispersive X-ray Spectroscopy (EDS) with EDAX Team^{TM} software. X-ray diffraction patterns were obtained using a Rigaku Ultima IV diffractometer (Cu Kα radiation, λ = 1.5406 Å) with an operating voltage of 40 kV and a current of 44 mA. Transmission electron microscope (TEM) images were taken with a ThermoFisher Talos 200 S/TEM. TEM samples were prepared using a ThermoFisher Helios Nanolab 460F1 Focused Ion Beam (FIB) equipped with a Ga-ion column and Multi-Chem Pt protective cap depositor. The TEM was equipped with a selected area electron diffraction (SAED) detector used to analyze the coating crystallinity.

2.2.4 Tensile Testing

Coated fiber tows were tensile tested using an Instron® 5869 universal testing system equipped with a ±50 kN load cell. Fiber tow samples with a 2.5 cm gage length were epoxy mounted on cardstock to allow for better gripping (**Figure 2.3**). Samples were sprayed with an acrylic binder to ensure that all fibers in the tow broke simultaneously. Testing was done at a rate of 0.5 cm/min until failure.

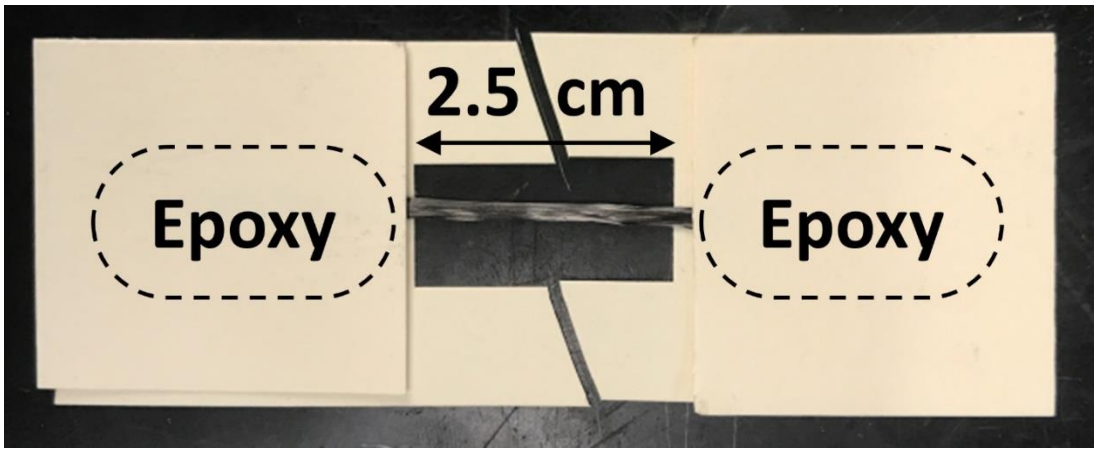

Figure 2.3 Fiber tow specimen prepared for tensile testing.

2.3 Results

An initial run of TiC deposition was performed on T300 carbon fiber at 1050 °C for 30 minutes flowing 120 sccm H_2 through the $TiCl_4$ bubbler and 100 sccm CH_4 directly to the furnace. Cross sectional samples were taken from the front, middle, and back of the coated fiber for SEM microscopy, seen in **Figure 2.4a-c**. The micrographs reveal a material deposited onto the fiber that appears crystalline. The front section was coated much more than the middle and back sections, however uncoated gaps of fiber can still be seen all over. The individual crystals exhibit a tetrahedral morphology, which gives the coating a high degree of roughness and inconsistency.

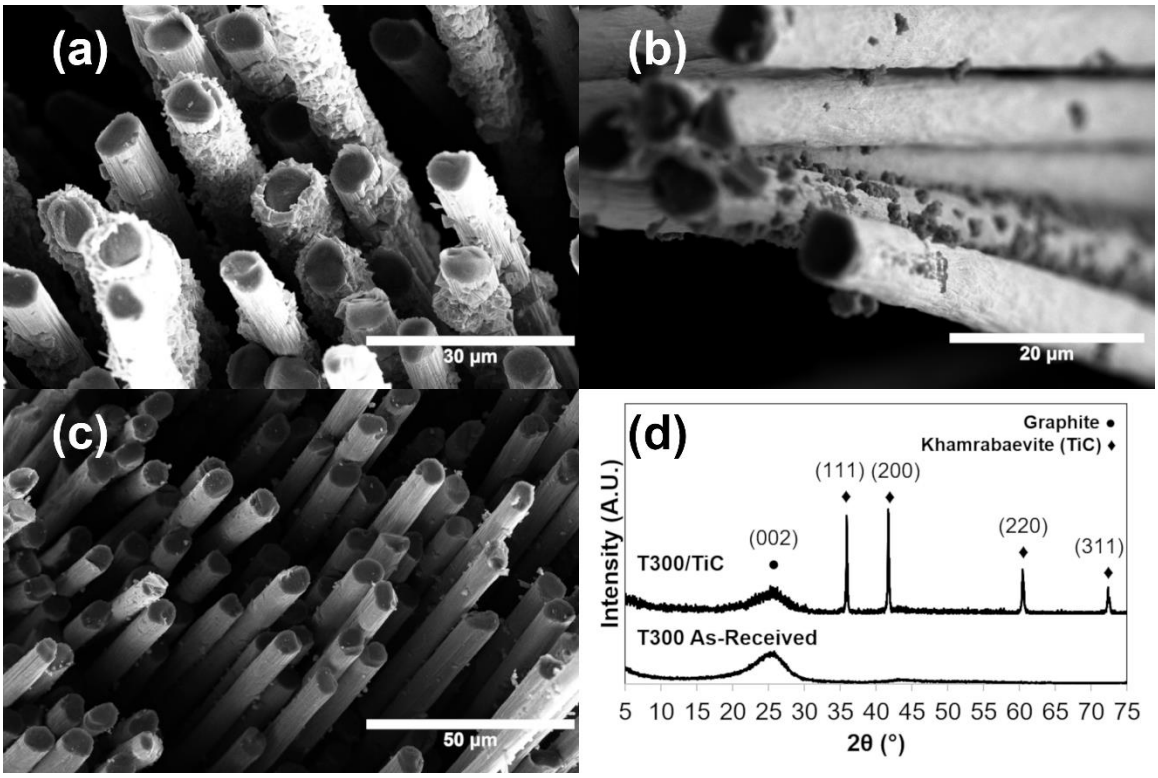

Figure 2.4 Results from a preliminary deposition of TiC onto carbon fiber before CVI parameters were optimized. (a-c) SEM micrographs from various parts of the fiber tow showing a sparse crystalline coating on the fibers. (d) Powder X-ray diffraction patterns of the as-received carbon fiber and TiC-coated carbon fiber before optimizing CVI parameters.

Powder X-ray diffraction was then used to compare the structure of the coated fiber to that of as-received T300 fiber (**Figure 2.4d**). The as-received fiber showed very little crystallinity, with a broad reflection around 26° that roughly correlates to graphite. The coated fiber pattern showed the same broad graphite reflection around 26° plus four sharp reflections at 35.9°, 41.7°, 60.5°, and 72.4° which correlated to khamrabaevite (TiC) [33].

2.3.1 Temperature Optimization

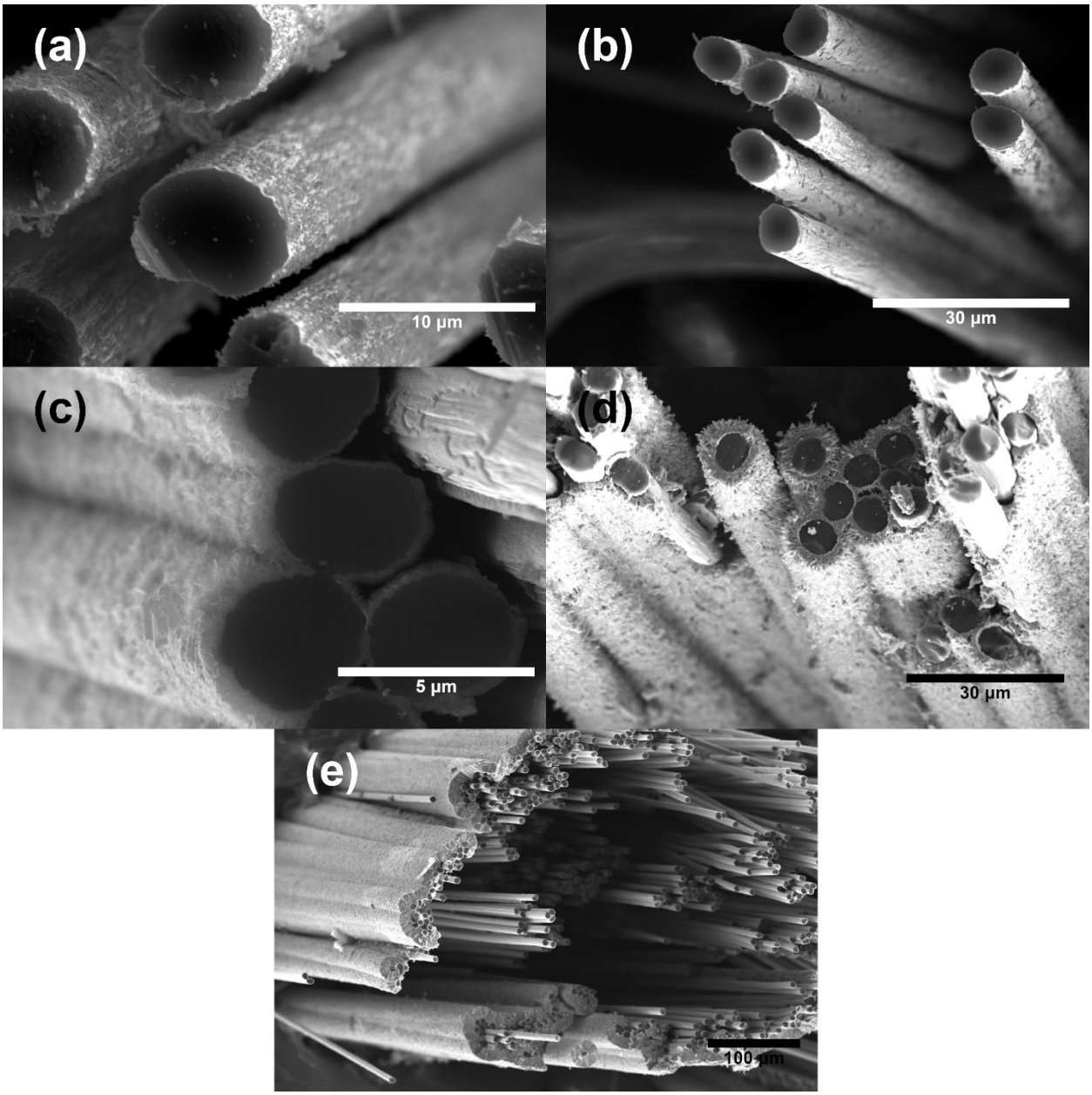

Figure 2.5 SEM micrographs from the temperature optimization study. TiC depositions done at (a) 750 °C (b) 850 °C (c) 900 °C (d) 950 °C and (e) 1050 °C. The chosen optimum temperature was 900 °C due to the coating morphology and consistency in coating thickness.

TiC was coated at 750, 850, 900, and 1050 °C. For each deposition, the total flow rate and flow ratio of sccm H_2/CH_4 were kept constant at 150 sccm and 2:1, respectively. SEM micrographs showed that the lower temperature depositions (750 °C, **Figure 2.5a** and 850 °C, **Figure 2.5b**) produced coatings with sparse coverage and poor adhesion within the deposition zone. At 900 °C (**Figure 2.5c**) the coatings throughout the deposition zone exhibited full fiber coverage, great fiber adhesion (coating was not flaking off), and uniform thickness. The coating was relatively smooth at the front of the deposition zone, but quite rough within the bulk of the deposition zone with TiC needles protruding from the surface. At 950 °C (**Figure 2.5d**) much of the coating displayed a high degree of roughness and porosity due to large spike-shaped crystals. The thickness was not consistent throughout the deposition zone, so some fibers had too thick of a coating which caused a fiber-bridging effect, and some fibers were inadequately coated with large gaps of exposed fiber. Still, the coating was well-adhered to the fiber. In the highest temperature deposition (1050 °C, **Figure 2.5e**) the bulk of the coating was only on the outer fibers, creating a shell of coating around the fiber tow and sealing in the inner fibers. The coating was made up of large tetrahedral grains, which gave a rough appearance on the surface. The 900 °C deposition gave the best quality coatings, so 900 °C was selected as the optimized temperature.

2.3.2 Total Flow Rate Optimization

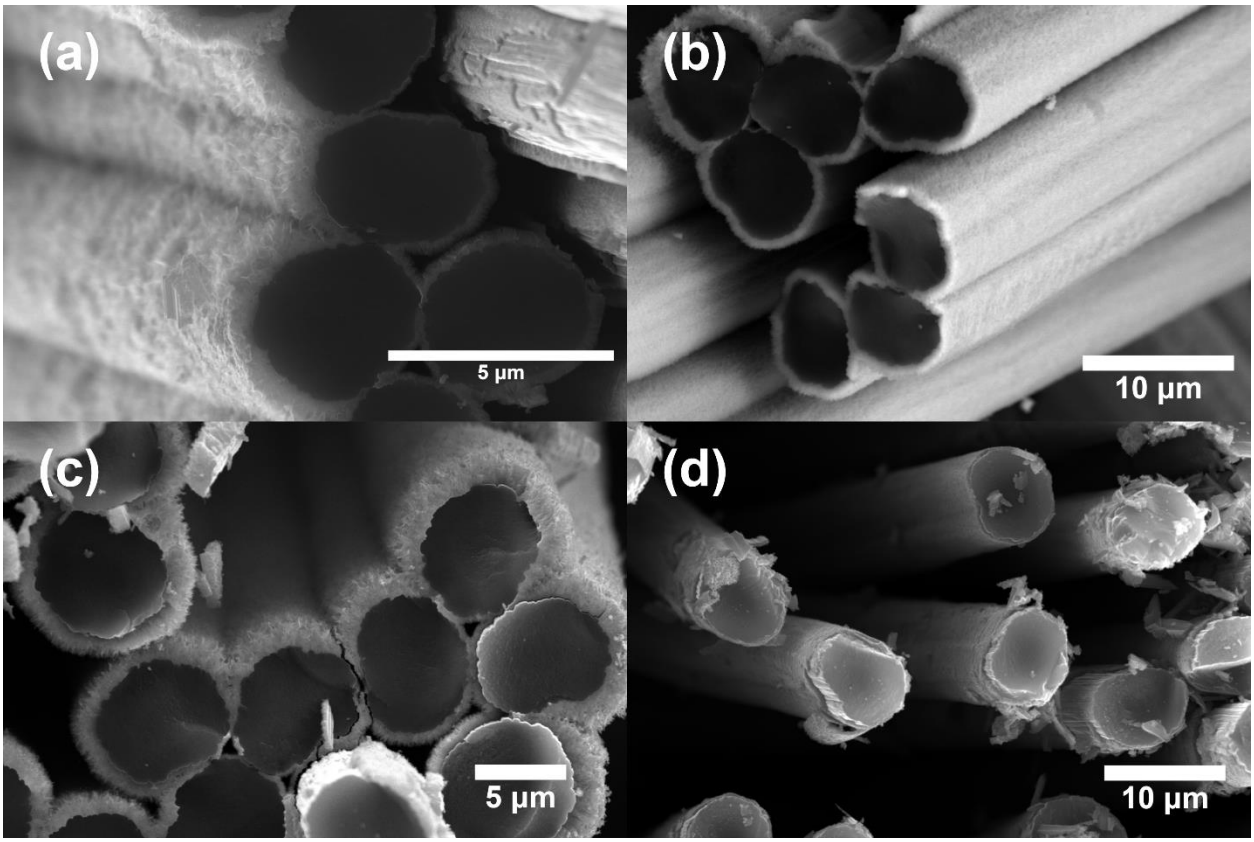

Figure 2.6 SEM micrographs from the total flow rate study. TiC depositions done with (a) 150 sccm (b) 112.5 sccm (c) 75 sccm and (d) 37.5 sccm total gas flow. The chosen optimum flow rate was 37.5 sccm due to the smoother morphology in the coating.

The total flow rate was the sum of the flow rates of the two process gases (H_2 and CH_4) measured in the mass flow unit of standard cubic centimeters per minute (sccm). Depositions were performed with flow rates of 150, 112.5, 75, and 37.5 sccm. The temperature was kept constant at the optimized value of 900 °C and the flow ratio was kept constant at 2:1 sccm H_2/CH_4. The 150 sccm deposition (**Figure 2.6a**) was described previously in **Section 2.3.1** as having good fiber coverage, fiber adhesion, and thickness consistency, but high roughness in many spots. Lowering the flow to 112.5 sccm (**Figure 2.6b**) reduced the roughness of the coating and increased uniformity throughout the deposition zone. This effect was supported by

the 75 and 37.5 sccm (**Figure 2.6c-d**) depositions—the coatings became smoother and the morphology was more consistent throughout. Thus, the lowest flow rate of 37.5 sccm was selected as the optimized total flow rate.

2.3.3 Flow Ratio Optimization

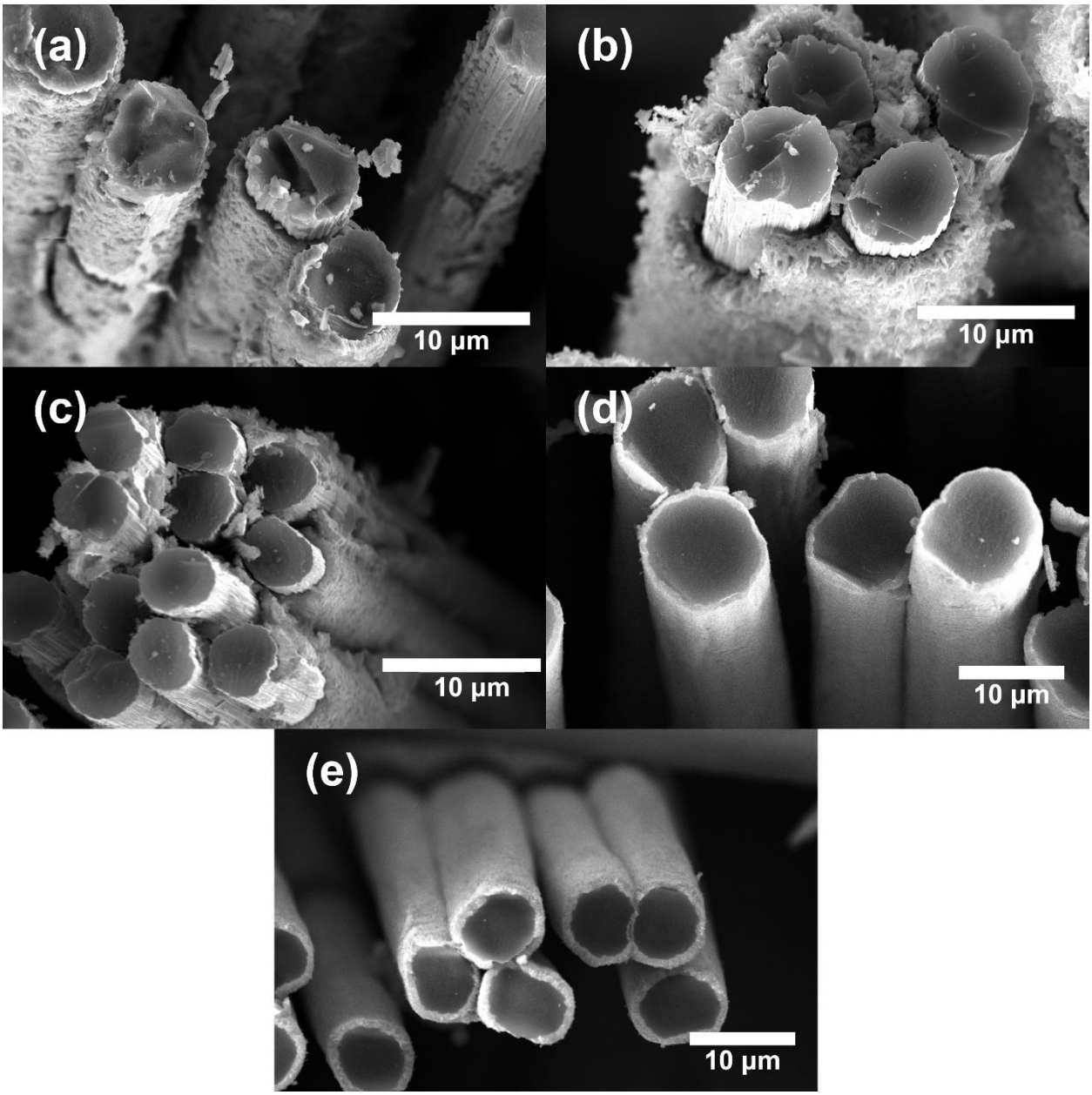

Figure 2.7 SEM micrographs from the flow ratio study. TiC depositions done with H2/CH4 flow rate ratios of (a) 1:2 (b) 1:1 (c) 2:1 (d) 3:1 and (e) 4:1. The optimal ratio was 4:1 due to the smooth coating morphology and the lack of fiber bridging.

The last parameter to be optimized was the flow ratio of sccm H_2 to sccm CH_4. This parameter also indirectly represents the ratio of $TiCl_4$ to CH_4 entering the reactor since H_2 is the carrier gas for $TiCl_4$. The ratios tested were 1:2, 1:1, 2:1, 3:1, and 4:1 sccm H_2/CH_4. The temperature and total flow rate were kept constant for each deposition at the previously optimized values of 900 °C and 37.5 sccm, respectively. With a ratio of 1:2 (**Figure 2.7a**) the coating had poor fiber coverage and adhesion. Much of the fiber surface was left exposed. Flakes of coating were seen hanging from the fiber surfaces, demonstrating a weak fiber-coating bond. The 1:1 deposition (**Figure 2.7b**) had similar results as 1:2, but also had a shell of coating around the outside fibers, sealing in the inner fibers. Many fibers were bridged due to this effect. At 2:1 **Figure 2.7c**, previously discussed in **Section 2.3.2**) there was no longer a shell of coating around the fibers, each fiber was completely coated, and coating adhesion improved, evidenced by fewer flakes of coating hanging from the fiber surfaces. However, a good deal of fiber bridging was seen, creating fiber bundles of 3-20 fibers. The 3:1 and 4:1 depositions (**Figure 2.7d-e**) both showed much improvement in coating coverage, adhesion, and bridging. The higher ratios yielded higher quality coatings, so 4:1 was selected as the optimized ratio.

2.3.4 Analysis of the Optimized Coating

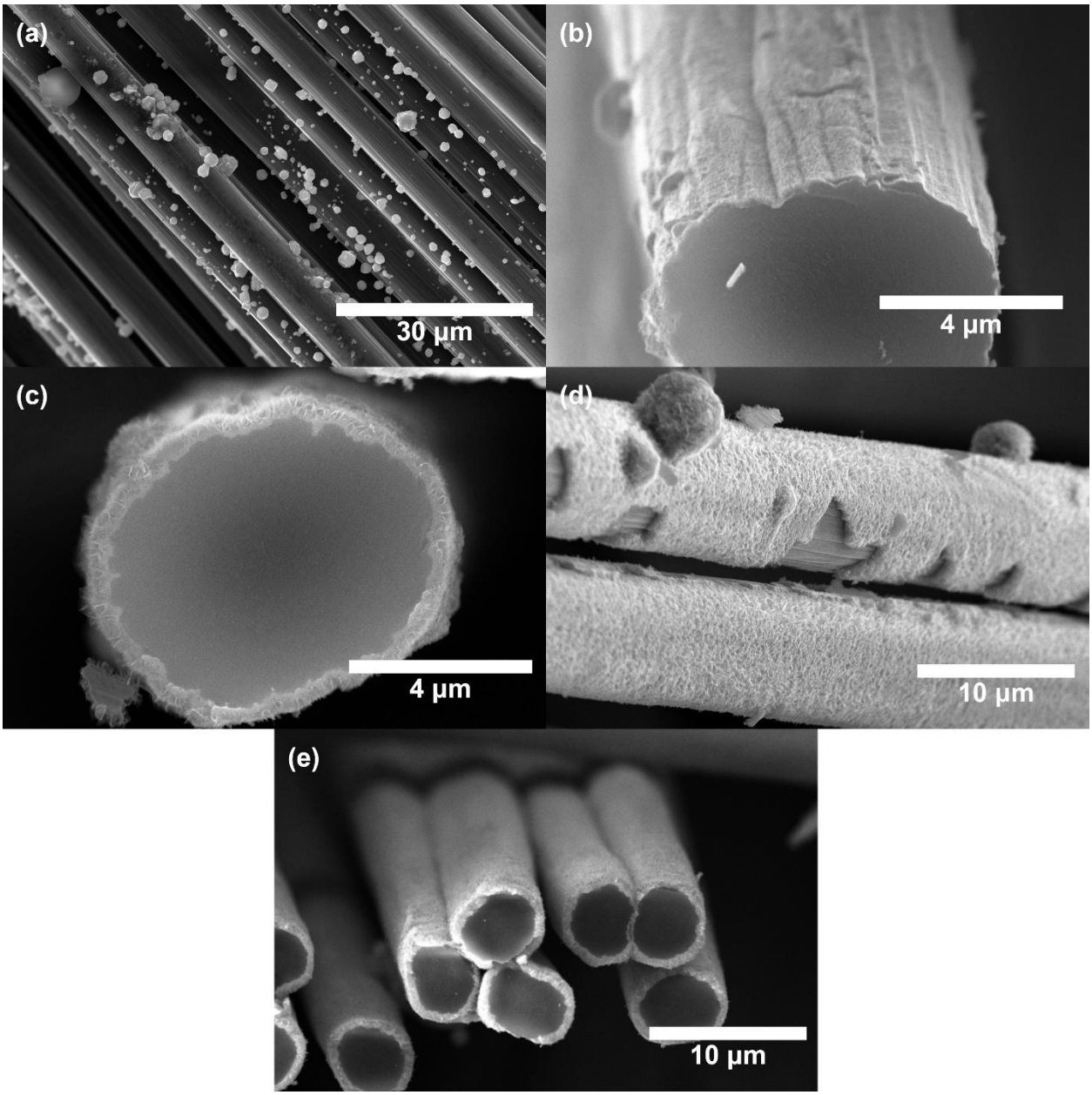

Figure 2.8 SEM micrographs of the TiC coating at different reaction times of (a) 0.5 (b) 1 (c) 2 (d) 3 (e) 4 hours showing the nucleation and growth of the coating over time.

With the optimized parameters, TiC was deposited at different reaction times (0.5, 1, 2, 3, and 4 hours) to track the nucleation and growth of the coating. At 0.5 hours (**Figure 2.8a**),

nodular particles of TiC soot ranging in size approximately 100-3500 nm were seen in SEM covering the fiber surfaces. A TiC thin film coating could not be resolved on the fibers, but EDS elemental mapping revealed sparse amounts of Ti spread evenly between the soot particles. From the 1 hour run (**Figure 2.8b**) the soot particles were still present, as well as a needle-like coating <100 nm thick in most areas. Some parts of the fiber surfaces were left uncoated. At 2 hours (**Figure 2.8c**), the needle-like coating grew to 200-400 nm in thickness and completely covered the fiber surfaces. This coating was also seen covering the soot particles. At 3 and 4 hours (**Figure 2.8d-e**) the coating grew to 350-700 nm and 350-900 nm, respectively. The needles were rounded off in most areas to a smoother coating.

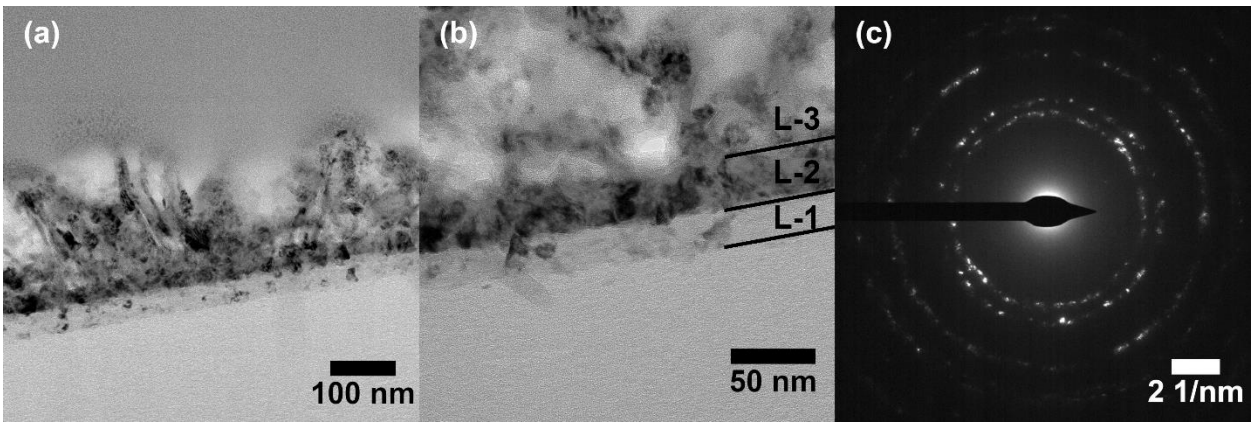

Figure 2.9 TEM analysis of the optimized TiC coating. (a, b) TEM images showing 3 distinct layers of the TiC coating denoted as L-1, L-2, and L-3. (c) SAED pattern from the coating in the L-2 layer.

TEM and SAED were used to further analyze the optimized TiC coating. A TEM sample of coated fiber was prepared using focused ion beam (FIB) milling. TEM images (**Figure 2.9a, b**) were taken revealing three distinct TiC layers in the coated fiber cross-section. In **Figure 2.9b**, these layers are labeled L-1, L-2, and L-3. The first layer of coating (L-1) is a portion of the carbon fiber surface which has been partially converted to TiC, about 25-40 nm thick. L-2 is a

relatively smooth layer of pure crystalline TiC, about 30-60 nm thick. Grains which grew off of the smooth layer of TiC had a needle-like morphology, creating a porous surface layer of TiC (L-3). These needle-shaped grains were up to 200 nm in length. TiC grains in L-2 were targeted for SAED (**Figure 2.9c**). The d-spacing values were calculated for the inner three rings of the diffraction pattern and compared to literature values for the Khamrabaevite TiC crystal structure. These three reflections correlated to d-spacings of 2.49 ± 0.01, 2.15 ± 0.01, and 1.52 ± 0.01 Å, respectively, which confirms that the coating is stoichiometric or near-stoichiometric crystalline TiC [33].

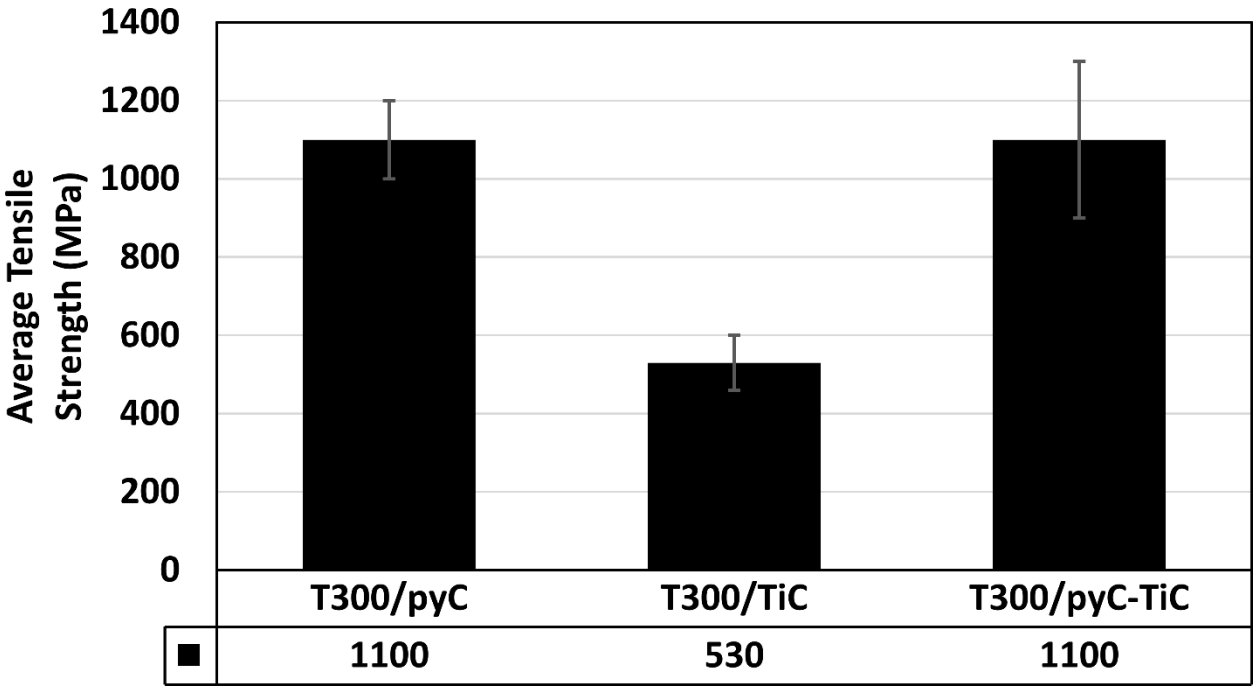

Figure 2.10 Chart of average ultimate tensile strengths for fibers coated with pyC and TiC.

Three sample sets were prepared for tensile testing, each with 10-12 specimens. The control sample set (T300/pyC) was specimens of carbon fiber tows coated with ~150 nm of pyrolytic carbon (pyC). PyC deposition was done according to the process outlined in **Section**

3.2.1. The second sample set (T300/TiC) was TiC-coated using the optimized CVI parameters. The last sample set (T300/pyC-TiC) had the ~150 nm of pyC with the optimized TiC coated on top. The average ultimate tensile strengths (**Figure 2.10**) were 1100 ± 100, 530 ± 70, and 1100 ± 160 MPa for samples C, TiC, and C-TiC, respectively.

2.4 Discussion

This study presents a method of depositing a relatively smooth coating of TiC onto carbon fibers by method of CVI using $TiCl_4$, CH_4, and H_2 gases. The smooth coating morphology, consistent coating thickness, and complete fiber coverage were achieved by optimizing CVI parameters. This included the deposition temperature, total gas flow rate, and gas flow rate ratio. Temperature optimization studies showed that lower temperatures produced a poorly adhered and incomplete coating. A coating such as this could not properly protect much of the carbon fiber during composite fabrication. The quality of subsequent coatings may also be negatively impacted. At 950 °C the coating surface was quite rough and some fibers were bridged together. If a matrix were to be applied, the fibers may be locked in place due to the high degree of roughness. This would prevent the ability for fiber pull-out and reduce the fracture toughness of the material. A comparatively smooth coating was produced at 1050 °C, but the high rate of deposition resulted in a thick shell of coating around the outside of the fiber tow, which sealed in the inner fibers. This created a high degree of coating thickness variability, which would make it impossible to properly apply further layers to the fibers, such as a matrix. The strength of the material would be reduced since the matrix would not be able to transfer load to the inner fibers. The optimum temperature was found to be 900 °C, but the resulting coating still showed some roughness.

This roughness was reduced during the total flow rate optimization by decreasing the flow of all gases. The first of the runs in this optimization had the highest flow rate (150 sccm). With the flow ratio of 2:1 H_2/CH_4, 100 sccm of H_2 was flowing through the bubbler. The flow rates of subsequent runs were chosen by reducing the H_2 flow by 25 sccm (100, 75, 50, 25 sccm) and calculating the CH_4 flow from the 2:1 flow ratio. The lowest flow rate gave the smoothest and most uniform coating. With less hydrogen passing through the bubbler there was less $TiCl_4$ entering the reactor and a slower rate of TiC deposition, which lead to a better coating quality. Lower flow rates were not investigated because they would have limited the flow ratio optimization that followed.

During the flow ratio optimization, higher ratios of H_2 to CH_4 gave overall better-quality coatings. The stoichiometry of TiC would suggest that a 1:1 ratio may be ideal, however the coating at this ratio had poor adhesion to the fiber, a high degree of roughness, and bridged fibers together in groups. Decreasing the ratio to 1:2 only worsened these effects. The highest ratio investigated was 4:1, which gave the smoothest and most uniform coating of all. This investigation in-part supported the idea that slower deposition rates produce a better-quality coating. A 4:1 ratio of gas flows results in fewer interactions between $TiCl_4$ and CH_4 compared to 1:1, so the deposition rate is likely to be slower. However, this phenomenon was not seen when the ratio was decreased rather than increased, which also would have reduced the number of interactions between $TiCl_4$ and CH_4. Ratios higher than 4:1 were not investigated because the CH_4 flow rate would have approached zero. The now fully optimized coating was well adhered to the fibers and free of cracks. Some SEM micrographs showed evidence of fiber and coating debonding. This condition of having a medium-strength bond benefits the fracture toughness of

the material due to the toughening mechanisms which are made possible by such a bond when excessive loads are applied, including fiber pull-out and crack deflection [34].

TiC coatings at different reaction times showed that the coating thickness could be easily controlled. However, at longer reaction times the thickness was less consistent and could vary as much as 500 nm within a single fiber tow. This was attributed to the distance between fibers in the fiber tow. The coating thickness on inner fibers is limited by the space between fibers, but the coating can grow indefinitely on the outer fibers. The range of coating times tested was 1-4 hours, which is similar to reactive-CVI (0.5 hours) [8] and MSS (1-5 hours) [29, 32] reaction times.

Varying the reaction time also revealed the mechanisms for nucleation and growth of the coating. A combination of soot particles and thin film coatings were seen on the fiber surfaces (**Figure 2.8**), suggesting two competing mechanisms of TiC formation. The nucleation and growth behavior during the CVI process as well as the precipitation of soots have been reported extensively [35]. Soots are known to form in the gas phase before they fall and stick to the substrate surface. A highly rough and poorly adhered film is created once the soot particles become bridged by the subsequent coating. This can happen when the gas precursor is too concentrated within the diluting gas or the process pressure is too high, which both promote molecular interaction in the gas phase. Since the process discussed here was performed at atmospheric pressure, sooting must be controlled by minimizing the gas precursor concentration. This was done by lowering the total gas flow rate and increasing the ratio of H_2 to CH_4, as more CH_4 lead to the formation of a poorly adhered sooty coating. Experiments for the 0.5 hour reaction time showed that soot particles will start to form before significant nucleation can be observed.

Previous studies on the nucleation and growth of CVI coatings suggest that smooth coatings result from having a high density of nucleation points which grow until the space between them is filled [35, 36]. A low nucleation density and high growth rate will create large hemispherical nodules and a rough film. High temperatures will cause this phenomenon, which explains the rougher coating at 950 °C compared to 900 °C. At 1050 °C the growth rate was so high that the coating covered the outer fibers before proper nucleation could develop on the inner fibers. At lower temperatures the nucleation and growth rates were too slow and sooting dominated the coating formation. The 1 hour reaction time showed that the optimized parameters satisfied the condition of having a high nucleation density, as many small needle-like growths were seen on the surface. Evidently, a lower precursor concentration and lower overall gas flow allowed for the formation of many nucleation sites before the growth could form large rough needles. The 2, 3, and 4 hour reaction times showed the nucleation sites growing and rounding off into a relatively smooth film.

Cross sectional images taken from TEM revealed more about the coating. Layer L-1 of the coating (**Figure 2.9**) contained some TiC which seems to have formed from the $TiCl_4$ reacting with the surface of the carbon fiber. Surface damage such as this is likely to reduce the strength of the fiber, which was confirmed from the tensile testing results. The TiC coated fibers were less than half as strong as the same fibers coated with pyC instead. This suggests that carbon fibers should be coated with a protective layer before TiC is applied. This was tested by coating the fibers first with pyC then with TiC and measuring the tensile strength. The average strength of these fibers was approximately the same as that of the fibers coated with just pyC, revealing that the pyC effectively prevented $TiCl_4$ from compromising the strength of the fibers. Similar results were encountered by Wang et al. [29] The thickness of the protective pyC layer

was greater than the thickness of L-1 seen in TEM to avoid the penetration of $TiCl_4$ into the surface of the fiber. An added benefit to the pyC layer is that it can act as a medium-strength interphase between the fiber and matrix for fracture toughness. Still, this increase in toughness comes at the cost of reduced overall tensile strength compared to the as-received fiber due to the presence of residual stresses at the fiber/coating interface. [29] Since the TiC CVI reaction does not depend on using carbon from the surface of the fiber, the protective coating may be composed of materials other than pyC if so desired.

Also seen in the TEM images was a layer of relatively smooth TiC (L-2) and a rougher layer on the very surface (L-3). This may be evidence to suggest that there is an epitaxial effect on the morphology of CVI TiC, in which depositing onto carbon yields smooth TiC and depositing onto TiC yields needle-like TiC. Other substrates may produce different morphologies.

2.5 Conclusions

The atmospheric pressure CVI of TiC onto carbon fiber using $TiCl_4$, CH_4, and H_2 gases was optimized to produce a uniform thin film coating with complete fiber coverage and a smooth morphology. Because this was done at atmospheric pressure, expensive and complicated pressure control instrumentation was not required. The TiC coating was similar in quality to TiC coatings from MSS [29, 32] and reactive-CVI [8] methods of producing TiC on carbon fibers. In Both MSS and reactive-CVI the carbon in the TiC comes from the carbon fibers, which can reduce the integrity of the fibers. The TiC CVI reported here uses CH_4 as the carbon source instead.

The presence of crystalline TiC was confirmed by both powder X-ray diffraction and electron diffraction. The optimized CVI temperature was found to be 900 °C. Lower

temperatures produced poorly adhered coatings with incomplete fiber coverage, likely because gas phase soot formation occurred more rapidly than growth at the substrate surface. Higher temperatures resulted in rougher morphologies and fiber bridging due to a high growth rate and fewer nucleation sites. TiC CVI has been criticized for using destructively high temperatures, but this temperature optimization showed that this process can be done at the lower end of the temperature ranges used in the MSS (900-950 °C) [29, 32] and reactive-CVI (927-1027 °C) [8] methods. The total flow rate of the reaction gases (H_2 & CH_4) was shown to have an effect on the coating roughness. Higher flow rates produced a needle-like morphology, while lower flow rates gave a smoother coating. The minimum flow rate tested was 37.5 sccm, which gave the smoothest morphology. The last parameter investigated was the flow ratio of H_2 to CH_4, which was shown to affect the adhesion of the coating to the fibers as well as the occurrence of fiber bridging. Having a higher ratio of H_2 gave drastically better coatings. The optimum ratio chosen was 4:1 sccm H_2/CH_4. This combination of low flow rate and high H_2 concentration minimized soot formation and allowed for the steady growth of a high density of nucleation sites, resulting in a relatively smooth TiC film. With the optimized parameters, it took around 2 hours to produce a coating with complete coverage, which is comparable to MSS (1-5 hours) [29, 32] but longer than reactive-CVI (0.5 hours) [8]. TEM cross sectional images showed that there is a compact layer of TiC beneath the more porous layer on the outer surface. The TEM images and fiber strength testing showed that the TiC coating penetrated into the carbon fiber surface causing loss of strength. This was overcome by first coating the fibers with a sacrificial layer of pyC. These protected fibers showed no significant strength loss after being coated with TiC.

Chapter 3

Comparison of Various Ceramic Coatings for the Protection of Carbon Fibers in Silicon Melt Infiltrated Composites

3.1 Introduction

Carbon fiber reinforced silicon carbide composite materials (C/SiC) show considerable promise across multiple industries including aerospace and nuclear energy. These composites are renowned high temperature structural materials due to their high strength-to-weight ratio, fracture toughness, oxidation resistance, and abrasive properties [4, 6, 7, 12, 15, 22, 37]. Such composites are target materials for tribological applications [4-6, 37] such as aircraft and high-end car brakes and electromagnetic shielding applications [7, 15] such as nuclear fuel rods. Tribologically, C/SiC outperforms carbon/carbon (C/C) due to the stability in friction coefficient and superior oxidation resistance. The SiC matrix forms a SiO_2 passivation layer at the onset of oxidation, thereby protecting the bulk composite and minimizing further oxidation [4-6, 10, 12].

Various methods of producing a SiC matrix on carbon fibers have been developed and often used alongside one another, including chemical vapor infiltration (CVI), silicon melt infiltration (SMI), polymer infiltration & pyrolysis (PIP), and slurry infiltration. In the PIP method, a pre-ceramic polymer is infiltrated into a fiber preform and pyrolyzed into SiC at high temperatures [4, 6, 15]. The viscosity of the polymer can be controlled to optimize for large or complex parts, allowing for better infiltration. However, porosity is introduced during pyrolysis as the solvent and byproduct gases exit the composite. Multiple PIP cycles can be performed to minimize porosity, but this method cannot achieve a fully dense composite alone. In CVI,

precursor gases or vapors flow over the fiber substrate under controlled conditions where they react at the substrate surface and grow the SiC coating outward radially [6, 35, 38]. The method produces highly uniform coatings at fairly low temperatures (900-1100 °C). However, CVI has a number of complications including residual porosity, unstable precursors, corrosive byproducts, expensive equipment, and long processing times. Due to the complicated pore structure of fiber preforms, it is common for CVI coatings to "can-off" the smaller pores between individual fibers while the larger pores between fiber tows are being infiltrated, leaving behind closed off pore channels that cannot be further infiltrated. This can be minimized to an extent by controlling process parameters such as temperature, pressure, and precursor gas flow rates, but it remains a difficult challenge for SiC matrix synthesis. The SMI process overcomes many of the challenges faced by PIP and CVI. First, a porous carbon matrix is applied to a fiber preform using PIP or other methods. Then molten silicon is infiltrated into the fibers to react with the carbon and form silicon carbide [2, 4, 6, 22, 28]. Residual porosity is minimal due to the wicking effect of the molten silicon and the volumetric expansion of the matrix from the reaction between silicon and carbon. SMI is a relatively simple and rapid process that does not involve hazardous precursors or byproducts. The primary drawbacks of SMI are high processing temperatures potentially weakening the carbon fibers, incomplete reaction of precursors leaving residual elemental silicon and/or carbon, and reaction between the molten silicon and the carbon fibers.

The current work seeks to address one of the SMI drawbacks—the molten silicon induced degradation of the carbon fibers. As the silicon melt wicks through the porous carbon network it is possible for some of the excess to diffuse to the fiber surface where the silicon will indiscriminately react with the carbon fiber instead of the carbon matrix [2, 6, 28]. As the primary load-bearing constituent of the C/SiC composite, the carbon fibers must remain

undamaged in order to maintain the tensile strength of the material. Workarounds for the issue have been developed in the past. The PIP method can be used on carbon fiber tows to create densely infiltrated C/C tow composites. A preform can be made from the C/C rods to then undergo the typical SMI procedure of infiltrating a porous carbon matrix and reacting with molten silicon to form a C/C-SiC composite. The dense carbon coating supposedly prevents the silicon melt from reaching the fibers [2]. Unfortunately, this strategy limits the complexity of the composite geometry to what can be made from the straight C/C rods.

In a somewhat similar strategy, a dense pyC interphase coating can be applied to a fiber preform (any geometry may be used) via CVI before performing the SMI process [2, 4, 22]. This workaround and the last both produce a C/C-SiC composite rather than a true C/SiC, which may be undesirable depending on the application. Additionally, a thick enough pyC layer could contain porosity from the PIP or CVI processes and may not necessarily protect the fibers adequately if enough silicon melt is present to react through the layer and reach the fiber. For these reasons, it would be most helpful to have a thin interphase coating around the fibers to act as an inert and impenetrable barrier to the silicon melt. This has been done by applying a thin film of SiC via CVI [6]. Prior to the SiC coating, it is necessary to first apply a thin pyC interphase directly on the fibers to prevent the SiC CVI precursor from reacting with the fiber surface and reducing the strength. This is not necessarily a drawback because the pyC interphase layer also provides fracture toughness to the material by allowing for mechanisms such as fiber pull-out and crack deflection [2, 6, 13].

It may be feasible and practical to protect the carbon fibers from degradation using interphase coatings other than SiC. There are various other high temperature ceramic materials that have been considered for use as interphase coatings in ceramic matrix composites, including

BN [9, 39, 40] and TiC [8, 28, 29, 41]. TiC is thermally stable above 3000 °C and resistant to oxidation and wear. TiC Interphase coatings have previously been produced using a relatively simple atmospheric pressure CVI method at relatively low temperatures [41]. It can also be produced on carbon fibers using a molten salt method [28, 29]. On contact with silicon melt, it may be the case that the TiC layer will convert to Ti_3SiC_2, one of the MAX phases. Multiple MAX materials have been considered for use in CMCs due to their unusual, but beneficial combination of properties including high thermal conductivity, thermal stability, and thermal shock resistance [29, 42]. In particular, Ti_3SiC_2 is highly inert and resistant to oxidation at high temperatures. If this material were to form at the fiber/matrix interface in a composite, it could very well aid in protecting the carbon fibers during use. Hexagonal BN is very commonly reported as a superb interphase layer for high temperature composites, especially in SiC/SiC. In addition to being oxidation resistant, the graphitic-like structure of h-BN provides the ideal medium-strength bond between fiber and matrix to introduce fracture toughness to the composite. BN is typically produced using a low-pressure CVI method. Similar to SiC coatings on carbon fibers, pyC must be applied prior to the TiC or BN layers so that the CVI precursors and byproducts do not degrade the fibers.

In this study, four different protective coating systems for C/SiC composites produced by SMI are compared: pyC, pyC-SiC, pyC-TiC, and pyC-BN. These coating systems were applied to carbon fiber tows, which were tensile tested and analyzed under scanning electron microscopy (SEM) to assess the ability to protect the fibers from silicon melt and to observe the resulting coatings.

3.2 Experimental

3.2.1 CVI of PyC, SiC, and BN Interphase Coatings

All coatings in this study were applied to T300 ex-PAN 3 K continuous carbon fiber tow supplied by TORAYCA®. Coatings of pyC, BN, and SiC were performed in the low pressure CVI tube furnace reactor seen in Figure 3.1. The tube furnace comprises three independently controlled temperature zones to maintain a consistent temperature throughout a 1.2 m long hot zone where the depositions took place. The reaction chamber was a 1.8 m long quartz tube with a 20 cm inner diameter, which was sealed off to the atmosphere. A graphite liner in the tube was used to protect the quartz from the deposited coatings and their respective byproducts, such as corrosive HCl gas. Samples were held on graphite tooling loaded in the center of the reactor tube. Precursor gases were flowed in and controlled using mass flow controllers. Pressure was measured and controlled using capacitance manometers in combination with an automatic control valve. Exhaust gases were sent through a liquid nitrogen cooled trap to collect condensed phase byproducts before exiting the gaseous byproducts through an oil-lubricated rotary vane pump. Two stages of filters with increasing pore size preceded the pump to protect the mechanical parts from any solid material that may have made its way through. CVI parameters for all three reactions are summarized in **Table 3.1**.

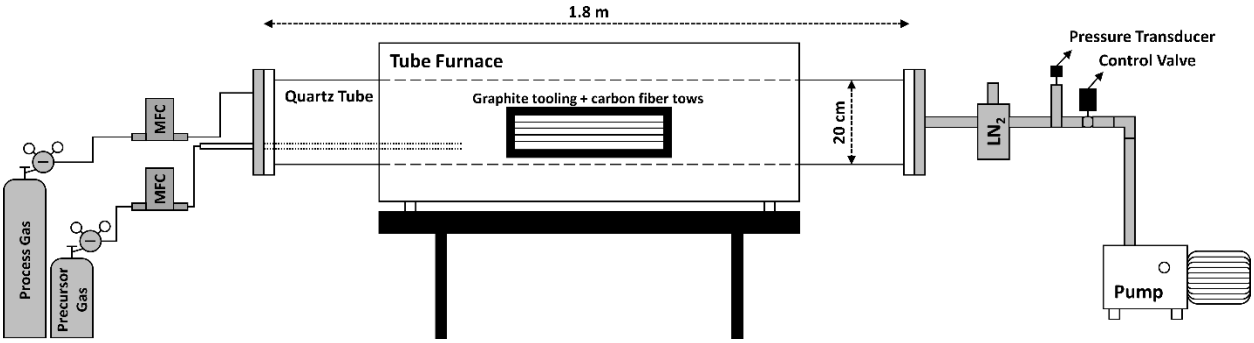

Figure 3.1 Diagram of CVI reactor used for pyC, SiC, and BN coatings.

For pyC coatings, propylene precursor gas (chemically pure, 99.0%) and nitrogen process gas (ultra-high purity, 99.999%) purchased from Airgas were used. Carbon was deposited according to the thermal decomposition of propylene in the presence of N_2 gas at 1050 °C and <1 torr (**Equation 3.1**). Flow rates of propylene and nitrogen gases during the reaction were 200 and 100 standard cubic centimeters per minute (sccm), respectively. The CVI reaction went for a duration of 120 minutes. All samples with a pyC coating came from the same pyC CVI run for consistency.

Equation 3.1 $C_3H_{6\,(g)} \rightarrow 3C_{(s)} + 3H_{2\,(g)}$ T = 1050 °C, P < 1 torr, N_2

For SiC coatings, nitrogen process gas was used, as well as methyltrichlorosilane (MTS, 98% purity) purchased from Gelest and hydrogen (ultra-high purity, 99.999%) purchased from Airgas. The liquid MTS precursor was held in a glass vessel and vaporized using the process vacuum and heating tape before flowing through the mass flow controller and into the quartz tube. SiC was produced according to the thermal decomposition reaction of MTS in the presence of H_2 and N_2 gases at 1050 °C and 50 torr (**Equation 3.2**). Flow rates of MTS, H_2, and N_2 were

80, 800, and 600 sccm, respectively. The reaction went for a duration of 75 minutes. The SiC-coated fibers were all prepared simultaneously in a single CVI run.

Equation 3.2 $CH_3SiCl_{3\,(g)} \rightarrow SiC_{\,(s)} + 3HCl_{\,(g)}$ T = 1050 °C, P = 50 torr, H_2, N_2

For BN coatings, nitrogen process gas was used, as well as boron trichloride (BCl_3, chemically pure, 99.9%) purchased from Matheson Gas and ammonia (anhydrous, 99.99% purity) purchased from Airgas. The BCl_3 and NH_3 gases were kept separate before entering the quartz tube. BN was deposited according to the reaction between BCl_3 and NH_3 gases in the presence of N_2 gas at 800 °C and ~1 torr (**Equation 3.3**). Flow rates of BCl_3, NH_3, and N_2 gases were 125, 500, and 400 sccm, respectively. The CVI reaction went for a duration of 45 minutes. The BN-coated fibers were all prepared simultaneously in a single CVI run.

Equation 3.3 $BCl_{3\,(g)} + 4NH_{3\,(g)} \rightarrow BN_{\,(s)} + 3NH_4Cl_{\,(g)}$ T = 800 °C, P ≈ 1 torr, N_2

Coating	T (°C)	P (torr)	Time (min)	Precursor 1 (sccm)	Precursor 2 (sccm)	Nitrogen (sccm)	Hydrogen (sccm)
PyC	1050	<1	120	200 (C_3H_6)	0	100	0
SiC	1050	50	75	80 (MTS)	0	600	800
BN	800	~1	45	125 (BCl_3)	500 (NH_3)	400	0

Table 3.1 CVI parameters for pyC, SiC, and BN coatings.

3.2.2 CVI of TiC Interphase Coatings

CVI of TiC was done in an atmospheric pressure CVI tube furnace reactor (**Figure 2.1**) according to the process outlined in **Section 2.2.2**. Titanium (IV) chloride ($TiCl_4$, 99.0%) was purchased from Alfa Aesar. Hydrogen (ultra-high purity, 99.999%) and methane (ultra-high purity, 99.99%) gases were purchases from Airgas. Carbon fibers were loaded inside of a 60 cm long quartz tube with a 2.5 cm diameter lined with graphite foil. Gas flow rates were controlled using mass flow controllers. The liquid $TiCl_4$ precursor was held inside of an air-free glass bubbler in which the hydrogen was bubbled through to carry $TiCl_4$ vapor into the quartz tube. The glass bubbler was heated to 50 °C using heating tape to encourage vaporization. TiC was produced by the reaction between $TiCl_4$ and CH_4 in the presence of H_2 gas at 900 °C (**Equation 3.4**). CH_4 was set to flow at 7.5 sccm and H_2 bubbled through the $TiCl_4$ bubbler at a rate of 30 sccm. The CVI parameters are summarized in Table 3.2. Exhaust gases were bubbled first through a hydrocarbon oil bath, which acted as an atmospheric barrier, followed by a 1 M NaOH (aq.) solution to neutralize the HCl byproduct. The CVI reactions went for durations of 120 minutes. The TiC-coated fibers were prepared across two CVI runs due to the limitation in reactor size.

Equation 3.4 $TiCl_{4\,(g)} + CH_{4\,(g)} \rightarrow TiC_{\,(s)} + 4HCl_{\,(g)}$ T = 900 °C, P ≈ 760 torr, H_2

Temperature (°C)	Pressure (torr)	Time (min)	H_2 (sccm)	CH_4 (sccm)
900	~760	120	60	7.5

Table 3.2 CVI parameters for TiC coatings.

3.2.3 Silicon Deposition

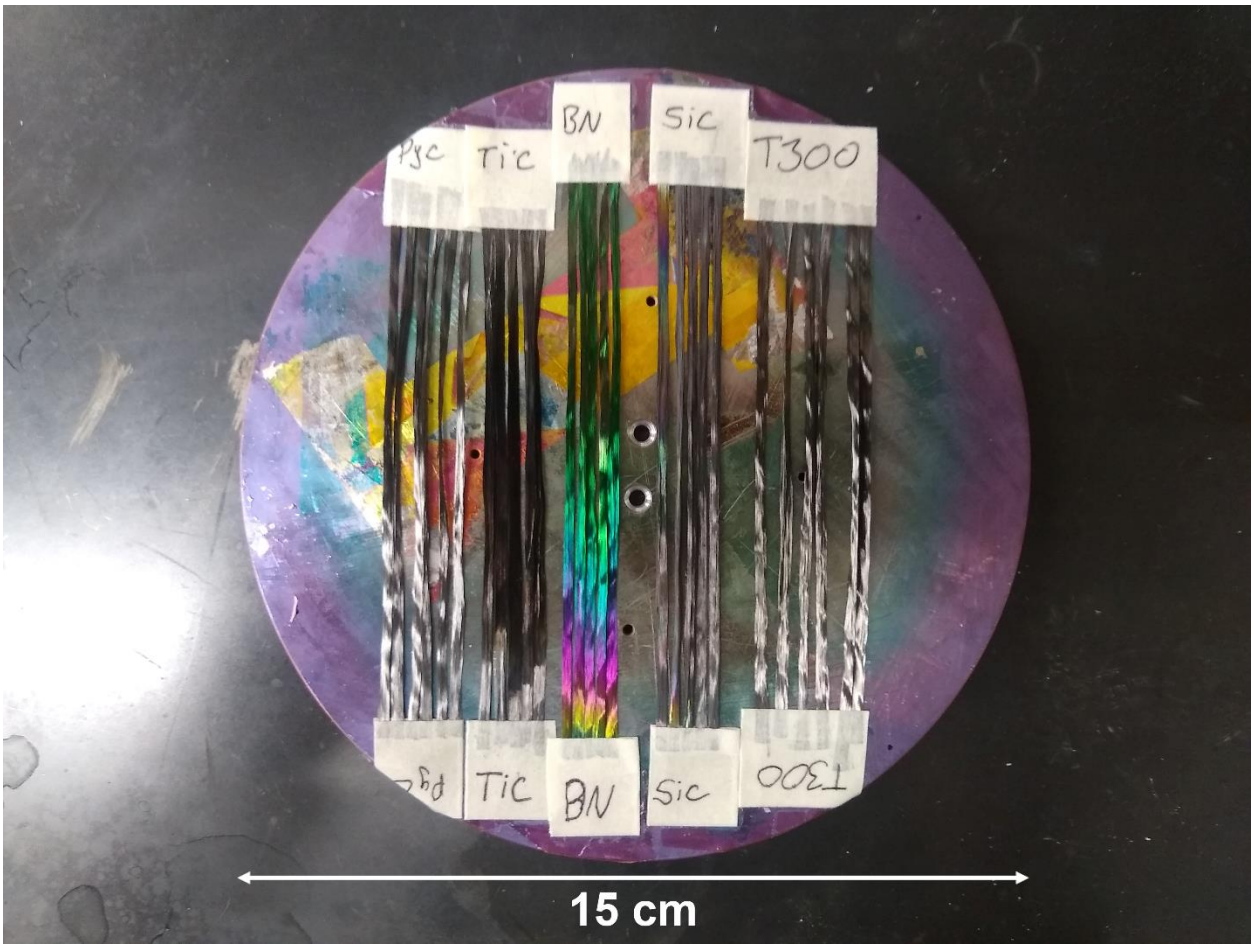

Figure 3.2 CVI-coated fiber tow specimens mounted to the rotating stage prior to silicon deposition.

A Denton Vacuum BenchTop Turbo Thin Film Deposition evaporator was used to coat fiber tow samples with silicon metal. The ends of the fiber tows were affixed to a rotating stage inside the deposition chamber with tape (**Figure 3.2**). Silicon metal was thermally evaporated from a tungsten crucible and deposited onto the fibers in batches until a 300-350 nm thick coating was produced. Charges of 20 mg of silicon metal were added to the crucible in between depositions. The fiber tows were flipped to coat both sides evenly. The power setting on the instrument was maintained at 28% during deposition.

3.2.4 Heat Treatments

To simulate the SMI process, fiber tow samples coated in silicon were heated under argon beyond the melting point of silicon. This was also done to a control group of fiber tows which were not coated with silicon. The heat treatments were done in a 1.2 m long alumina tube with a 4 cm inner diameter. The fiber tows were loaded inside a smaller quartz tube, which was plugged on both ends with a porous carbon foam material and placed in the center of the alumina tube. The foam plugs served to filter out alumina particles ejected from the outer tube during heating and prevent them from contaminating the fiber tow samples while still allowing for argon flow through the quartz tube. Prior to the heat treatments, the air was pumped out of the alumina tube to prevent oxidation of the fibers and coatings. The vacuum was held for ~12 hours to ensure complete evacuation of oxygen and moisture. The tube was then backfilled with argon to bring it back up to atmospheric pressure before the heat treatment. Argon was allowed to flow for ~1 hour before heating began. The exhaust argon gas was flowed into a hydrocarbon oil bath, which acted as an atmospheric barrier. The furnace ramped to 1550 °C at a rate of 8 °C/min where it held for 1 hour before ramping down to room temperature at 8 °C/min. The temperature and time parameters were based on an SMI process performed by Xu et al. [6].

3.2.5 Tensile Testing

Tensile testing was performed with an Instron® 5869 universal testing system equipped with a ± 5 kN load cell. The fiber tows were mounted to cardstock on both ends using epoxy to aid with gripping (**Figure 2.3**). A 2.5 cm gage window was used. The tests ran until failure at a rate of 0.05 mm/s. At least four specimens were successfully tested for each sample set and no more than six.

3.2.6 Characterization

Scanning electron microscopy (SEM) was used to obtain micrographs of the fibers at various stages of the study and analyze the coatings. The instrument used was a ThermoFisher TeneoLoVac Field Emission SEM operated at 10-20 kV and 0.4-1.6 nA.

Grazing incidence X-ray diffraction (GIXRD) was used to detect crystalline phases within coated fiber samples. Fiber tow samples were taped to glass slides for the analysis. The instrument used was a SmartLab X-ray Diffraction System using a grazing angle of 0.5°. Angles of 2θ ranged from 10 to 80°.

3.3 Results

3.3.1 CVI Coatings

Carbon fiber tows were coated to prepare the following CVI protective coating systems: T300/pyC-SiC, T300/pyC-TiC, T300/pyC-BN. Additional systems were prepared as control groups for comparative purposes: T300 (as received, with no coatings) and T300/pyC. Samples for SEM analysis were taken after each CVI coating for analysis.

The pyC coating (**Figure 3.5a**) exhibited a smooth morphology. Fiber coverage was complete with minimal area of exposed fiber, most of which was seen at the locations of cross sections where the fibers were mechanically agitated. Adhesion to the fiber appeared to be good, as very little coating separated even where the fibers were agitated. Coating thickness ranged from 200-300 nm.

The SiC coating (**Figure 3.6a**) had a nodular morphology. Much of the coating comprised very small nodules, which made up a relatively smooth continuous coating. Most of the fibers were also covered in larger disjointed nodules ranging 0.3-2 μm in size. The "smooth"

coating was complete in fiber coverage. This coating was seen separating from the pyC coating below in some fiber cross sections. Coating thickness ranged from 160-250 nm.

The TiC coating (**Figure 3.7a**) was also nodular in morphology and relatively rough compared to all other coatings. Similar to the SiC coating, larger nodules could be seen growing from the smoother coating below ranging in size 0.3-2 μm. Coating seemed to separate completely from the fiber in areas of mechanical agitation, but the rest of the fibers were covered completely. Coating thickness ranged from 150-300 nm.

The BN coating (**Figure 3.8a**) was smooth in morphology. Nodules were not observed, but thin layers of the surface could be seen peeling off. Fibers were completely covered and separation of the BN coating was rare. Coating thickness ranged from 300-400 nm.

3.3.2 Silicon Coatings

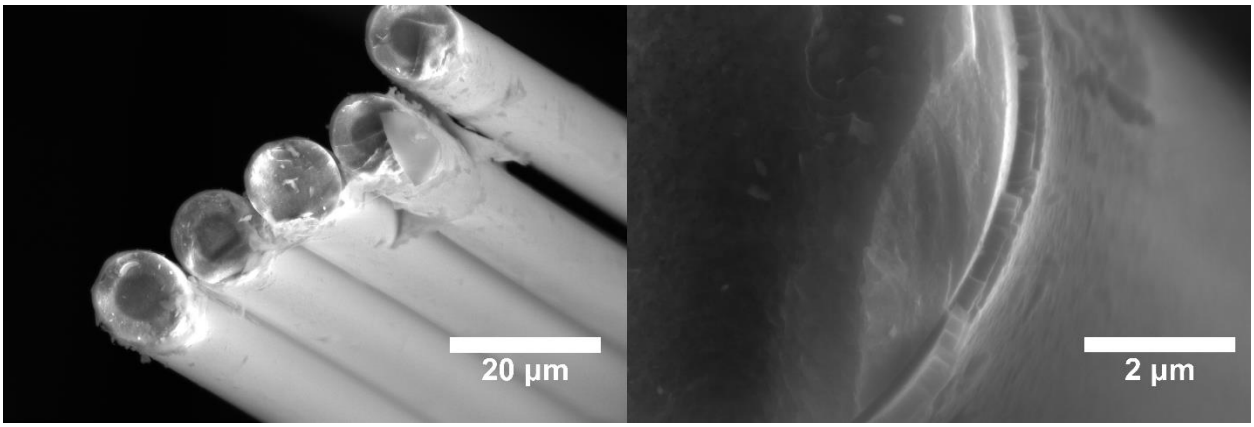

Figure 3.3 Silicon coatings on silicon carbide fibers.

Silicon metal was deposited onto fiber tow specimens from all protective coating systems and control systems (i.e. T300, T300/pyC, T300/pyC-SiC, T300/pyC-TiC, and T300/pyC-BN) using thermal evaporation. All fiber tows were coated simultaneously across a total of 20 depositions, 10 per side, each run with 20 mg of silicon loaded in the crucible. The instrument

ran at 28% power during each deposition. These parameters were determined by first coating as-received silicon carbide fibers using this method (**Figure 3.3**). The SiC fibers used were more regular in cross section compared to the carbon fibers used in this study, which simplified the silicon coating thickness measurements. With the conditions used, 10 deposition cycles produced 300-350 nm of silicon on a single side of the SiC fiber tows.

3.3.3 Heat Treatments

After heating the silicon coated fiber tows as well as an identical set of fiber tows which did not receive a silicon coating, SEM samples were taken for analysis. Average coating thickness measurements are listed in **Table 3.3**.

Sample		**PyC**	**PyC-SiC**	**PyC-TiC**	**PyC-BN**
Outer Coating Thickness (nm)	**Without Si**	200 ± 25	180 ± 20	200 ± 60	390 ± 70
	With Si	230 ± 45	700 ± 200	200 ± 60	270 ± 20

Table 3.3 Average coating thicknesses of the outer coatings in each fiber system after heat treatment with and without silicon coatings.

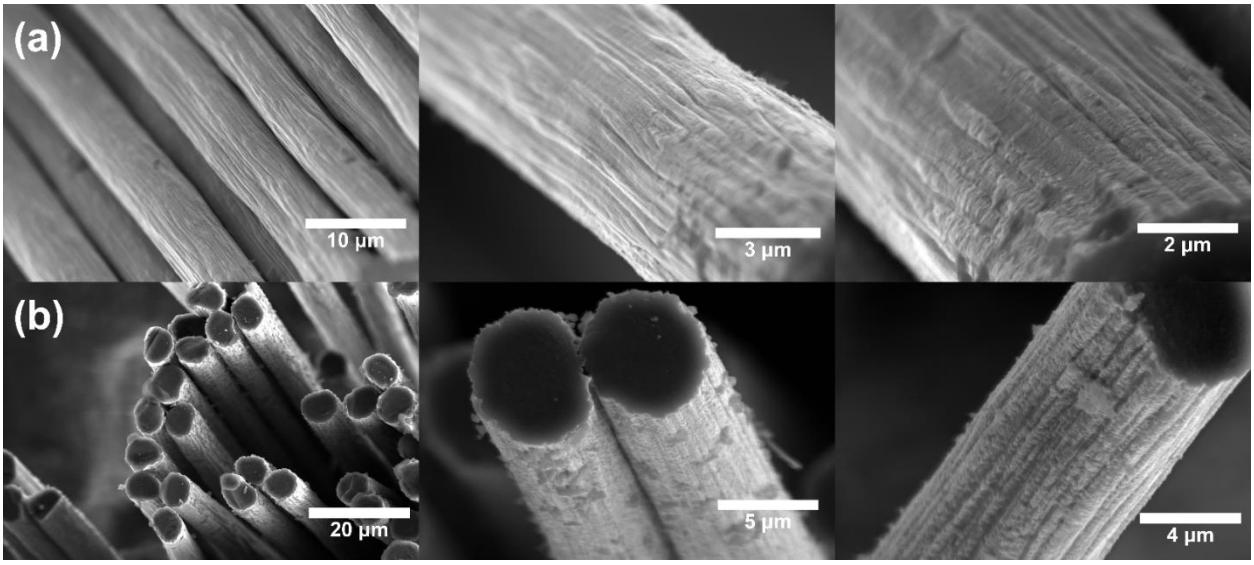

Figure 3.4 Micrographs of the as-received T300 carbon fiber after heat treatment (a) without silicon and (b) with silicon.

The heat treated as-received T300 fibers without silicon coating were unremarkable in appearance. Cross sectional imperfections are normal in this type of carbon fiber, but no surface features developed as a result of the heat treatment. The fiber diameters averaged ~6.9 µm. In contrast, the T300 fibers that received a silicon coating prior to heat treatment were significantly impacted. The surfaces were rough with nodules. The cross sections appeared more jagged and degraded. The average fiber diameter decreased to ~6.5 µm. The SEM micrographs of these fibers can be seen in **Figure 3.4b-c**.

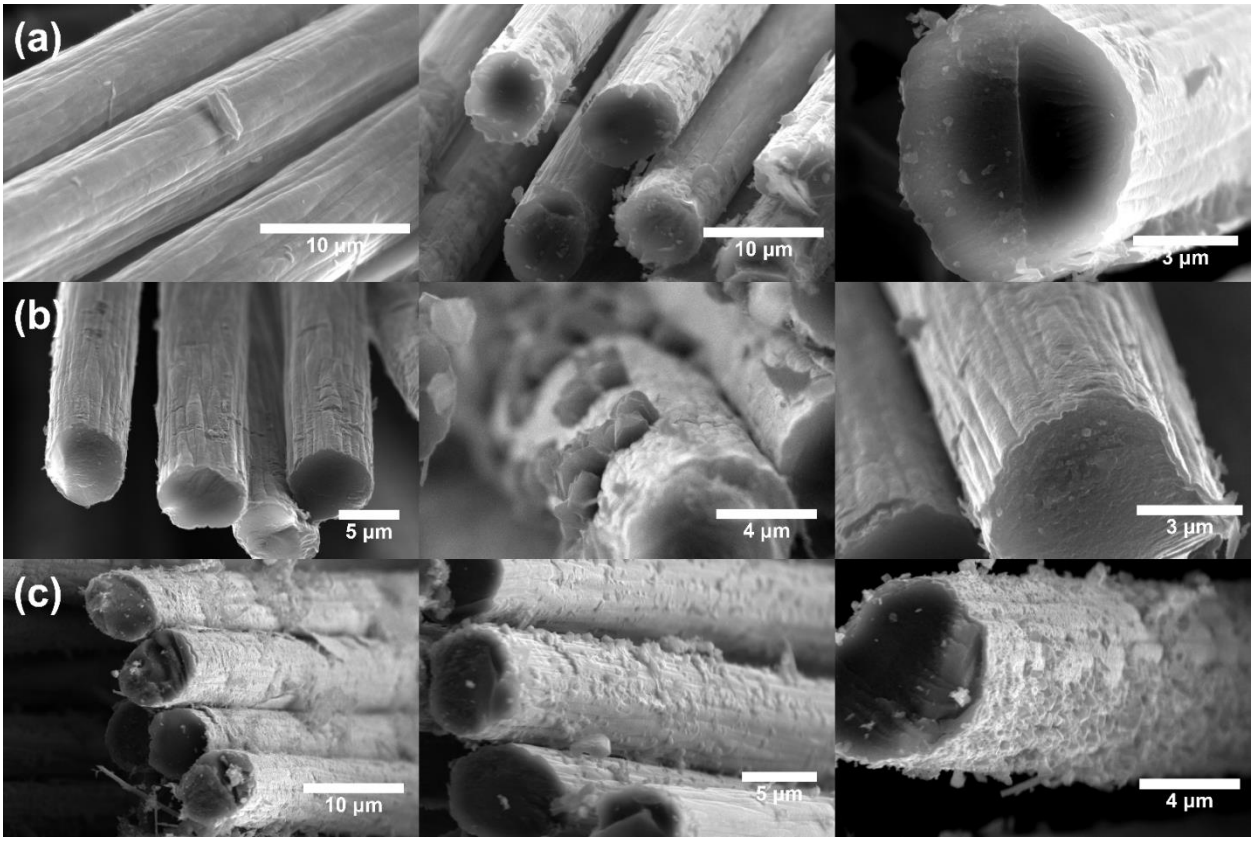

Figure 3.5 Micrographs of the T300/pyC samples (a) before heat treatment (b) after heat treatment without silicon and (c) after heat treatment with silicon.

The T300/pyC samples without silicon appeared slightly grainier in texture compared to before the heat treatment, though were still relatively smooth overall. However, large crystals 1-2 µm in size were observed in some areas, though rare. Much like the T300 samples, the T300/pyC samples coated in silicon became rough with nodules on the surface after the heat treatment. It is unclear if the fiber beneath the coating was affected. Coating adhesion appeared to be unaffected with and without silicon. The SEM micrographs of these fibers can be seen in **Figure 3.5b-c**.

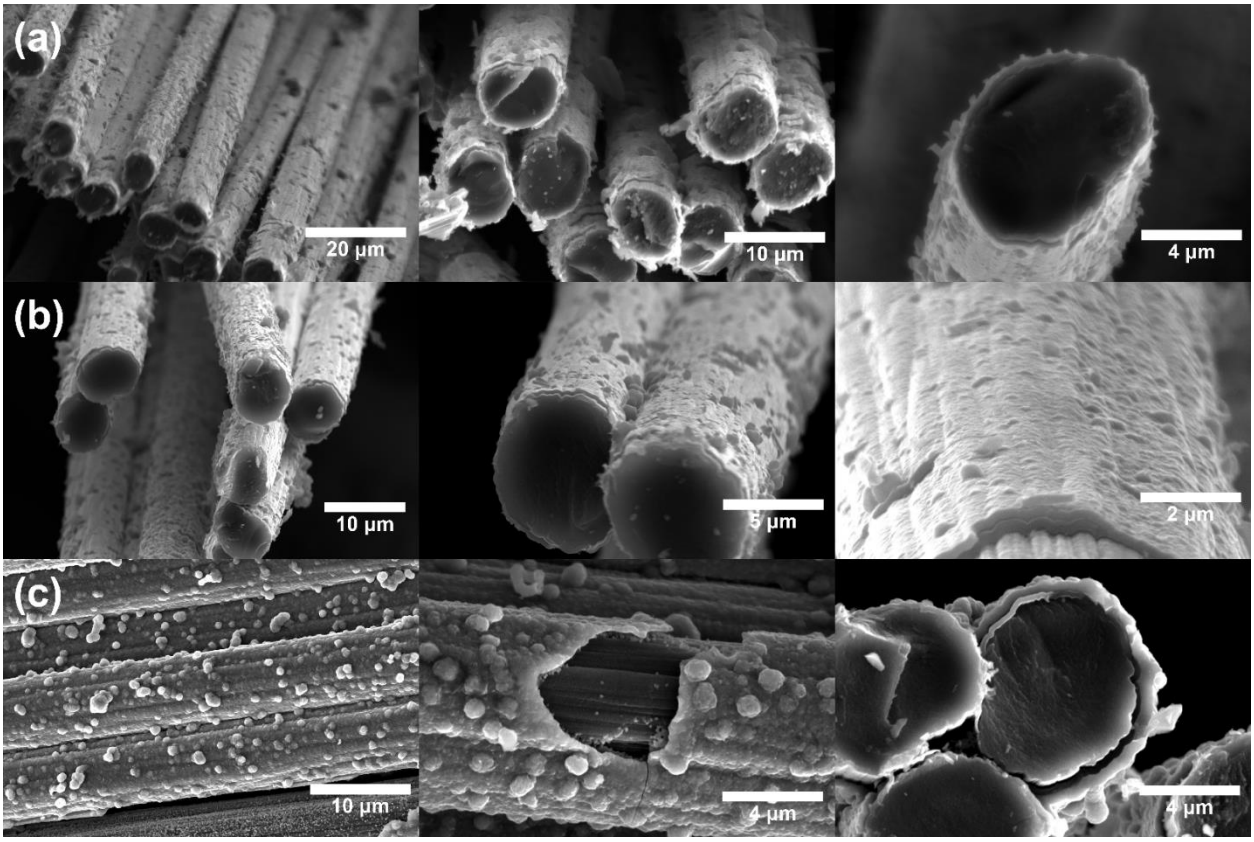

Figure 3.6 Micrographs of the T300/pyC/SiC samples (a) before heat treatment (b) after heat treatment without silicon and (c) after heat treatment with silicon.

No changes to the T300/pyC-SiC samples were observed post heat treatment. However, the samples coated with silicon had much different surface features. The outer coating was much thicker, growing from ~180 nm to ~650 nm. The surface nodules were larger in size and appeared more fused to the surface. In some areas, the surface had a rough porous coating over the SiC layer. The coating was observed separating from the pyC layer, but to no higher degree than was observed before the heat treatment. The SEM micrographs of these fibers can be seen in **Figure 3.6b-c**.

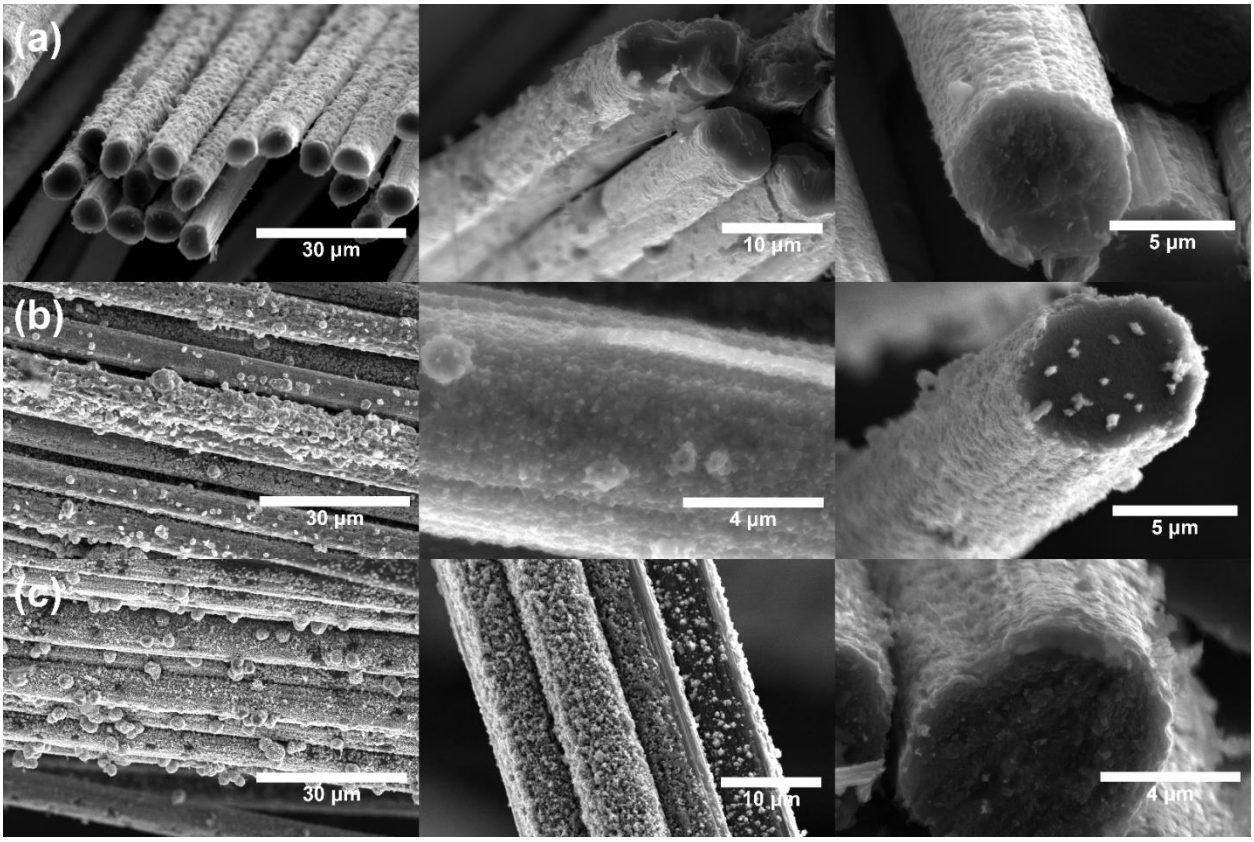

Figure 3.7 Micrographs of the T300/pyC/TiC samples (a) before heat treatment (b) after heat treatment without silicon and (c) after heat treatment with silicon.

The T300/pyC-TiC samples were affected significantly by the heat treatment. The surface became much rougher and nodules were larger. In some areas the coating became discontinuous, exposing the pyC coating below. Similar results were observed in the T300/pyC-TiC samples which received a silicon coating. The silicon did not seem to affect the final morphology. The SEM micrographs of these fibers can be seen in **Figure 3.7b-c**.

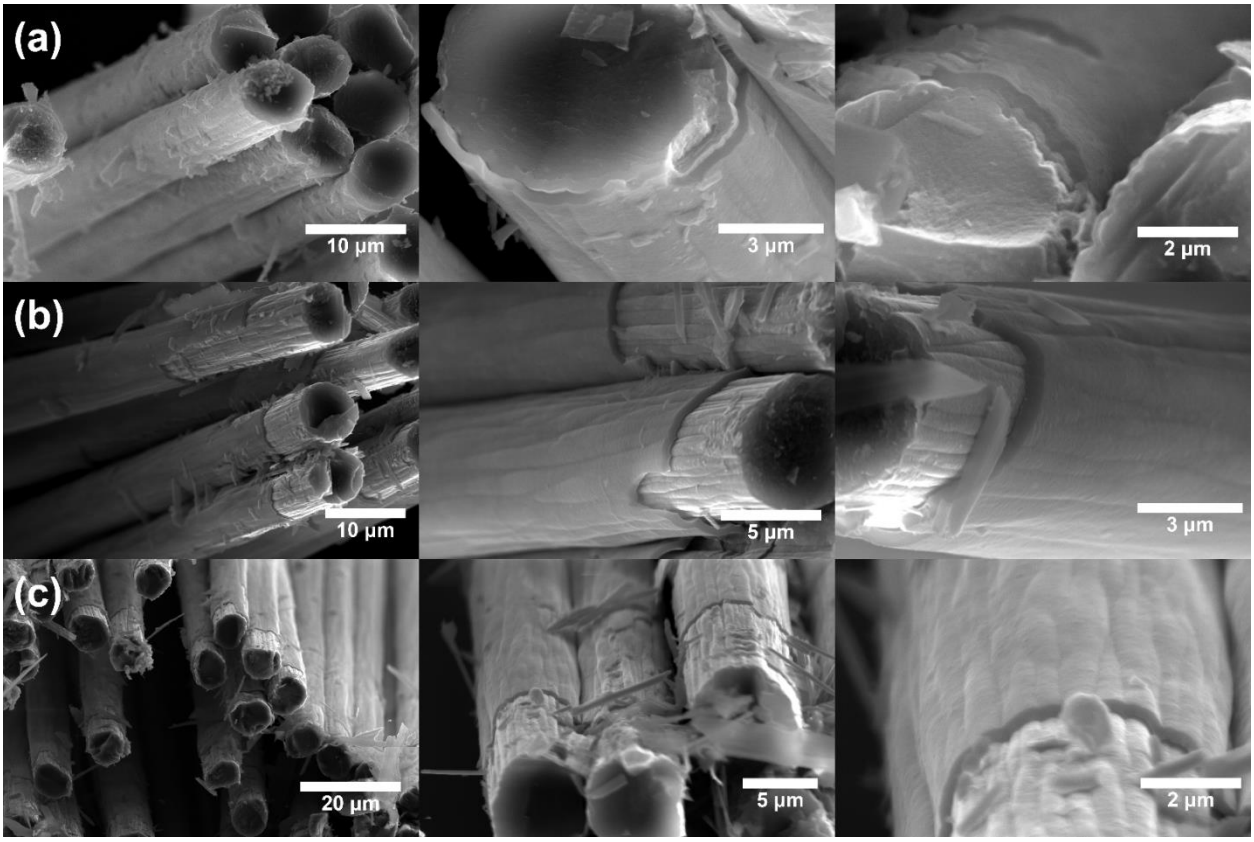

Figure 3.8 Micrographs of the T300/pyC/BN samples (a) before heat treatment (b) after heat treatment without silicon and (c) after heat treatment with silicon.

In the T300/pyC-BN samples, the only difference observed from the heat treatment was in the coating adhesion. The BN layer seemed more susceptible to separating from the fibers where they were mechanically agitated. The samples coated in silicon exhibited no morphological differences compared to those without silicon. However, the average thickness of the BN layer reduced from ~400 nm to ~270 nm. The SEM micrographs of these fibers can be seen in **Figure 3.8b-c**.

3.3.4 Tensile Testing

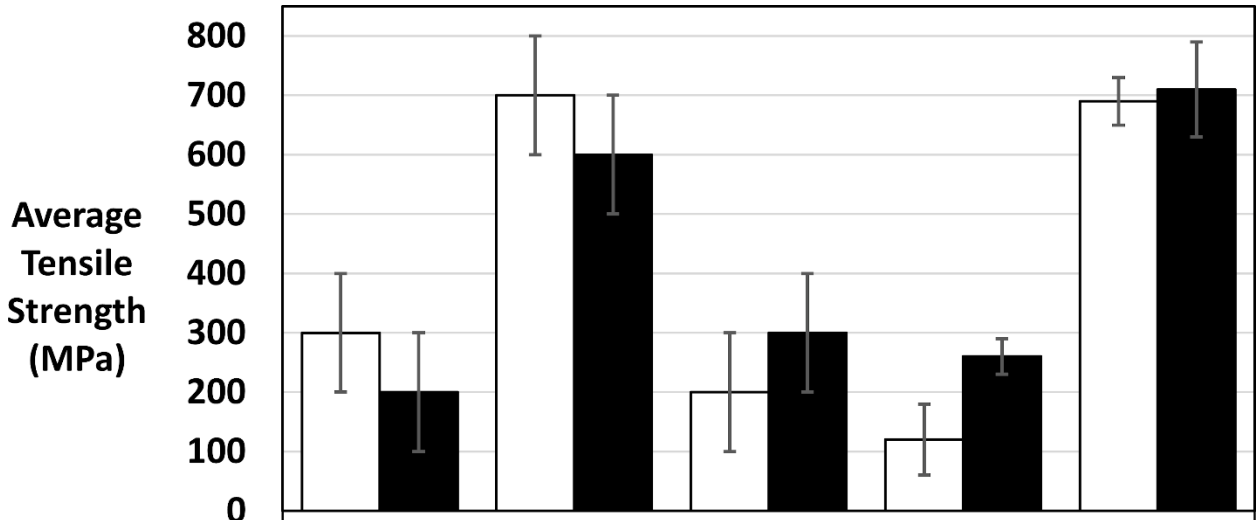

	T300	PyC	PyC-SiC	PyC-TiC	PyC-BN
☐ Without Silicon	300	700	200	120	690
■ With Silicon	200	600	300	260	710

Figure 3.9 Chart of average ultimate tensile strengths for each fiber tow system after heat treatments with and without silicon.

Tensile testing was performed after the heat treatments to compare the ultimate tensile strengths of the protective coating systems with and without silicon coatings (**Figure 3.9**). The strengths were taken and averaged from the load-extension curves as the maximum load before failure. They were normalized based on cross sectional area using the number of fibers per tow, fiber diameter, and coating thicknesses. The T300 carbon fiber tows each have 3000 fibers. Post heat treatment, they were measured to be 6.9 μm in diameter on average. This diameter was used for all fiber systems except the T300 coated with Si, which was measured to be 6.5 μm in diameter on average.

3.3.5 GIXRD

Grazing incidence XRD was performed after the heat treatments on samples that received a silicon coating. **Figure 3.10** shows the stacked XRD patterns of each fiber tow system. When mounting the fiber tow samples to the glass slides before analysis they were unable to lay completely flat. This resulted in the XRD patterns to be shifted. Each pattern was manually aligned using the most intense peak, which was common to all samples. Due to this, only qualitative analysis was performed by comparing relative reflection intensities. The XRD scans ran from 2θ angles of 10 to 80°, but significant reflections were only observed between 15 and 35°. Reflections matching to graphite and silicon were observed. Reflections for SiC, TiC, or BN could not be resolved.

The reflection common to all samples was presumed to be from the graphite (002) plane, which is typically seen at 2θ of 26.38°. In the T300 sample this reflection was quite broad and low in intensity. The reflection was only slightly more intense in the T300/pyC-TiC sample. The T300/pyC-SiC sample exhibited it as relatively sharp, but still low in intensity. The T300/pyC and T300/pyC-BN samples showed it as much sharper and more intense.

A reflection between 28-29° was seen in all samples but T300. This peak was presumed to be due to the silicon (111) planes known to exist at 28.44°. This reflection was most intense for T300/pyC and T300/pyC-BN samples, but almost unnoticeable for T300/pyC-TiC and T300/pyC-SiC samples.

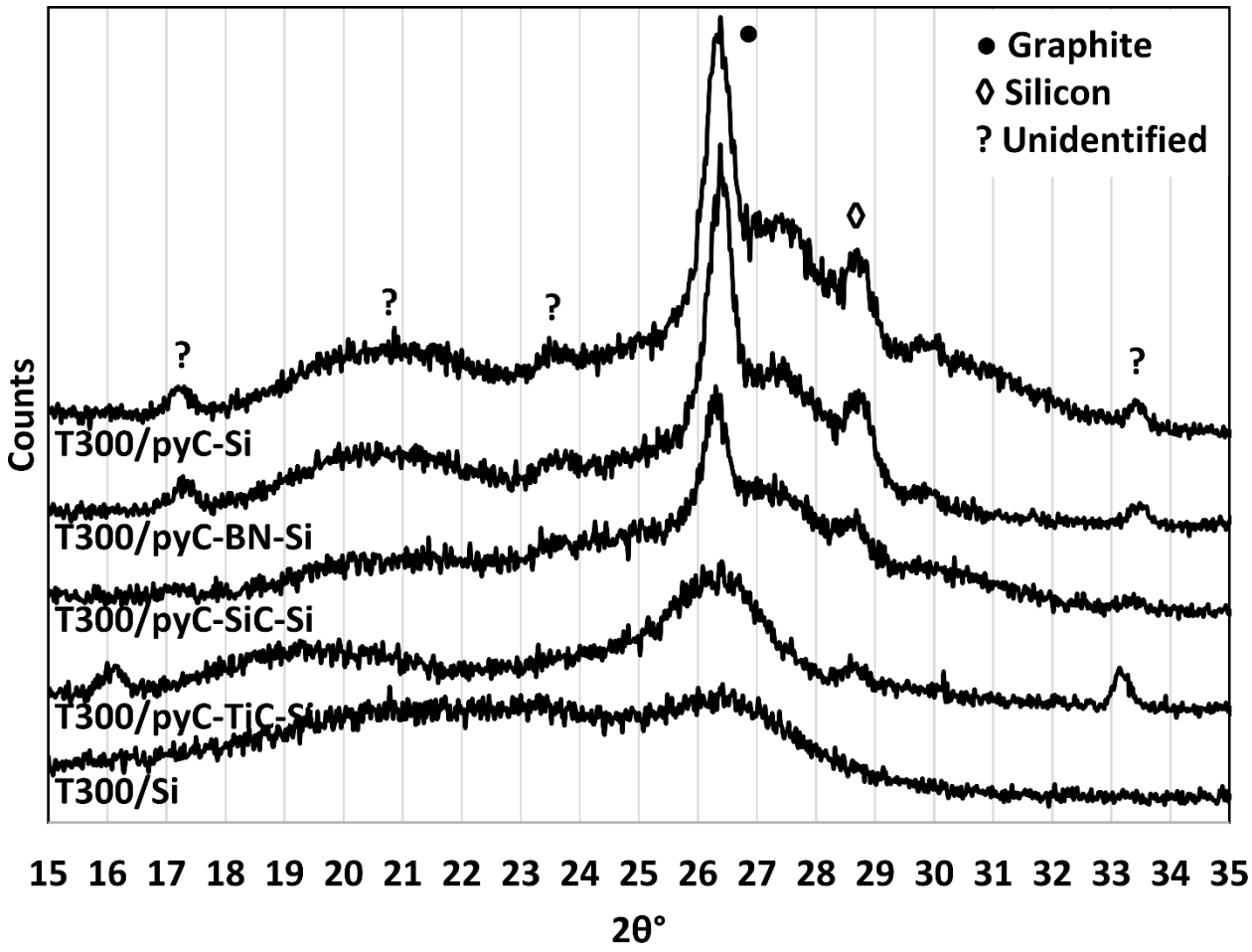

Figure 3.10 GIXRD patterns of all fiber tow systems coated in silicon and heat treated. All patterns were shifted and aligned based on the graphite (002) reflection at 26.38°.

All other reflections were not able to be identified. A low intensity, but relatively sharp reflection was observed between 16-17.5° in the T300/pyC-TiC, T300/pyC-BN, and T300/pyC samples. A very broad hump was common to all samples within 17-25°. A low intensity reflection was seen in T300/pyC and T300/pyC-BN samples. Lastly, a relatively significant reflection was observed between 33-34° for T300/pyC-TiC, T300/pyC-BN, and T300/pyC samples.

3.4 Discussion

This study seeks to investigate the ability of various CVI ceramic coating systems to protect carbon fibers from degradation from molten silicon during the SMI process. Tensile testing of the fiber tow systems after heat treatments proved to be helpful in observing the overall effect that the coatings had on the mechanical properties of the carbon fibers. SEM micrographs were used to visually see the changes that the heat treatments and silicon coatings had on the fiber surfaces. GIXRD patterns were also used to help explain the results of the tensile data.

Property	T300	PyC	SiC	TiC	BN	Si
Elastic Modulus (GPa)	230 [43]	30 [44]	401 [45]	400 [46]	37-100 [47]	130-188 [48]
Contact Angle of Silicon	NO DATA	145° [49]	36° [49]	NO DATA	105-145° [49]	N/A
CTE ($*10^{-6}$ /°C)	-0.41 [43]	< 13 [50]	4.7 [51]	8.4 [51]	7.2 [51]	2.6 [51]

Table 3.4 Various properties of T300 carbon fiber, pyrolytic carbon, SiC, TiC, BN, and Si.

The average strength of the as-received T300 fibers after heat treatment was reduced by the addition of the silicon coating. Although, due to the variation in both measurements the difference is technically not significant. The presumption here is that the silicon reacted with the carbon in the fibers to form SiC. The fibers would become weakened due to the chemical degradation from the silicon. This was supported by the micrographs, which showed rough nodules covering the fiber surfaces in the silicon coated samples but not in the samples without silicon. The micrographs also showed a reduction in fiber diameter from the silicon coating, suggesting that the silicon did in fact degrade the fibers rather than just bead up on the surface.

Since the fiber strengths were normalized to cross sectional area, it may be unexpected that a reduction in fiber diameter would result in a reduction in strength. This may be explained by the more jagged features of the fiber surfaces and the increase in stiffness from the SiC nodules, which could work in tandem to embrittle the fibers. The smoother and more flexible fibers without the silicon coating have fewer nucleation sites for crack formation and are less likely to propagate cracks which do form. Crystalline SiC phases were not observed in the GIXRD pattern of the silicon coated T300. This may be due to a lack of crystallinity of the SiC nodules and/or domination of signal from the bulk fiber.

The pyC coated samples were some of the strongest overall, even with the silicon coating. The increase in strength is likely a result of the coating acting as a sacrificial barrier to crack propagation. Cracks which form on the surface can be redirected around the fiber perimeter from delamination of the coating. This phenomenon is known for pyC interphase coatings and is the reason they are used in composite materials [2, 6, 13]. Evidence of this is seen in the micrographs where the coating has separated from the fiber, leaving it undamaged. PyC is also more elastic compared to the fiber based on their respective elastic moduli (**Table 3.4**). This elasticity may have aided in crack prevention by absorbing some of the load during the tensile tests. However, the average strength was still reduced by the silicon. Again, the variation in strength measurements make this difference technically insignificant. The same effect of silicon degradation of the carbon is expected here as in the as received T300 fibers. Micrographs confirmed this effect, showing the formation of nodules on the coated fiber surfaces by the addition of silicon. Even the samples without silicon became slightly rougher in appearance, suggesting further crystallization of the pyC coating from the heat treatment. Larger crystals were seen in a few areas growing from the fiber surfaces, which was not seen before the heat

treatment. It is possible that some of the pyC converted to the cubic diamond phase of carbon. GIXRD of the silicon coated sample showed a relatively crystallized pyC coating as evidenced by the sharp and intense (002) graphite plane reflection between 26-27°. The reflection comes from the coating and not the fiber because this reflection was not nearly as intense from the T300 sample. These crystallization events may have caused the grains at the fiber/coating interface to merge which could result in embrittlement of the fibers. The XRD reflection between 28-29° indicates the presence of residual unreacted silicon on the surface. This suggests the coating had some part in protecting the fiber. In these tests the quantity of silicon was limited to just a 300-350 nm thick coating. In the actual SMI process the fibers may come in contact with a larger quantity of silicon. The pyC coatings could be completely consumed and lead to fiber degradation similar to what was seen in the T300 sample. The SiC that formed from the reaction with the coating likely will not protect the fibers because a continuous coating was not formed. Rather, rough nodules are formed leaving open space for the silicon melt to further diffuse into the fiber. Again, the SiC nodules did not produce a strong signal in the XRD pattern.

The SiC coated samples without silicon showed a reduction in average tensile strength compared to the T300 fibers without silicon. They were actually identical in strength to the T300 fibers coated in silicon. This may be a result of the higher stiffness of SiC compared to the T300 fiber. Elastic moduli of these materials are listed in **Table 3.4**. The elastic modulus of CVI SiC coatings is over 13 times larger than that of the T300 fiber, making this coating more brittle. This, in combination with the roughness of the coating makes it easy for cracks to form and propagate. Evidently, the pyC layer between the fiber and SiC coating was unable to deflect these cracks and protect the fibers. This could be an indication that the pyC layer has crystallized and merged with the fiber to some degree. Interestingly, the average strength of the samples

coated in silicon was greater than that of the samples without silicon. This indicates that the SiC layer may have successfully protected the fiber from the silicon melt. The micrographs of the silicon coated samples may be able to explain why this may be. Firstly, the SiC coating grew significantly in thickness from ~180 to ~700 nm. Additionally, the surface features of the coating seemed to "smooth out". This smoothing effect was not observed in the samples without silicon. It would seem as though the silicon diffused into and merged with the SiC coating. Silicon has the ability to slightly dissolve layers of SiC [49]. In some areas the SiC coating separated and revealed the pyC coating beneath. Some of this exposed pyC coating was covered in small nodules 100-200 nm in size which resembled the nodules seen in the T300/pyC samples coated in silicon. Some of the silicon may have diffused through the SiC coating and reacted with the pyC coating below. Another possibility is that cracks in the SiC coating allowed the silicon melt to contact the pyC coating, especially since much of the pyC coating was not covered in nodules. Despite the increase in thickness, SiC was still not observed from the XRD pattern. A discrete porous layer was also observed coating the SiC layer, which was presumed to be silicon that had melted and solidified without dissolving the SiC. A reflection for silicon was seen in the XRD pattern confirming its presence. The silicon may be the reason for the increase in strength compared to the T300/pyC-SiC that was not coated in silicon. Silicon is more elastic than both the fiber and the SiC coating, so the residual silicon could have made up for some of the stiffness induced by the SiC.

The TiC coated samples showed the lowest overall strengths on average. The micrographs revealed a large increase in roughness from the heat treatments in samples with and without silicon. This in combination with the high stiffness of TiC make it easy for cracks to form and propagate. The increase in roughness and size of TiC nodules suggests grain growth of

the TiC coating from the heat treatment. In some areas, the TiC coating became discontinuous and exposed the pyC below, making the pyC coating susceptible to attack by the silicon melt. Despite this, the silicon coating actually increased the strength of the TiC coated samples just like in the SiC coated samples. Again, this is attributed to the elastic nature of the silicon compared to the relative stiffness of the TiC and T300 fiber. Despite having low overall strength, the TiC seemed to have effectively barricaded the silicon melt from impacting the fiber. Residual silicon was observed on the fibers from the XRD pattern (although low in intensity). Neither the presence of TiC or a Ti_3SiC_2 MAX phase was observed in any significance.

The BN coated samples showed the most success of all. The ones without silicon were nearly identical in strength to the T300/pyC samples without silicon. This is not surprising considering both coatings were quite smooth and their respective elastic moduli are both less than that of the fiber. The heat treated BN coated samples were more susceptible to separating from the fiber where cross sections were cut compared to the samples prior to the heat treatment. Further crystallization of the coating during heating may have caused it to shift and dislodge from the fiber surfaces. The samples coated in silicon showed no significant change in tensile strength, indicating that the fiber was well protected. The silicon did not increase the strength of the fibers as it did with SiC and TiC coated samples because elasticity was already provided by the BN layer. The only difference observed between the samples with and without silicon was a significant reduction in coating thickness of the silicon coated samples. The BN produced by the CVI method used here is not known to be fully hexagonal, but rather ranging from amorphous to turbostratic [9]. This type of BN is relatively susceptible to oxidation by humidity at ambient temperatures to form B_2O_3 and NH_3. The additional steps required to coat the samples in silicon gave the BN more exposure to the atmosphere and likely caused the BN to oxidize further

compared to the BN in the samples without silicon. The B_2O_3 that formed on the surface would have sublimed during heating above 1000 °C and reduced the thickness of the coating [49]. Evidence of this oxidation was observed in the samples before heat treatment where thin flakes were seen peeling off of the surface. A relatively sharp silicon reflection was seen in the XRD pattern, indicating that it remained on the surface rather than reacting with the BN, pyC, or T300. No significant BN, silicon boride, or silicon nitride reflections were resolved. The BN layer may have lacked crystallinity and/or thickness to stand out amongst the more intense (002) graphite reflection.

Another consideration when selecting a protective coating for SMI is the wettability of the coating by liquid silicon. Wettability is typically quantified by the contact angle of a liquid droplet on a solid surface. A high angle describes a round liquid bead and indicates low wettability. With protective interphase coatings, such a condition would minimize the interaction between the silicon melt and the coating, almost pushing the silicon away from the fibers. The silicon would have difficulty penetrating through cracks in the coating, leaving the fibers well protected. The wetting characteristics of silicon on various ceramics have been reviewed by Drevet and Eustathopoulos [49]. Contact angles are listed here in **Table 3.4**. PyC, which is similar in structure to graphitic carbon is not expected to be wetted by silicon very well, with a contact angle around 145°. However, the reactivity is high enough that SiC will readily form above the melting point of Si. SiC has a significantly lower contact angle with silicon (36°), allowing the silicon melt to wick further into carbon layers. This characteristic is what makes SMI such an effective processing method for SiC matrix formation. The contact angle with TiC is not reported, though Drevet and Eustathopoulos predict that it has similar wetting characteristics compared to SiC due to the structural similarities between the two covalently

bonded carbides. BN has a high wetting angle and low reactivity with silicon, making BN almost ideal as a protective coating.

Characteristics of the coatings when the full C/SiC composite is in use should be considered as well. In the field, the composite will be subjected to highly oxidizing conditions at high temperatures. All of the coatings in this study are expected to oxidize to some degree, but the oxides that are formed will impact the properties of the composite differently. PyC has been reported to oxidize in excess of 400 °C [10], forming CO and CO_2. The evolving gas can induce high internal stresses and leave behind voids, resulting in a weaker composite. Because of this, it is imperative to discourage oxygen and moisture from interacting with the carbon fiber and pyC coating. Both SiC and TiC coatings have previously been reported to inhibit fiber oxidation in carbon fiber composites [10]. However, they both form solid oxides between 500-1300 °C, which leave behind micro-cracks and allow for the penetration of oxygen. These oxides will not melt until beyond 1700 °C, well past the point at which the carbon will oxidize. BN oxidizes to form B_2O_3, which can sublime at elevated temperatures as previously discussed. However, when combined with SiO_2 formed from the SiC matrix, borosilicate glass is produced [10]. Borosilicate melts at around the onset of carbon oxidation, allowing the glassy material to flow and fill in microcracks. Borosilicate also has a low volatility, preventing it from evaporating from the composite, and a high viscosity, allowing for the absorption of stresses on the composite. Borosilicate is perhaps most well-known for its low coefficient of thermal expansion (CTE), minimizing the formation of residual stresses from heating/cooling cycles.

Linear CTE is another factor that should be considered for each of the protective coatings. Residual stresses formed from mismatched CTEs lead to cracking and weakening of the composite. The CTEs of each material are listed in **Table 3.4**. T300 fiber and pyC are said to

have negative CTEs below 300 °C, causing them to shrink upon heating [50]. Beyond this temperature, the CTE gradually increases to positive 10-13 $*10^{-6}$ /°C. SiC is the coating material with the lowest CTE at 4.7 $*10^{-6}$ /°C. BN and TiC are both higher at 7.2 and 8.4 $*10^{-6}$ /°C, respectively.

3.5 Conclusions

Carbon fiber tows were CVI coated with various protective ceramic coatings to produce the following samples: T300 (as-received), T300/pyC, T300/pyC-SiC, T300/pyC-TiC, and T300/pyC-BN. In order to simulate the SMI process, some of the samples were coated in silicon using thermal evaporation. The coated fiber tows, both with and without silicon, were then heat treated to 1550 °C for 1 hour under flowing argon atmosphere. The ultimate tensile strengths of the heat treated samples were measured and their surface morphologies were analyzed using SEM. The silicon coated samples were also analyzed using GIXRD.

The unprotected T300 samples showed a drop in average tensile strength from the addition of silicon. The SEM micrographs showed that the samples without silicon remained smooth, but the samples with silicon developed a rough nodular surface morphology. The fiber diameter also decreased by ~6% confirming silicon degradation of the fibers. These fiber samples did not display crystallinity in the XRD results.

T300/pyC and T300/pyC-BN samples had the highest tensile strengths on average. This was attributed to the smoothness and relative elasticity of the coatings, as well as their ability to redirect cracks from propagating through the fibers. The addition of silicon caused a reduction in average tensile strength for the T300/pyC samples. Micrographs revealed the formation of rough nodules on the fiber surfaces, likely to be silicon carbide from the reaction between the molten silicon and pyC coating. However, SiC could not be resolved in the XRD pattern for these

samples. The BN coated fibers did not show this reduction in tensile strength from the silicon, indicating that the fibers were well protected. Oxidation of the only partially crystalline BN coating resulted in a decrease in thickness, but did not impact the strength or morphology of the samples. BN reflections could not be resolved from the XRD data.

The SiC and TiC coated samples were both relatively weak in average tensile strength, but exhibited an increase in strength from the addition of silicon. The coatings were both relatively rough prior to heat treatment. SiC seemed to be unaffected by the heat treatment, but TiC became noticeably rougher in the micrographs. Both materials have high elastic moduli making them brittle compared to the fibers and other coatings. The rough and brittle nature of both carbide coatings may have facilitated the formation and propagation of cracks during testing. Silicon, which is more elastic than the carbide coatings and was observed on the fiber surfaces from the XRD patterns may have strengthened the fibers by allowing for energy absorption during testing. Evidence of Si diffusion through the SiC layer was seen in the micrographs. The TiC coatings seemed to be unaffected by the silicon, suggesting proper protection of the carbon fibers. Smoother morphologies for both coatings may very well lead to more successful tensile results.

Overall, the BN coated fibers showed the most promise. Amorphous to hexagonal BN has the additional benefit of low wettability and reactivity with liquid silicon, which further prevents the silicon melt from reaching the fibers through micro-cracks. PyC is not well wetted by silicon, but it readily reacts to form SiC which is very well wetted. The oxide of BN, when mixed with silica, also forms a low volatility high viscosity borosilicate glass. This property allows further oxidation protection of the fibers at elevated temperatures. From a CTE standpoint, BN closely matches that of the carbon fibers and pyC coating.

Chapter 4

Chemical Vapor Infiltration of a Boron Carbide-Pyrolytic Carbon Mixed Matrix System

4.1 Introduction

Carbon fiber reinforced carbon matrix composites (C/C) are exceptional high temperature materials. They stand apart from other high temperature composites due to the high strength of carbon fibers, high thermal conductivity of pyrolytic carbon (pyC), and low thermal expansion coefficient [1, 23, 50, 52]. This set of properties has earned them use as aircraft and high-end car brakes, nuclear power radiation absorption, rocket nozzles, re-entry shields, and heat exchangers [1, 50, 52-54].

In these types of applications, it is important to select the right materials as well as engineer them to optimize for the transfer and absorption of heat. Heat transfer should be rapid and should be directed out of the material and away from parts of the assembly made from materials that cannot withstand such high temperatures. This can be done by designing the fiber preform architecture to channel heat through the carbon fibers to the outside of the composite where it can be dissipated to the atmosphere. Heat channeling can also be done at the matrix level by producing a pyC microstructure with the most effective heat transfer capabilities, such as rough laminar or regenerative laminar [54-56].

The heat absorption capabilities of C/C composites could be enhanced by the addition of boron carbide (B_4C) in the matrix. Proper heat absorption helps to minimize the temperature of the composite part while in use, thereby reducing the rate of degradation and maximizing its lifetime. B_4C is a high temperature ceramic, which is thermally stable to around 2450 °C and is

typically recognized for its impressively high hardness, making it a highly wear resistant material. B_4C has also been acknowledged for its neutron absorption capabilities [57-59]. What makes this carbide a truly great addition to C/C is its specific heat capacity of 1288 J/kg/°C, compared to graphite which is 717 J/kg/°C [51]. A C/C composite with a mixed pyC-B_4C matrix could potentially optimize both heat transfer as well as heat absorption for use in many applications.

C/C composites are typically made using either the polymer infiltration & pyrolysis method (PIP) or the chemical vapor infiltration method (CVI) [1]. In PIP, a carbon fiber preform is infiltrated with a carbon-based polymer, which is then pyrolyzed at high temperatures to form the carbon matrix. The properties of the carbon matrix are determined by the type of polymer and the pyrolysis conditions. To incorporate B_4C into a PIP carbon matrix, a B_4C powder slurry would simply be made from the polymer and used for the infiltration steps. In CVI, hydrocarbon gases are flowed through the preform at high temperatures to crack the molecules and deposit carbon on the fiber surfaces. Here, the properties of the matrix depend on many parameters of the CVI process such as temperature, pressure, gas residence time, and gas composition. The most favorable pyC microstructures, rough laminar and regenerative laminar, have been produced through careful control of these CVI parameters, but have never been made using the PIP method. The incorporation of B_4C into a CVI carbon matrix is more complicated than simply adding a powder filler.

Boron carbide is most commonly produced by the thermal reaction between carbon and boric acid, but can also be produced using low pressure CVI much like pyC [57-61]. This has been done at temperatures as low as 900 °C using a BCl_3-CH_4-H_2 gas feed. With this precursor system, Zeng et al. [61] demonstrated that under certain CVI conditions B_4C and pyC can

actually be deposited simultaneously. Phase pure B_4C was produced at the lower temperatures of 900 and 950 °C, but a mixture of B_4C and pyC was produced at the higher temperatures of 1000 and 1050 °C. X-ray diffraction (XRD) patterns of the materials showed an amorphous phase for all temperatures, presumed to be B_4C. In the 1000 and 1050 °C samples, sharp graphite reflections appeared, suggesting the presence of pyC in addition to the B_4C. The two materials could be seen visually in SEM micrographs of the mixed coating as separate phases within the coating. The ratio of B:C in the coating as measured by EDS varied as a function of temperature and mole ratio of BCl_3:CH_4 in the gas mixture. This suggests that a mixed B_4C-pyC matrix can be produced via low pressure CVI and its composition can be controlled by tuning the CVI parameters. This makes it possible to develop a wide variety of mixed matrix systems such as alternating layers of B_4C and pyC, a continuous layer of mixed B_4C-pyC, or pyC matrix with pulses of B_4C-pyC. The latter system may be optimal for tribological applications where too much B_4C could diminish the thermal transfer properties of the matrix and only sparsely scattered pockets of B_4C are necessary for adequate heat absorption. With proper pyC microstructure, heat could be directed towards the B_4C pockets to be absorbed.

This study seeks to investigate ways of controlling the B_4C-pyC mixed matrix by adjusting CVI parameters. A preliminary set of CVI runs was performed here to try to reproduce results from the Zeng study and learn what may be done to control the matrix properties. Control over the B_4C content, stoichiometry, and grain size is important for optimizing the heat absorption capabilities of the matrix without impacting other matrix properties. Favorable pyC microstructures should be reproduced by the mixed-matrix CVI for adequate heat transfer.

4.2 Experimental

4.2.1 CVI of Matrix

CVI was carried out using the setup described in **Section 3.2.1** (**Figure 3.1**). CVI gas precursors were BCl_3 (chemically pure, 99.9%) and CH_4 (ultra-high purity, 99.99%). CVI process gases were H_2 and N_2 (ultra-high purity, 99.999%). 3K T300 ex-PAN carbon fiber tow substrates (TORAYCA®) were used for all depositions. Process conditions were based off of Zeng at al. [61]. The gas molar ratio of BCl_3:CH_4, BCl_3:H_2, and BCl_3:N_2 in the inlet stream were kept constant for all runs at 5:1, 1:2, and 1:2, respectively. Deposition temperature was isothermal and ranged from 900-1050 °C. Process pressure was isobaric and controlled at either 1 or 75 torr for different runs. Reaction time was held constant at 5 hours. Process conditions for all runs are summarized in **Table 4.1**.

BCl_3:CH_4	BCl_3:H_2	BCl_3:N_2	P (torr)	T (°C)
5	0.5	0.5	1	900
5	0.5	0.5	1	950
5	0.5	0.5	1	1050
5	0.5	0.5	75	900
5	0.5	0.5	75	950
5	0.5	0.5	75	1000

Table 4.1 Summary of CVI process parameters for all runs performed.

4.2.2 Characterization

Scanning electron microscopy (SEM) images were taken of the coated fibers to observe the coating morphologies. A ThermoFisher TeneoLoVac Field Emission SEM operating at 10-20 kV and 0.4-1.6 nA was used. Elemental analysis of the coatings was performed using Energy Dispersive X-ray Spectroscopy (EDS) with EDAX Team™ software.

To analyze the crystallinity of the CVI coatings, grazing incidence X-ray diffraction (GIXRD) was used. A SmartLab X-ray Diffraction System was used with a grazing angle of 0.2° scanning from 2θ 20-70°.

4.3 Results

4.3.1 Micrographs

The primary factor influencing the coating morphology was pressure. Coatings deposited at 1 torr (**Figure 4.1**) were rough and granular in appearance while coatings deposited at 75 torr (**Figure 4.2**) were smooth with scattered occurrences of urchin-like structures.
The 1 torr runs produced coatings made up of relatively large crystallites (~1 μm) evenly covering the fiber surfaces. Coating thickness increased with temperature. Cross sections of the carbon fibers at all temperatures appeared jagged and degraded.

The coatings at 75 torr were much smoother compared to 1 torr, but the formation of urchin-like structures occurred at 900 and 950 °C. These structures seemed to grow outwards radially from a central point on the fiber surfaces into many long whiskers terminating at a sharp point. Some were seen growing from the smooth coatings, while others were seen growing directly from the fibers. The urchins were most frequent at 900 °C, less at 950 °C, and not seen at all in the 1000 °C coatings.

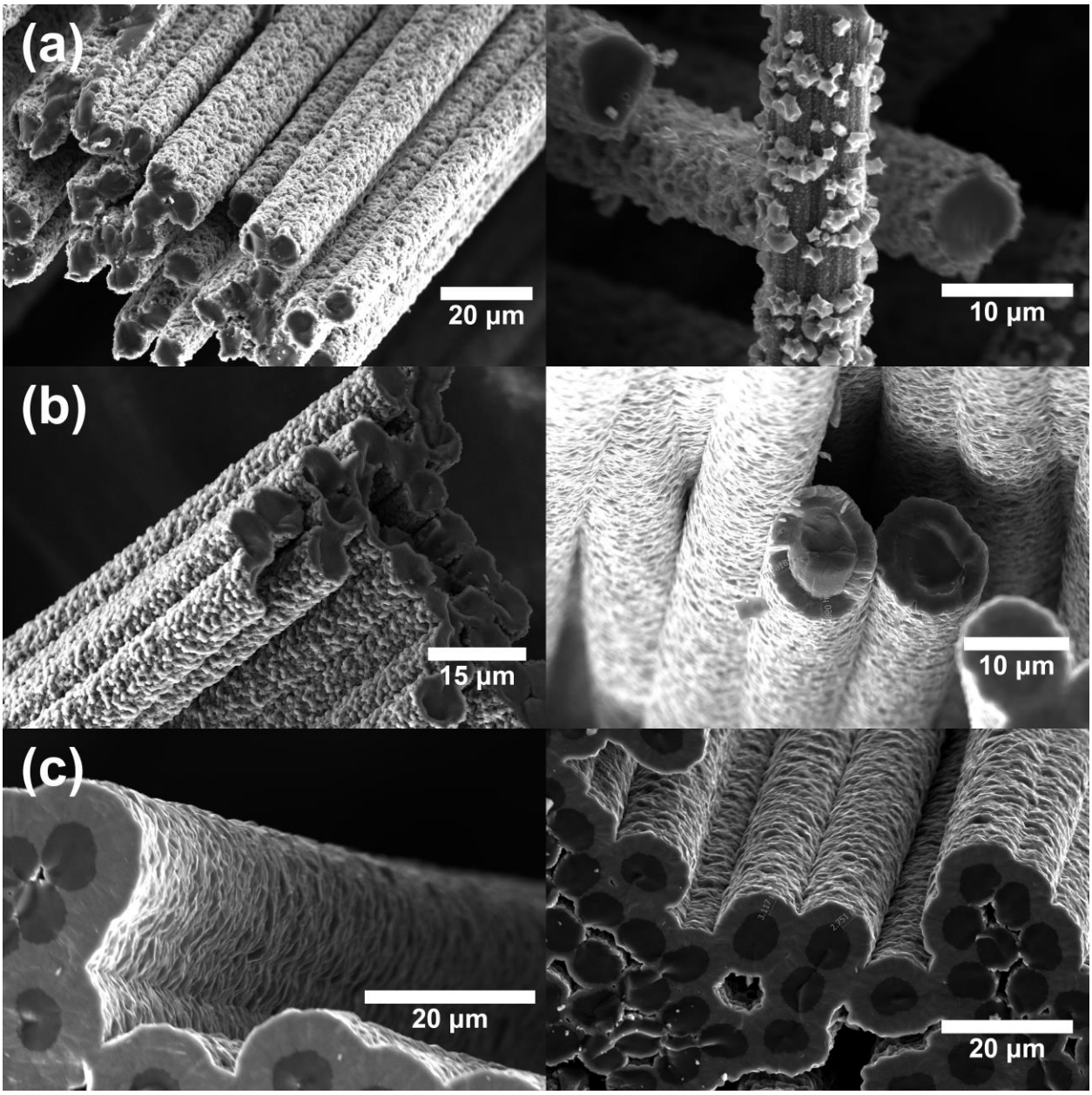

Figure 4.1 CVI coatings performed at 1 torr and (a) 900 °C (b) 950 °C (c) 1050 °C.

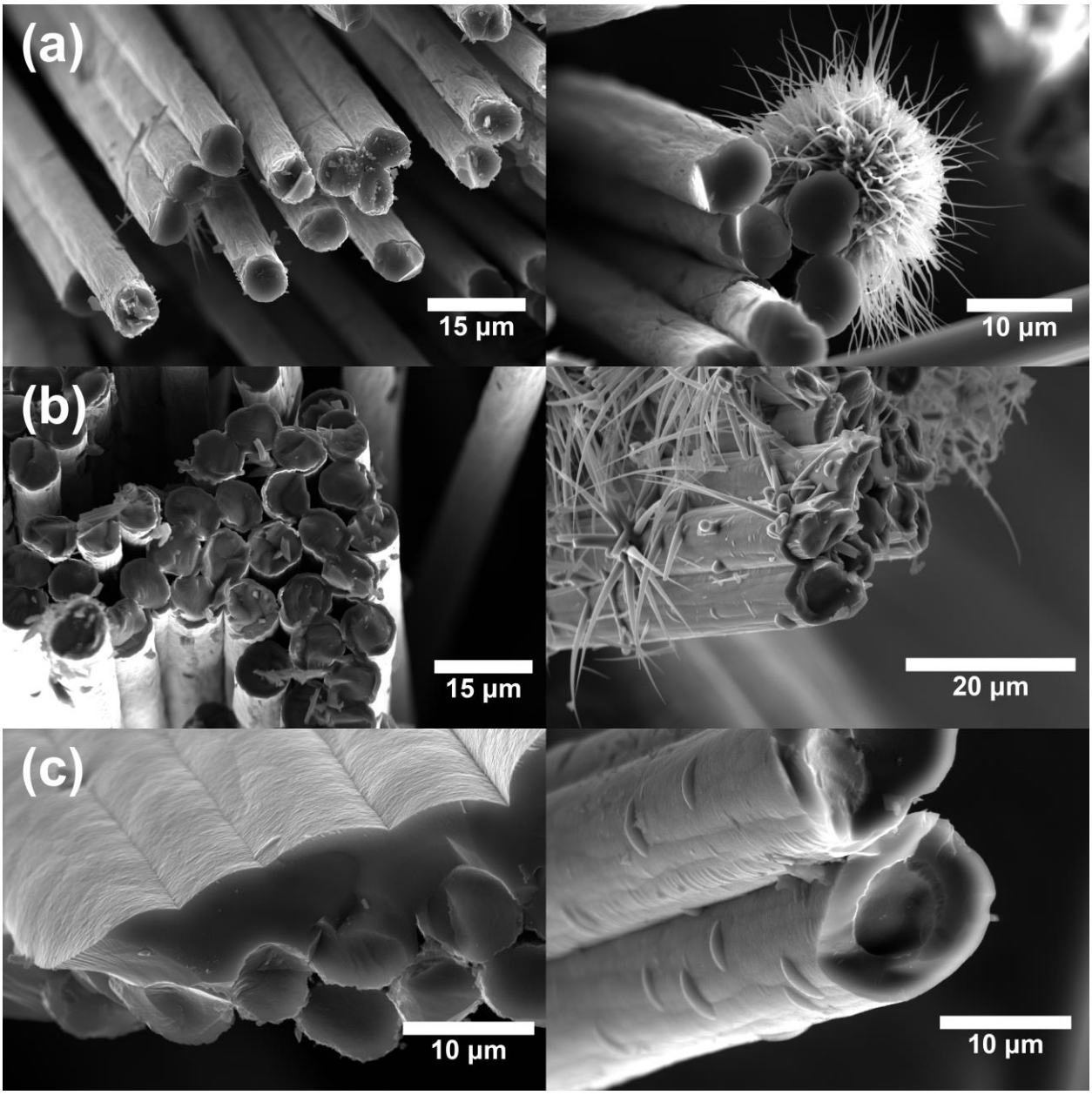

Figure 4.2 CVI coatings performed at 75 torr and (a) 900 °C (b) 950 °C (c) 1000 °C.

4.3.2 Coating Composition

EDS was used to compare the elemental compositions for two of the 75 torr coatings: 900 and 1000 °C. The atomic ratios of boron to carbon in the coatings was calculated from the EDS spectra. B:C averaged ~1:2 for 900 °C and ~1:1 for 1000 °C. B:C for the urchin structures in the 900 °C run was ~1:1.

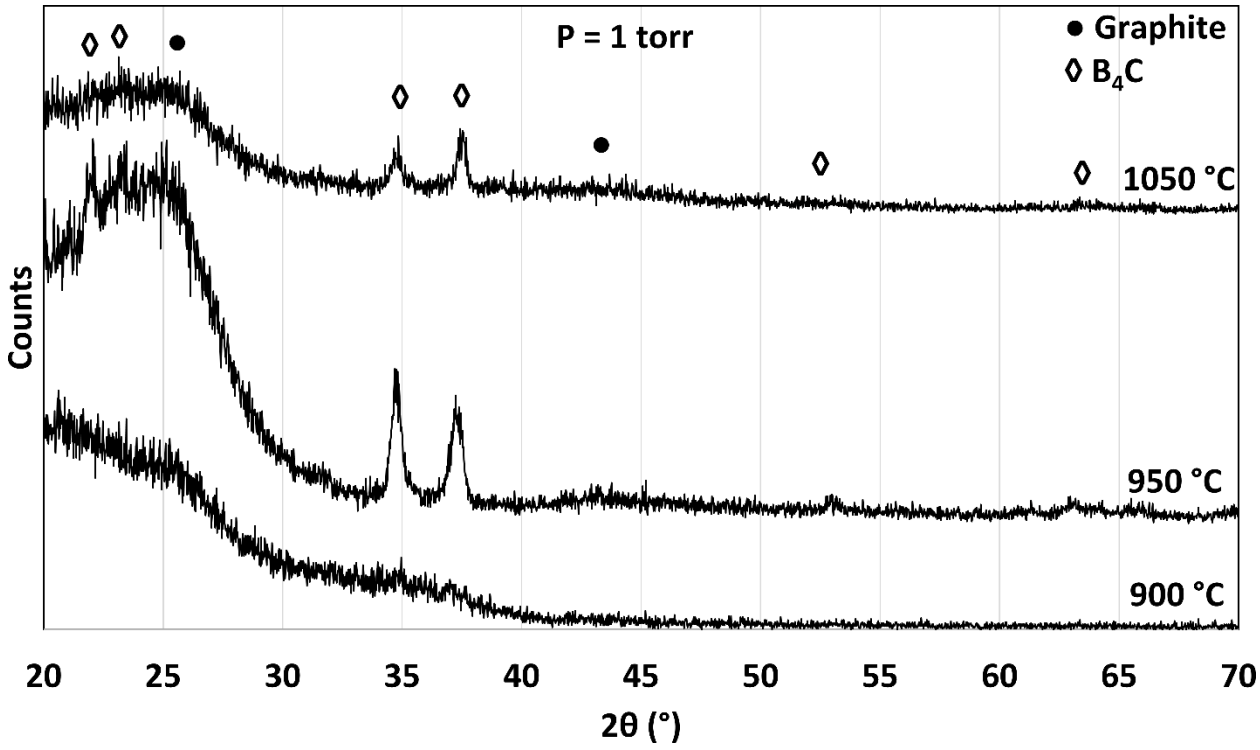

Figure 4.3 GIXRD patterns for the fiber tows coated at a pressure of 1 torr.

Temperature also had an influence on the XRD patterns for the samples coated at 1 torr (**Figure 4.3**). At 900 °C, no crystalline phases were present. Broad humps were observed from ~20-30°, roughly correlating to the graphite (002) reflection [62], and from ~33-38°. At 950 °C, the 20-30° hump grew in intensity and developed somewhat of a peak around 22°, which correlates to the B_4C (003) reflection [63]. Instead of a broad hump around 33-38°, two sharp

peaks around 35 and 38° were present. These correlate to the B_4C (104) and (021) reflections, respectively. The pattern for the 1050 °C sample was similar to that of the 950 °C sample, but with lower intensity.

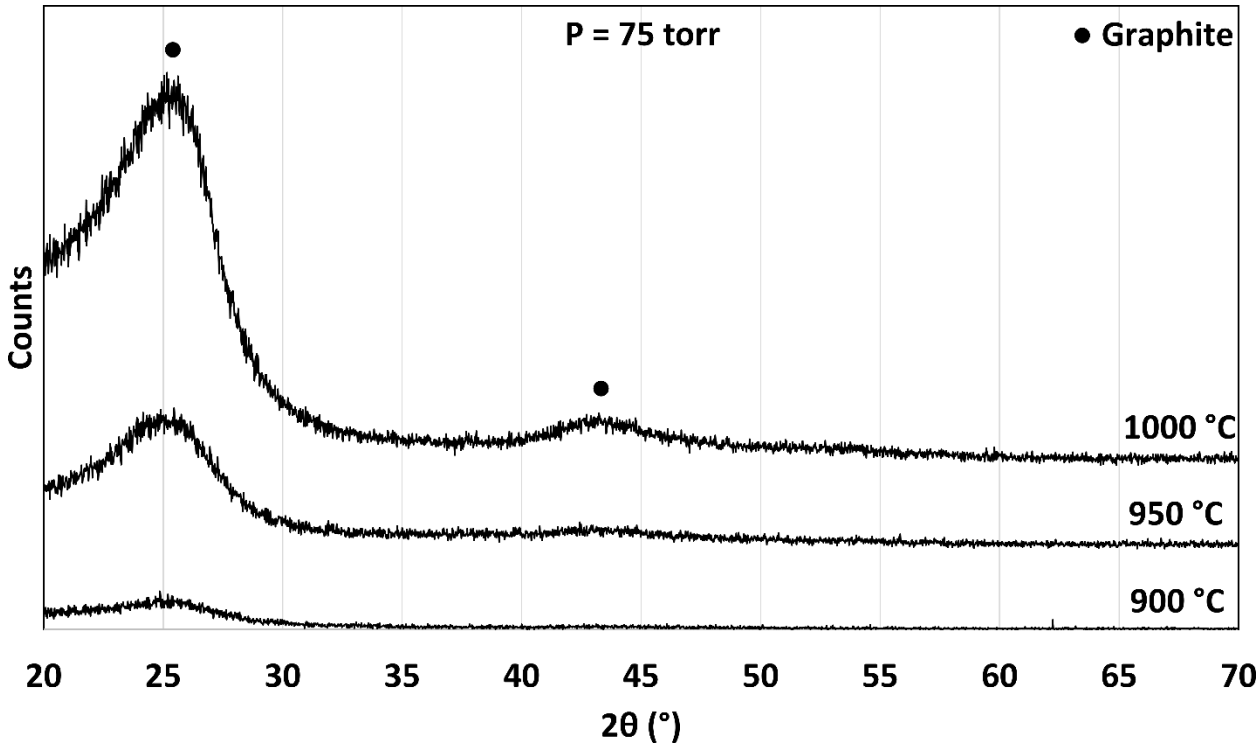

Figure 4.4 GIXRD patterns for the fiber tows coated at a pressure of 75 torr.

The GIXRD patterns for the samples coated at 75 torr (**Figure 4.4**) did not display any crystalline phases at any temperature. Broad humps were seen ~20-30° and ~40-45°. These roughly correlate to the graphite (002) and (101) reflections [62]. Both humps were more intense at higher temperatures.

4.4 Discussion

Carbon fibers were CVI coated using BCl_3, CH_4, H_2, and N_2 gases at different temperatures and pressures. CVI parameters were based off of a study by Zeng et al. [61] who were able to simultaneously deposit both pyC and a-B_4C. This study seeks to further understand how to control the composition and morphology of these coatings. Zeng at al. performed all depositions at 75 torr. For comparative purposes, this study used both 75 and 1 torr.

The carbon fibers were degraded by the coating process under all CVI conditions. At 1 torr, the fibers took on a more jagged cross-sectional shape and the coating seemed to be continuous with the fiber. At 75 torr, some of the urchin structures were observed growing directly from the fibers. Based on the EDS results, these structures were shown to have a substantial boron content. In both pressure regimes, the BCl_3 likely reacted with the fibers to form boron carbides. Any CMC part made using this process would require protective interphase coatings on the carbon fibers first, as described in **Chapter 3**.

The lower pressure coatings were rough and rigid in appearance. The higher temperature coatings were thicker due to the reaction kinetics. At higher temperatures, the reaction rate will be faster and thicker coatings will develop for the same reaction times [35]. The higher temperatures also gave rise to crystallinity in the coating, indicated by the XRD patterns. Crystallites were all identical in appearance suggesting that phase-pure boron carbide was being deposited, rather than a mixture of pyC and boron carbide. This type of coating was not reported in the Zeng paper because they did not operate at this low of a pressure. The exact stoichiometry of the boron carbide was not measured, but the XRD reflections match with that of "technical boron carbide". This form of cubic boron carbide is commonly notated as having a B_4C stoichiometry, but actually exists on a spectrum from B_4C to $B_{10}C_4$ [59, 60]. Since pyC was not

being deposited under these conditions, this type of process would be used when discrete B_4C layers were needed. These layers could be used as fiber interphase coatings, alternating pyC-B_4C layers in the matrix, or environmental barrier coatings (EBCs) encapsulating the entire composite. This could be useful for nuclear power applications because the continuous B_4C coatings would effectively shield the carbon fibers. Used on the surface as an EBC, such a coating would be great for absorbing heat which builds up at the surface and cannot dissipate into the atmosphere quickly enough, like in heat shields and rocket nozzles [12]. However, a continuous rough coating of a material as stiff as B_4C could embrittle the composite. Structural applications with excessively high loads may be avoided, such as certain engine components. This may also not work for brake discs. PyC and B_4C would be unevenly distributed throughout the composite, so the discs wear and friction properties would likely have a high degree of variability.

The higher-pressure coatings were much different in appearance and composition. They were smooth rather than grainy and contained the urchin structures. Crystalline boron carbide was not observed from the XRD results, but the EDS results showed that both the coatings and the urchins contained significant quantities of boron. When the urchins were present, they had a higher ratio of B:C compared to the coatings. These structures were less common at higher temperatures, not being observed at all at 1000 °C. This suggests that higher temperatures encourage boron incorporation in the coating, while lower temperatures encourage urchin growth. It is not known if the smooth coatings are homogeneous in composition or contain distinct regions of pyC and B_4C, like what was observed by Zeng at al. [61]. The higher temperature coating could be used to make a continuous matrix with consistent B_4C content throughout. The quantity of B_4C may be controlled by adjusting the gas inlet stream, according

to results from the Zeng paper. Without rough crystalline B_4C coatings, the mechanical properties of the fibers would be impacted less. This could make for a good brake material because the wear and friction properties would be more consistent due to the homogenous matrix. However, simultaneous control of both the B_4C content and the pyC microstructure would be difficult. It may not be possible to optimize both properties.

The high-pressure low-temperature regime may be further optimized to eliminate the smooth coating and only produce the urchin structures. The urchins could be incorporated into a pyC matrix by using pulses of the B_4C CVI. A pre-established pyC CVI process would be used to produce a matrix of whatever desired microstructure. The urchins would be evenly scattered throughout the matrix and enhance its thermal properties without affecting its composition or microstructure. They would have little to no impact on the mechanical properties of the fibers and could stop or deflect crack propagation as hard blunt particles in the matrix. This type of composite could be practical for any application of C/C materials and may be the best choice for brake discs since there is control over both the pyC microstructure and B_4C content in the matrix.

4.5 Conclusions

Coatings containing B_4C were applied to carbon fibers under different CVI conditions, leading to different coating compositions and microstructures. The CVI process at 1 torr produced rough, crystalline B_4C continuous coatings. PyC was not deposited alongside the B_4C. These phase-pure B_4C coatings could be used to deposit discrete layers of B_4C within a C/C composite. Future studies should investigate the *actual* stoichiometry of this boron carbide. Smoother coatings were produced at 75 torr, which more closely resembled the coatings produced by Zeng et al. [61]. They were not crystalline, but contained boron and an excess of carbon. The exact microstructural properties of these coatings are not yet understood and should

be further studied and controlled. At 900 and 950 °C, urchin-like structures with high boron content were produced alongside the smooth coatings. These structures could be used to produce a matrix that is predominantly pyC with B_4C particles evenly scattered throughout. More work is needed to optimize the CVI conditions to produce just the urchin structures without the coating. At 1000 °C there were no urchins and the smooth coating had a higher boron content. This type of coating could be used to produce a continuous homogenous matrix containing both pyC and B_4C.

Chapter 5

Development of a Ferromagnetic SiC/SiC Ceramic Matrix Composite

5.1 Introduction

Continuous fiber reinforced ceramic matrix composites (CMCs) have proven to be exceptional high temperature structural materials. The numerous benefits of their thermal, mechanical, and chemical properties are undisputed. However, little work has been done to integrate CMCs with electronic equipment such as sensors or actuators because most high temperature ceramics lack adequate electrical and magnetic properties. CMCs with magnetic properties could expand their usage into other high temperature applications including sensors, actuators, information storage, and MEMS used in automotive, aerospace, or power generation [64-67]. Even certain biological applications like drug delivery could benefit from the chemical inertness of CMCs [66].

Polymer-matrix and metal-matrix composites have previously been made with dispersed magnetic particles [68, 69]. However, CMCs have a different set of challenges associated with incorporating magnetic particles during processing and keeping them from oxidizing when in use at high temperatures. Metal-ceramic composites in which metallic particles are dispersed in a ceramic matrix have been previously studied [65, 67, 70-73]. The addition of the metal particles to monolithic ceramics has been shown to benefit the mechanical properties of the material [73]. These same benefits can be expected to apply to CMCs with metal particles as well. The metal-ceramic composites have been made using pre-ceramic polymers. Hauser et al. [65] milled iron and cobalt particles together with cured polymer and pyrolyzed the mixture into a ceramic puck.

The material had good magnetic properties, but this method could not be applied to CMCs because the solid mixture cannot be effectively infiltrated into ceramic fibers. Magnetic particles have also been mixed in with liquid pre-ceramic polymers before curing and pyrolyzing together [67, 73]. A polymer slurry such as this could then be infiltrated into fibers using the PIP process, but it is not ideal. It can be difficult to suspend solid particles in the polymer and prevent them from agglomerating and sinking to the bottom of the container [72]. This would lead to a matrix with an inconsistent distribution of magnetic particles. This is especially true if large/agglomerated particles cannot infiltrate properly and are "filtered out" by the fibers. Another method is to incorporate metals into pre-ceramic polymers as side-chain groups [65, 70, 71]. Hauser et al. did this by reacting a SiCN-forming polymer with metal carbonyls and pyrolyzing to form metal-SiCN composites. Unfortunately, the reaction product was solid prior to pyrolysis and could not be used to make a PIP CMC. Kulbaba et al. [70] and MacLachlan et al. [71] synthesized liquid silane pre-ceramic polymers with metallic functional groups. The polymers were successfully pyrolyzed to produce ceramics with even magnetic particle distribution and good magnetic properties, but were not demonstrated for CMCs.

The only published accounts of magnetic fiber reinforced CMCs have been from the Suib research group [74, 75]. Gottlieb achieved this by applying a cobalt interphase coating to ceramic fibers [74]. This was done by coating the fibers in cobalt (II) nitrate aqueous solution and reducing to cobalt with hydrogen. A SiO_2 protective interphase was then coated over the cobalt via CVI before applying a CVI SiC matrix. Kmetz et al. applied a magnetic interphase coating by dissolving cobalt (II) acetate in a mullite sol-gel [75]. Ceramic fibers were soaked in the modified sol-gel, dried, then heated under hydrogen. The cobalt (II) acetate reduced to cobalt metal particles dispersed in a mullite coating. A PIP ceramic matrix was then applied to the

magnetic fibers. The magnetic properties of the CMCs in these two methods were well maintained after high temperature oxidation testing. However, multiple additional steps had to be performed to apply the magnetic coatings, adding complexity to the fabrication process. Additionally, the ferromagnetism was weakened by the addition of the matrix.

A more effective approach may be to incorporate the magnetic particles in the matrix rather than as a thin film coating, which is the focus of this study. This was done by dissolving cobalt salts in a SiC-forming pre-ceramic polymer and using the PIP process to apply a SiC matrix to SiC fibers. Cobalt was chosen as the magnetic material due to its relatively high curie temperature, allowing it to maintain its magnetic properties in excess of 1100 °C [76]. The reduction of the cobalt salts to cobalt metal and pyrolysis of the polymer was done in a single step to reduce complexity of the process. A stronger magnetic response is to be expected compared to the previously reported magnetic interphase coatings and oxidation protection of the magnetic particles is still provided by the ceramic matrix. Environmental barrier coatings (EBCs) can be used for additional oxidation protection of the cobalt particles as well as the rest of the CMC. Since a polymer solution is used rather than a polymer slurry of insoluble particles, distribution of the magnetic particles is expected to be more homogenous.

5.2 Experimental

5.2.1 Polymer Solutions

Pre-ceramic polymer solutions were made for dip-coating onto fiber tow samples. The polymer was KDT Ceraset® Polysilazane 20 [77]. This commercial polymer forms SiC when pyrolyzed to 1000 °C under inert atmosphere or Si_3N_4 under ammonia atmosphere. Its formulation and solvent system are proprietary. Cobalt-salts were mixed into the polymer by

adding 20% by mass and stirring until fully dissolved. $CoCl_2$ and $CoBr_2$ salts were used, procured from Fisher Scientific (anhydrous, 97% pure).

5.2.2 Polymer Infiltration & Pyrolysis

CG-Nicalon^{TM} fiber tows were infiltrated with the polymer-salt solutions by dip-coating the tows in the solution and gently pressing the polymer into the fibers. The infiltrated tows and excess polymer solutions were cured under vacuum to 200 °C. The green mini-composites and polymer pucks were then heat treated to 1000 °C under flowing H_2 for 5 hours in a tube furnace. The heat treatments served to both pyrolyze the polymer and reduce the Co-salts into Co metal. Three infiltration and pyrolysis cycles were performed on the mini-composites.

5.2.3 Oxidation Testing

Mini-composites were given either SiO_2 or SiC protective EBCs for oxidation testing of the magnetic matrix. The SiO_2 EBC was applied by dip-coating the mini-composite into a silica-ethanol based sol-gel. The coating was dried at room temperature under vacuum. The SiC EBC was applied by dip-coating the mini-composite into the polysilazane pre-ceramic polymer and pyrolyzing to 1000 °C under H_2 for 2 hours.

Oxidation testing was performed on $CoBr_2$-based mini-composites with SiO_2 EBC, SiC EBC, and no EBC. The samples were calcined in an open tube furnace to 1000 °C for 10 hours.

5.2.4 Characterization

To test if the mini-composites were magnetic or not, a permanent magnet was held close to the fibers to see if they would stick or move. Powder X-ray diffraction (XRD) was performed on the pyrolyzed polymer to observe the presence of metallic cobalt and other species. A Rigaku Ultima IV diffractometer (Cu Kα radiation, $\lambda = 1.5406$ Å) was used with an operating voltage of 40 kV

and a current of 44 mA. Energy Dispersive X-ray Spectroscopy (EDS) was used with EDAX Team™ software to perform elemental analysis on the pyrolyzed polymer.

5.3 Results

The initial SiC-forming pre-ceramic polymer used in this study was StarPCS™ SMP-10 polycarbosilane from StarFire Systems. Cobalt salt solutions from this polymer were attempted using anhydrous cobalt (II) acetate, chloride, and bromide. None of the salts were soluble in the polymer and quickly sunk to the bottom. When the KDT Ceraset® Polysilazane 20 was used, cobalt (II) chloride and bromide both showed solubility, while cobalt (II) acetate again sunk to the bottom. Neither SMP-10 nor cobalt (II) acetate were used for further studies.

5.3.1 Mini-Composites and Polymer Pucks

Mini-composites were made by infiltrating SiC fibers using the solutions of Polysilazane 20 with $CoCl_2$ or $CoBr_2$ and pyrolyzing to 1000 °C under H_2 (**Figure 5.1b**). SiC pucks were made by pyrolyzing the excess polymer solutions under the same conditions (**Figure 5.1a**). All samples exhibited ferromagnetic properties when a permanent magnet was held close.

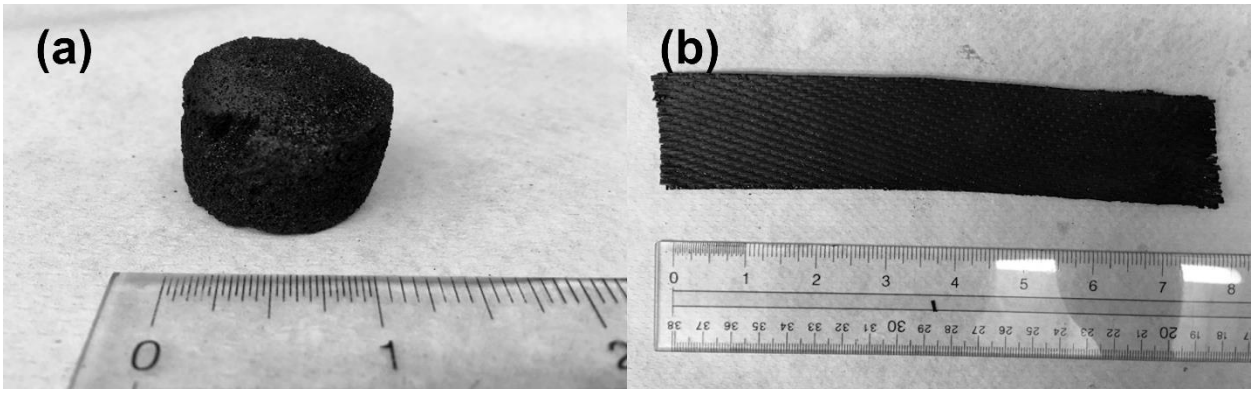

Figure 5.1 (a) SiC puck made from pyrolyzed polymer-salt solution. (b) Mini-composite made by infiltrating polymer-salt solution into SiC fibers and pyrolyzing.

5.3.2 Characterization

EDS was performed on the pyrolyzed polymer-salt solutions made from $CoCl_2$ and $CoBr_2$. The atomic ratios of X/Co (where X = Cl or Br) were calculated from the EDS results. This ratio was ~1.3 Cl/Co and ~0.7 Br/Co.

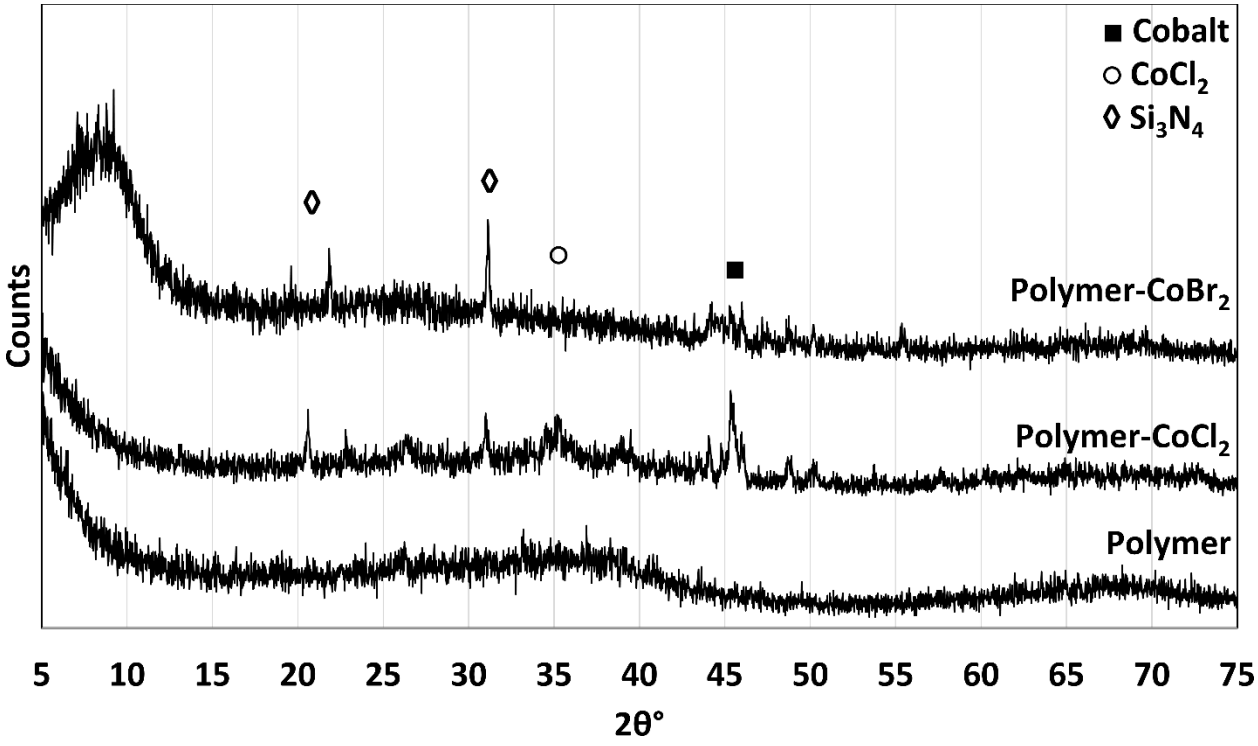

Figure 5.2 Powder XRD patterns of the pyrolyzed polymer solutions.

Powder XRD was performed on the pyrolyzed polymer-salt solutions as well as the pyrolyzed polymer without cobalt salts (Figure 5.2). No crystallinity was observed in the sample without cobalt salt. In the pyrolyzed polymer-salt solutions, a series of minor reflections were present between 44-50°. These were attributed to the face-centered cubic (FCC) and hexagonal close packed (HCP) crystal structures of cobalt, which both have reflections in the same region. These reflections were stronger in the $CoCl_2$ pattern compared to the $CoBr_2$ pattern. A reflection

for $CoCl_2$ was identified around 35°. Both of the patterns for the samples with cobalt salts also had reflections around 21° and 31°, which loosely match with Si_3N_4.

5.3.3 Oxidation Testing

From the EDS results, the $CoBr_2$ polymer solution had a better conversion to cobalt metal, so this system was used for oxidation testing. Samples for oxidation testing were prepared with a SiC protective coating, SiO_2 protective coating, and without protective coating. After calcining to 1000 °C for 10 hours, the magnetism of the samples was tested by holding a permanent magnet close. All three samples exhibited ferromagnetism this way after the oxidation testing.

5.4 Discussion

One primary design feature of the ferromagnetic SiC/SiC CMCs proposed in this study was to have cobalt metal particles evenly dispersed in the SiC matrix. This was done by dissolving cobalt salts in the SiC-forming pre-ceramic polymer. After infiltrating into the SiC fibers, the polymer is pyrolyzed to SiC under H_2 and the cobalt salts are simultaneously reduced to cobalt metal. Three salts were attempted: cobalt (II) acetate, chloride, and bromide. The cobalt (II) acetate powder was not soluble in the polymer and settled to the bottom of the mixture container. A mixture such as this would have poor infiltration properties, limited by the size of the powder particles compared to the pore sizes of the fibers. There would likely be an uneven distribution of cobalt in the CMCs. Solubility of the salts was key for good infiltration and even cobalt distribution in the matrix. This property was exhibited by both $CoCl_2$ and $CoBr_2$.

Another fallback of cobalt (II) acetate would have been the reduction reaction byproduct. Due to the organic nature of the acetate anion, this reagent would likely leave behind excess

carbon in the matrix from the reduction. This carbon could be detrimental to the thermal, chemical, and mechanical properties of the SiC matrix. Reduction of $CoCl_2$ and $CoBr_2$ produces gaseous HCl and HBr, respectively. These byproducts will exit the CMC as exhaust during the pyrolysis. Although, the corrosive nature of these gases may lead to degradation of the CMC components.

The first indication that the cobalt salts were reduced to cobalt metal was seen by holding a permanent magnet close to the pyrolyzed samples. All samples clung to the magnet, which indicated that enough cobalt metal was present to produce a significant ferromagnetic effect. The presence of cobalt metal was also detected in the XRD spectra. The reflections between 44-50° loosely match with the FCC and HCP crystal structures of cobalt. For FCC, reflections are expected at 45.9° and 53.6°. For HCC, reflections are expected at 41.4°, 43.9°, and 47.3°. The fact that the reflections were stronger in the $CoCl_2$ sample suggested that this salt was more easily reduced and a larger percentage of the chloride precursor was converted to cobalt. However, this was contradicted by the EDS results, which showed a larger atomic ratio of halide/cobalt in the $CoCl_2$ sample. This higher ratio suggested more chlorine was present in the form of residual unreduced $CoCl_2$. The size and distribution of the cobalt particles were not measured. Interestingly, the samples containing cobalt salts both indicated the presence of Si_3N_4 based on the reflections around 21° and 31°. Since this was not seen from the standalone polymer, the cobalt salts or cobalt metal may be inducing the pre-ceramic polymer's ability to pyrolyze to Si_3N_4. Further tests would be needed to confirm this.

Oxidation testing of the ferromagnetic CMCs is important to see if the material maintains its magnetic properties under extreme conditions. CoO is known to exhibit ferromagnetism, so some oxidation of the cobalt particles may be acceptable. However, Co_3O_4 is antiferromagnetic

and will reduce the magnetic properties of the material if present [78]. Some oxidation protection is expected from the surrounding matrix, but more may be provided from EBCs. SiC and SiO_2 EBCs were applied to mini-composites and compared against an unprotected mini-composite. SiC is expected to oxidize to SiO_2 at high temperatures, which can provide protection from further oxidation. However, the conversion process to SiO_2 may lead to matrix cracking which can expose more surface in the matrix [10]. A SiO_2 layer will provide the same protection without the matrix cracking. Nevertheless, all samples exhibited ferromagnetism after the oxidation testing. Evidently, the matrix alone provided adequate protection for 10 hours of oxidation. Chemical and structural analysis of the oxidized samples was not performed, so the presence of cobalt oxides is unknown. More samples and testing would be required to find the limit of these materials.

5.5 Conclusions

Ferromagnetic SiC matrices were successfully synthesized using the SiC-forming KDT Ceraset® Polysilazane 20 pre-ceramic polymer mixed with $CoCl_2$ and $CoBr_2$. Heat treatment of the polymer solutions to 1000 °C under hydrogen simultaneously pyrolyzed the polymer to SiC and reduced the cobalt salts to cobalt metal. Mini-composites made from both polymer-salt solutions exhibited ferromagnetic properties when a permanent magnet was held close. XRD showed stronger cobalt reflections from the $CoCl_2$ system, but EDS showed that the $CoBr_2$ system had a lower atomic ratio of halide/cobalt. Samples maintained their ferromagnetism after being calcined in air at 1000 °C for 10 hours, even without EBCs. Further oxidation testing would be required to see the effects of SiC and SiO_2 EBCs that were applied. As of yet, it is unknown if ferromagnetic cobalt oxides were produced and helped to maintain the ferromagnetism after calcination.

Chapter 6

Future Work and Partial Studies

The studies I have described in this dissertation were successful in various ways, but could still benefit from more work to further corroborate the findings, explain certain observations, and/or reveal additional findings. I have also worked on multiple projects during my time at UConn which were not described in the previous chapters because additional results were needed to draw useful conclusions. Some of these partial studies, which show promise for the future of CMCs are outlined here. This chapter serves to advise future researchers how they may wish to continue the work I have started.

6.1 Smoother TiC Coatings

In **Chapter 2**, TiC coatings were deposited on carbon fibers to have a relatively smooth morphology. However, the optimized coating still exhibited some roughness and sooting which may be able to be overcome. Some of the smoothest and most uniform coatings were actually seen from the deposition at 1050 °C (**Figure 2.5**), but the deposition rate was too fast and fibers were bridged together.

One possible way to improve the rough coatings is by diluting the reaction gases further. Hydrogen was used as a carrier gas to deliver $TiCl_4$ vapors to the reaction tube. This hydrogen diluted the reaction to some extent, but this could not be controlled because increasing the hydrogen flow rate would also introduce more $TiCl_4$. An additional gas inlet for more hydrogen or an inert gas such as nitrogen or argon could be plumbed into the system for dilution of the reaction. This would decrease gas-phase interactions between $TiCl_4$ and CH_4 reaction gases, thereby reducing the formation of soot particles [35]. It would also slow down the reaction rate for depositing TiC on the fibers. This may make it possible to perform the depositions at higher temperatures to get a smoother coating without bridging fibers together. The flow rate of the diluting gas would be another parameter to optimize.

6.2 Protective Interphase Coatings

In **Chapter 3**, carbon fibers were coated with thin film interphase coatings to protect them during the silicon melt infiltration process. One of these coatings was TiC, which became damaged when heated to 1550 °C and left the carbon fibers vulnerable. This may have been from grain growth or further decomposition of the coating, which did not take place during the TiC CVI process. Additional research may be done to observe the crystallinity of the coatings before and after heat treatment using TEM and SAED. Thermogravimetric analysis in combination with mass spectrometry will show if further degradation is occurring, what temperature(s) it occurs at, and what species are being evolved. The suggestions in **Section 6.1** may circumvent this issue altogether.

Boron carbide may be another material of interest for protective coatings. Like TiC and SiC, it has a high stiffness and will likely embrittle the fibers. However, the high specific heat capacity of boron carbide would be quite beneficial to the overall CMC. Like BN, boron carbide will also lead to the formation of glassy borosilicate which can aid in oxidation protection of the fibers [10]. It would be useful to see how the boron carbide coatings produced in **Chapter 4** would hold up during the melt infiltration process.

This study would also benefit from additional characterization to see how silicon is interacting with the coatings. It was inconclusive whether silicon was reacting with or diffusing into the coatings. Raman spectroscopy and/or X-ray photoelectron spectroscopy (XPS) may be able to reveal the nature of the residual silicon in the samples.

6.3 Boron Carbide/Pyrolytic Carbon Matrix

In **Chapter 4**, carbon fibers were CVI coated using BCl_3 and CH_4 gases to try to reproduce results from a study that produced a mixed boron carbide and pyrolytic carbon matrix [61]. The goal was to better control the properties of the phases in the matrix by adjusting the CVI parameters. The deposited coatings contained boron, but the stoichiometry was not measured. Boron carbide is often notated as B_4C, but this representation is not always accurate because the stoichiometry lies on a spectrum depending on synthesis conditions [59]. EDS can be used to measure the atomic ratio of B:C in the various microstructures produced. This may be most effective alongside TEM where there is more control over the region of interest. EDS was used in this study, but the results are not considered conclusive because the analysis was applied across wide areas of the coating. Carbon signal may have been coming from boron carbide, pyC, or even the carbon fibers.

Pyrolytic carbon was not identified in the coatings. Further microscopy analysis may be used to search for grain boundaries separating boron carbide regions from pyC regions, as was seen in the literature. It may be possible to promote pyC deposition by increasing the partial pressure of CH_4 in the CVI process. When pyC is identified, the particular microstructure should be determined. This may be done using Raman spectroscopy [55]. In general, CVI parameters including temperature, pressure, and flow rates should be further tweaked to gain more insight into controlling the properties of the mixed matrix.

6.4 Ferromagnetic Silicon Carbide Matrix

In **Chapter 5**, CMCs with ferromagnetic matrices were prepared by dissolving cobalt salts in pre-ceramic polymer and reducing the salts to cobalt metal during the PIP process. Ferromagnetism was confirmed by holding a permanent magnet close to the CMCs and seeing that they are attracted. The use of a magnetometer would quantitatively measure the magnetic moment of the material. This should be done before and after oxidation testing, and oxidation testing should continue until the magnetic moment is no longer changing. This will also show how well the protective EBCs aid in oxidation resistance. Furthermore, the forms of cobalt in the material (Co, $CoCl_2$, $CoBr_2$, CoO, Co_3O_4, etc.) could be determined using a combination of Raman spectroscopy and XPS. Powder XRD was not completely useful in determining this during the study because the quantities of these components were low and they may not be crystalline in nature. The size and distribution of these particles may be determined using SEM and EDS.

The PIP parameters should be optimized by experimenting with different polymer-salt concentrations, pyrolysis temperatures, and pyrolysis times. The composition and structure of the ceramic matrix should be determined as well. The pre-ceramic polymer used supposedly produces SiC when pyrolyzed under inert gas or Si_3N_4 when pyrolyzed under NH_3. However, XRD reflections correlating to Si_3N_4 were identified in the matrices containing the cobalt salts despite the use of hydrogen during pyrolysis. It is possible that the cobalt salts are causing the polymer to form Si_3N_4 rather than SiC. The use of XRD, Raman spectroscopy, EDS, and/or XPS may clarify the nature of the pyrolyzed matrix.

6.5 Processing Considerations for Chemical Vapor Infiltrated BN Interphase Coatings

6.5.1 Introduction

Boron nitride is an excellent material for CMC interphase coatings. Hexagonal BN (h-BN) has the same structure as graphite, consisting of 2-D covalent networks stacked on top of one another. The BN layers, which are not covalently bonded together, are able to slide relatively easily to give the material its "solid state lubricant" properties. This ability provides control over the strength of the bond between fiber and matrix in CMCs and gives rise to multiple mechanisms for fracture toughness in the material [10]. Compared to pyrolytic carbon (pyC) interphase coatings, h-BN is resistant to oxidation to higher temperatures [79]. However, the chemical vapor infiltration (CVI) process for applying the BN coatings is highly sensitive to leaks introducing oxygen and moisture into the reaction. A large enough leak can result in an oxidized coating and a CMC with poor thermal and mechanical properties. Furthermore, fully hexagonal BN is difficult to produce using CVI [79]. BN with a turbostratic microstructure (t-BN) is typically deposited, meaning the 2-D BN layers are not perfectly aligned and contain disorder [80]. This form of BN is quite susceptible to oxidation from oxygen and moisture at room temperature, forming B_2O_3 on the coating surface. The crystallinity of turbostratic BN lies on a spectrum from fully amorphous to fully hexagonal. Maximizing this crystallinity minimizes the material's sensitivity to oxidation [81].

Air leaks in the CVI process can be minimized but not completely eliminated. Leaks are inherent to all piping and instrumentation connections, even when properly installed. Even in a perfectly sealed system, oxygen can enter by diffusing through the walls. It is important to know how bad the leaks are in a CVI system and how to minimize them. A common way of

determining this is by measuring the leak-up rate. The entire system is pumped down to its lowest possible pressure then the line to the pump is closed. Without the connection to the pump, the pressure of the system will gradually increase as air leaks in. The rate of this pressure change over time, normalized to the volume of the system (differential-pressure/time/volume), is the leak-up rate of the system. The concentration of oxygen in the reactor can also be measured directly using instrumentation such as a gas chromatographer (GC) or a residual gas analyzer (RGA). These measurements should be taken while the system is being pumped on and no other gases are flowing through so that oxygen and moisture are not diluted.

It has been previously reported that bulk t-BN made from the reaction between boric acid and ammonia can be further crystallized by post-annealing heat treatments [80]. Highly ordered h-BN planes were seen after annealing to 1800 °C. Udayakumar et al. [79] reported that the mechanical properties of BN coatings deposited from the BCl_3-NH_3 CVI process were improved from post-annealing to different temperatures. It would be useful to know how the crystallinity of t-BN improves from post-annealing to various temperatures and if this is influenced by the temperature of the CVI process.

Preliminary studies are reported here concerning the influence of air leaks during the CVI process and the influence of post-annealing heat treatments of BN coatings on crystallinity. Oxygen was purposefully "leaked" into the BN CVI reactor during deposition at various flow rates to see its effect on the coating. This was done with the goal of determining a threshold "leak" rate of oxygen in the system at which point the BN coating is too oxidized. Unoxidized BN coatings were also annealed to 1600 and 1800 °C in order to increase their crystallinity.

6.5.2 Experimental

A small-scale low pressure isothermal-isobaric CVI tube furnace reactor for BN deposition was assembled to investigate the influence of oxygen leaks. BCl_3 (chemically pure, 99.9%) and NH_3 (anhydrous, 99.99%) gases were used to form BN according to **Equation 3.3**. N_2 (ultra high purity, 99.999%) process gas was also used. The reaction took place in a 2.5 cm diameter quartz tube lined with graphite foil. The quartz tube ran through a single-zone horizontal tube furnace. Gas flow was regulated using digital mass flow controllers. BCl_3 and NH_3 were not mixed until reaching the quartz tube. Exhaust gases flowed through a liquid nitrogen cooled trap to condense solid byproducts. The rest of the gases were exhausted through an oil-lubricated mechanical pump. The pump allowed for low-pressure operation, but pressure was not actively controlled. CVI substrates were CG-Nicalon^{TM} SiC fiber tows. A diagram of the setup is shown in **Figure 6.1**.

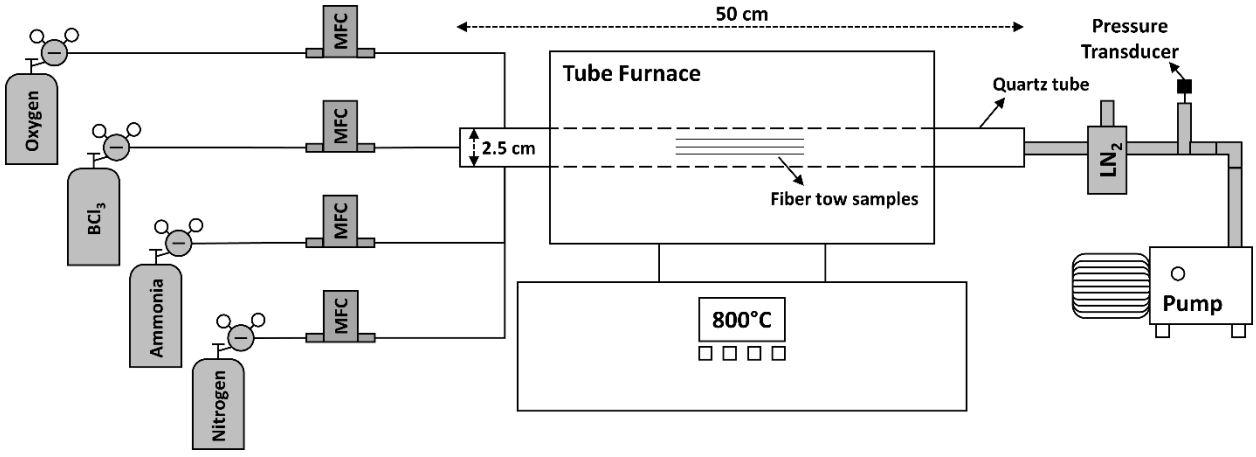

Figure 6.1 Diagram of BN CVI reactor used for investigating the effect of air leaks.

BN CVI parameters were optimized to produce smooth BN coatings on the SiC fibers. Leaks were then simulated in the process by flowing in a controlled amount of oxygen (ultra

high purity, 99.999%). Experiments were performed varying the mass flow rate of oxygen while keeping other CVI parameters constant. Oxygen flow rates were between 0-25 standard cubic centimeters per minute (sccm).

In a separate set of experiments, BN was CVI coated according to the process outlined in **Section 3.2.1** using the setup seen in **Figure 3.1**. A coating of SiC for environmental protection was also applied immediately following the BN CVI. Coatings were deposited on CG-Nicalon™ SiC fiber tow substrates. Post-annealing heat treatments were performed on coated fibers to 1600 and 1800 °C for 1 hour under nitrogen atmosphere.

Micrographs of the coated fibers were taken using a ThermoFisher TeneoLoVac Field Emission scanning electron microscope (SEM) operated at 10-20 kV and 0.4-1.6 nA. Diffraction patterns of the coated fibers were obtained using a Rigaku Ultima IV diffractometer (Cu Kα radiation, $\lambda = 1.5406$ Å) with an operating voltage of 40 kV and a current of 44 mA. Tensile testing of coated fibers was performed using an Instron® 5869 universal testing system equipped with a ±50 kN load cell at a rate of 0.5 cm/min. Tensile samples were mounted according to **Figure 2.3**. Coating thicknesses were factored into the tensile strength calculations.

6.5.3 Results

CVI conditions were optimized for the small scale CVI furnace (**Figure 6.1**) to produce baseline-quality BN coatings. The furnace temperature was 800 °C. BCl_3, NH_3, and N_2 flow rates were 12, 48, and 38 sccm, respectively. 30 min reaction times produced BN coatings ~200 nm thick. These coatings can be seen in **Figure 6.2a**. Coatings were smooth and consistent. Some gaps in coating were seen where adjacent fibers were touching. The coating was prone to flaking off from mechanical agitation where cross-sections were taken. Otherwise, the BN appeared to be well-adhered to the fibers.

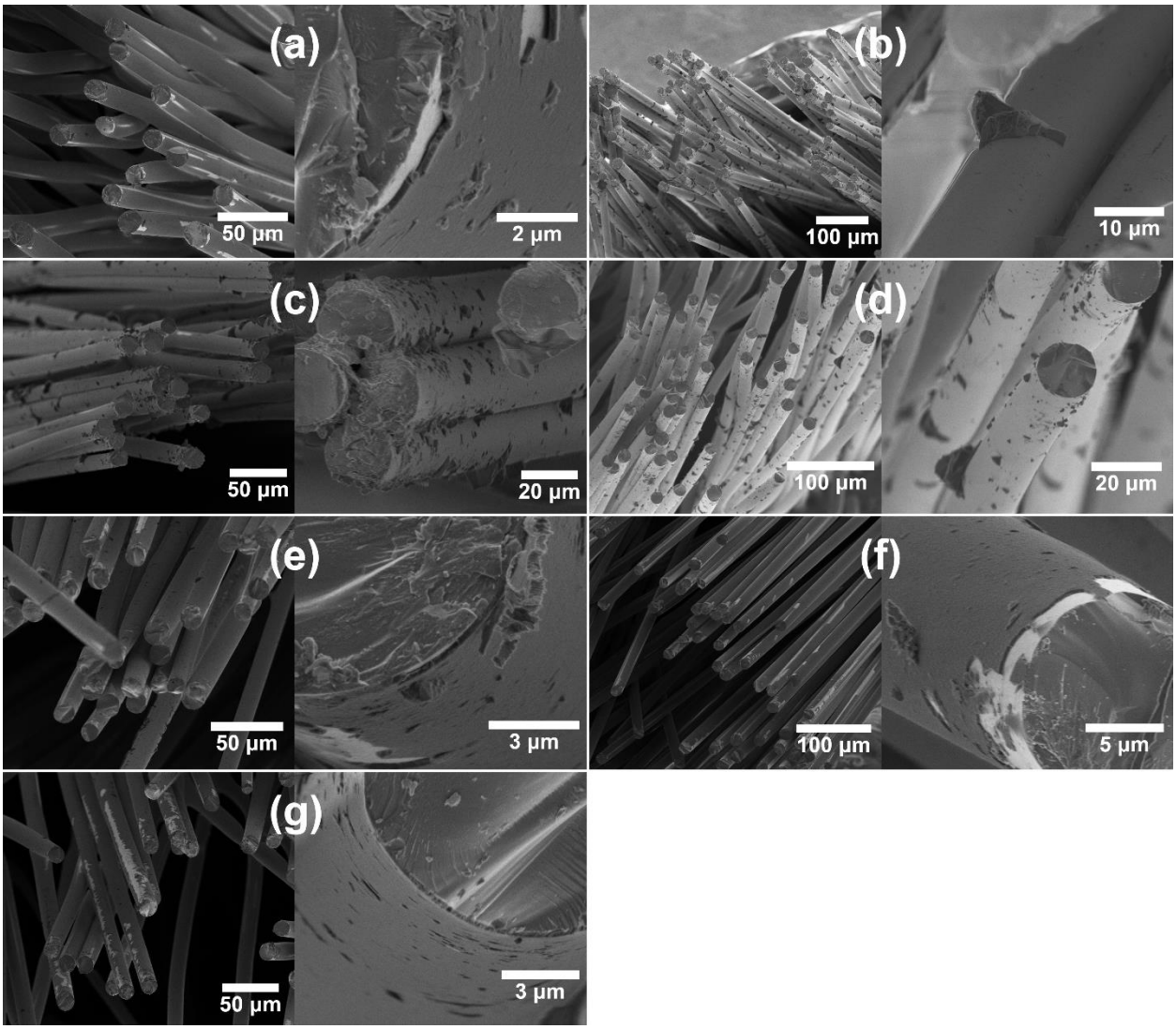

Figure 6.2 Micrographs of SiC fibers with oxidized BN coatings. Oxygen was leaked in at rates of (a) 0 sccm (b) 3 sccm (c) 5 sccm (d) 7 sccm (e) 10 sccm (f) 15 sccm (g) 25 sccm.

Oxygen contamination experiments were performed at 3, 5, 7, 10, 15, and 25 sccm oxygen, while still using all the parameters listed above. SEM was used to observe the quality of these contaminated coatings (**Figure 6.2b-g**). The introduction of oxygen resulted in the presence of particulates covering the fibers. A smooth coating was still applied to the fibers beneath the particulates. This was seen at all flow rates of oxygen, even as low as 3 sccm. The average tensile strengths of the coated fiber tows were measured and reported in **Figure 6.3**. The

flow of oxygen had little effect on the average tensile strengths below 15 sccm. Samples with 15 and 25 sccm flow rates of oxygen showed a reduction in strength.

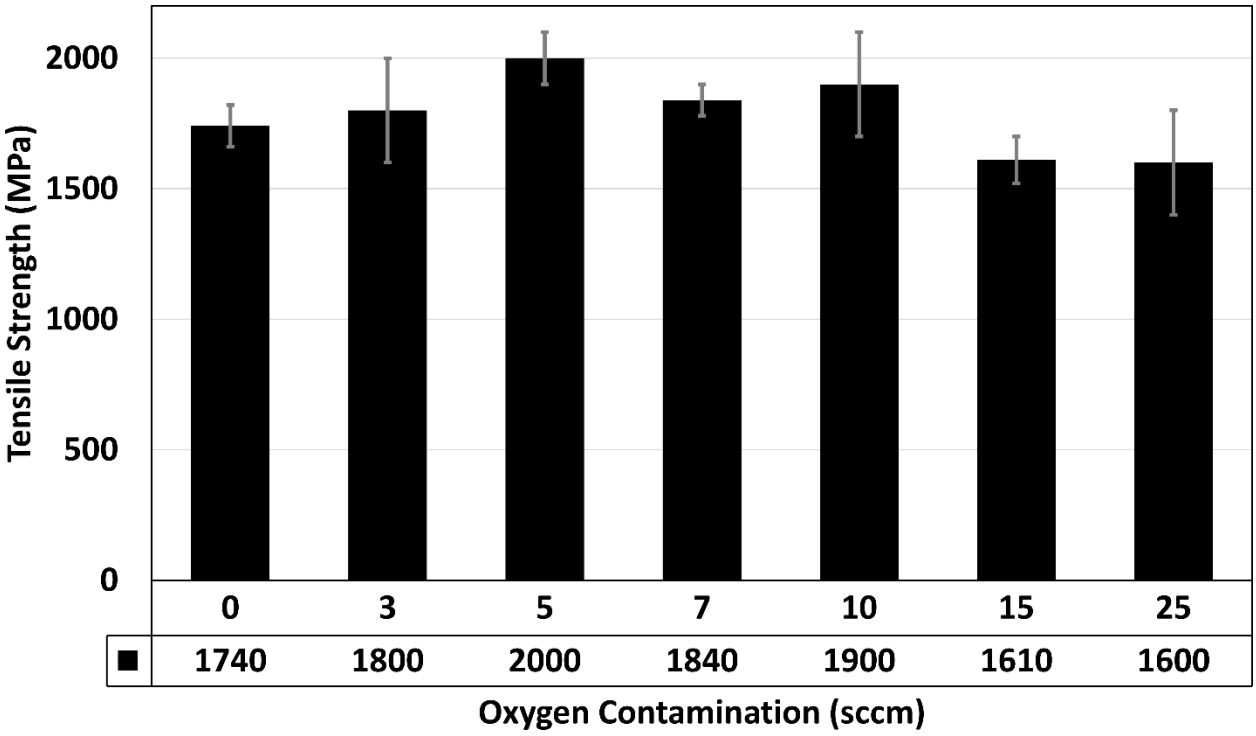

Figure 6.3 Average tensile strengths of SiC fibers coated with oxidized BN.

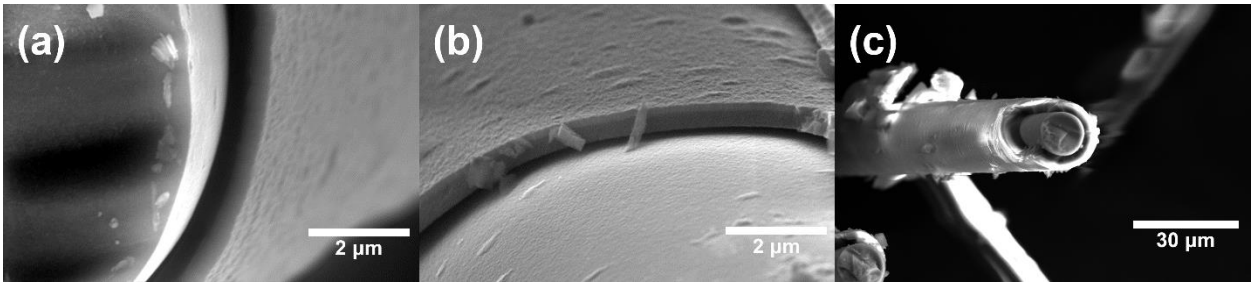

Figure 6.4 Micrographs of BN-SiC coated SiC fibers from the BN crystallization study. (a) ~350 nm BN coating before heat treatment. (b) ~350 nm BN coating after 1600 °C heat treatment. (c) ~4 µm BN coating before heat treatment.

BN-coated SiC fiber tows were prepared to investigate the effect of post-annealing heat treatments on BN crystallinity. The first set of samples had 300-400 nm of BN coating with 350-450 nm of CVI SiC on the outside for environmental protection. Some of the coated fiber tow was heat treated to 1600 °C for 1 hour under nitrogen. SEM images can be seen in **Figure 6.4**. No visual differences were seen in coating morphology between the as-received coatings and the heat treated coatings. Powder XRD was then performed on both samples. Diffraction patterns are shown in **Figure 6.5**. Sharp reflections were present in both patterns around 35°, 41°, 60°, 72°, and 75° due to the SiC fiber and coating. In the heat treated sample, a broad reflection with low intensity appeared between ~20-30°. These experiments were then repeated for a thicker coating of BN in order to strengthen the XRD signal from BN. This time about 4 μm of BN was deposited, as well as the 350-450 nm protective SiC layer. Micrographs of this coating can be seen in **Figure 6.4**. A sample from this run was heat treated to 1800 °C for 1 hour under nitrogen. Powder XRD patterns (**Figure 6.6**) of this set of samples had all the same reflections as the first set of samples. This time, the broad reflection in the heat-treated sample spanned ~23-28° and was slightly more intense.

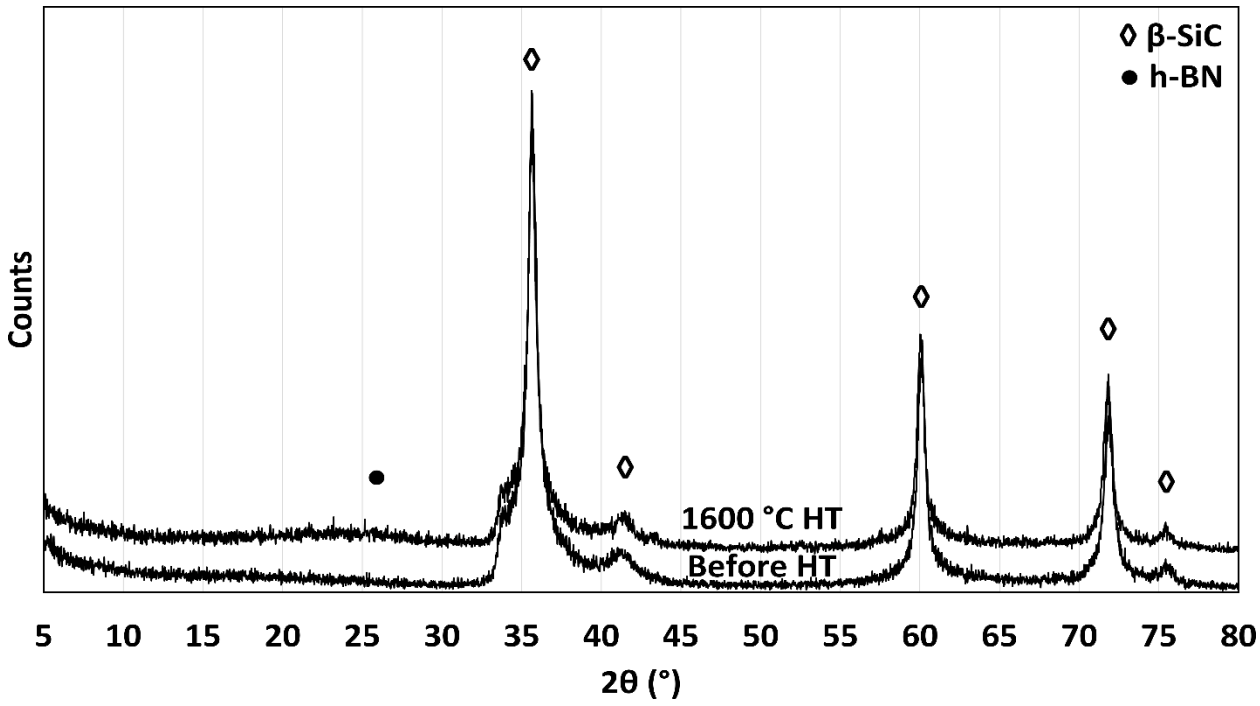

Figure 6.5 XRD patterns of SiC fiber coated with ~350 nm BN before and after 1600 °C heat treatment.

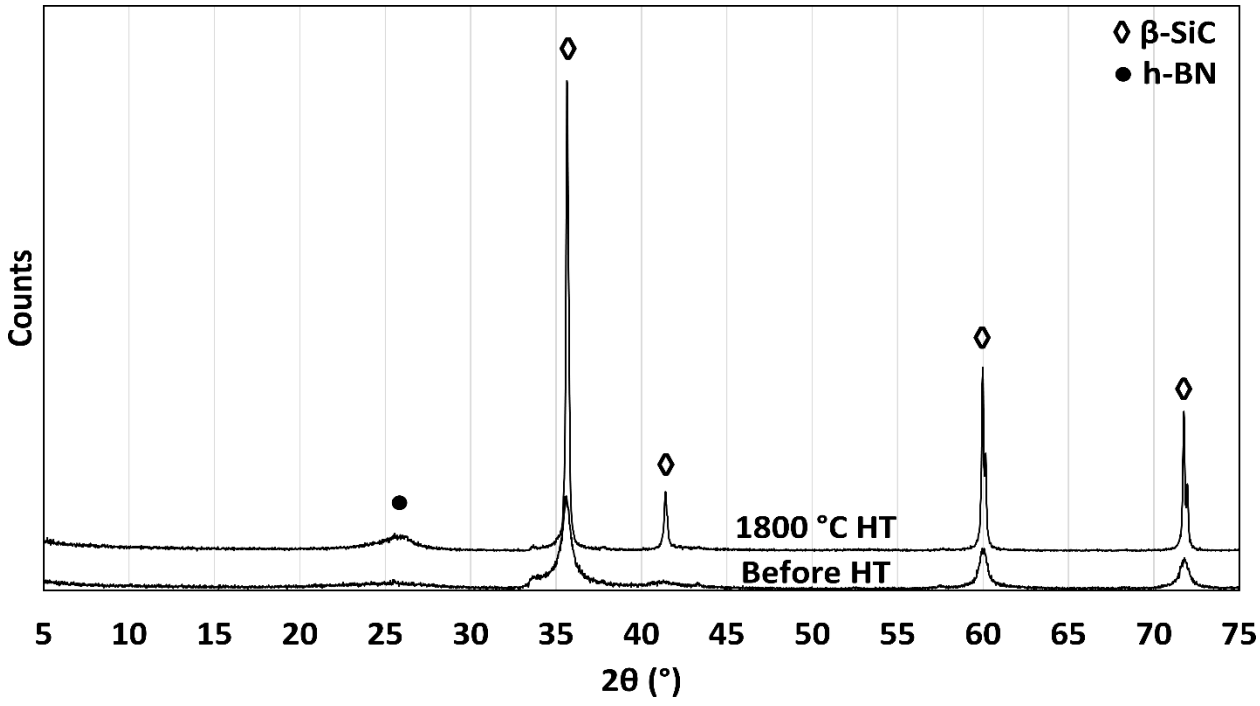

Figure 6.6 XRD patterns of SiC fiber coated with ~4 μm BN before and after 1800 °C heat treatment.

6.5.4 Discussion

Experiments investigating the effects of air leaks in the BN CVI process revealed that even small flows of oxygen (<5 sccm) can negatively impact the BN coating in a 2.5 cm tube reaction vessel. With no oxygen contamination (**Figure 6.2a**), the coatings were smooth with very few particulates seen on the surfaces of the coated fibers. The effect of the oxygen flow was visually obvious in the micrographs of the oxidized coatings. Much of the coated fiber surfaces were still relatively smooth, but they were also covered in soot particles, which could be seen without even magnifying to a single fiber. This is especially highlighted in **Figure 6.2b-d**, which had 3, 5, and 7 sccm oxygen during the CVI process, respectively. A close-up micrograph of one of these particles is seen in **Figure 6.2b**. It is likely that gas phase reactions are occurring between oxygen and BCl_3 to produce B_2O_3 solids, which then get deposited on the fibers. It is also possible for the oxygen to react with already deposited BN coatings, especially since they have a low degree of crystallinity before any post-annealing has been performed [81]. A process that promotes the crystallinity of the as-deposited BN may minimize this effect. Increased crystallinity has been achieved using multiple ways of adjusting and enhancing the CVI process such as promoting gas diffusion, depositing at higher temperatures, using the aid of EM radiation, and forming gas plasmas [9, 82-84].

Particular "success" has been seen in studies depositing fully hexagonal BN using plasma-assisted CVI [84-91]. Most of these studies were actually striving for the cubic BN phase for semiconductor applications and fell short by producing h-BN instead. The bulk of this research was conducted in the late 1990's, very little targeting high temperature CMC applications. This method needs to be applied to carbon and SiC fiber substrates. Degradation of the fibers is possible, but will never be understood if this research is not done.

Even though the coatings were significantly affected by low oxygen flow rates, the average tensile strengths of the coated fiber tows were not reduced until at least 15 sccm of oxygen was leaked in. This was attributed to oxidation of the fibers rather than the coatings. The fibers are meant to be the high-strength load bearing components of the CMC, not the coatings. A weak coating will not necessarily reduce the tensile strength of the fiber. Here, the coating and process gases may have been protecting the fiber from oxidation below oxygen flow rates of 15 sccm. Evidently, 15 sccm and higher was enough to oxidize the SiC fibers to a point that significantly reduced their tensile strengths.

3 sccm of oxygen "leaking" into the process may seem insignificant, but the scale of this setup is small. This amount may have much less impact on larger scale production furnaces which can be hundreds to thousands of times larger in volume and have much higher flow rates of gases. Here, there is just 12 sccm BCl_3 and 48 sccm NH_3. Even if most of the oxygen reacts with the ammonia, which is in excess, a good percentage of the BCl_3 may be oxidizing before it gets a chance to form BN. This is why leak rates must be normalized on a reactor-volume basis or even as a percentage of reaction gas flow rates. It would be helpful to determine the minimum leak rate of oxygen that will significantly affect the BN coating and be able to apply it to a wide range of CVI reaction scales. The effect of air humidity should be investigated as well, as BCl_3 and BN are also prone to oxidation from water. Reactor operators and engineers would be sure to minimize leaks to below this point before running the process.

For the BN post-annealing studies, SEM images did little more than confirm the presence of the coating and approximate its thickness (**Figure 6.4**). Heat treating to 1600 °C did not significantly alter the appearance of the BN, but it was important to confirm that the BN had not oxidized before or after the heat treatment from exposure to the atmosphere. In the first set of

samples, approximately 350 nm of BN was applied to the SiC fibers. In the XRD pattern for this pre-treated sample (**Figure 6.5**), BN reflections were not observed. This could be a result of the lack of crystallinity in the BN and/or the weak signal from the low percentage of BN in the powder sample compared to SiC. The pattern of the sample heat treated to 1600 °C shows a very subtle broad reflection from 20-30°. A h-BN reflection is expected at 26.6°, so this low-intensity reflection could indicate that BN crystallinity increased from the heat treatment. In the second set of samples, a much thicker BN layer was deposited with the hope of producing a stronger signal. In the pattern for the pre-treated sample (**Figure 6.6**) there was somewhat of a broad hump in the 20-30 range, but this peak was only just above the signal noise. Heat treatment to 1800 °C significantly sharpened and strengthened this signal, indicating further crystallization of the BN coating. The reflection was still very weak compared to the SiC reflections from the fibers, but it shows a large improvement from the heat treatment.

More is still to be learned about controlling the crystallinity of CVI BN coatings. Powder XRD provides weak signals from the BN due to dilution by the SiC. Grazing incidence XRD (GIXRD) may improve the BN contribution by focusing more on just the coating. Furthermore, the use of transmission electron microscopy (TEM) and selected-area electron diffraction (SAED) can completely isolate the BN. TEM images can be used to approximate the size of h-BN crystals and SAED can be used to measure the degree of crystallinity and preference of orientation. More work is needed to collect this data from heat treatments to other temperatures and for various durations of time. It would also be helpful to know how CVI reaction temperature affects the crystallinity of the as-deposited BN as well as its ability to crystalize further.

Since the time that this work was done, a study was published by Dai et al. on the effect of CVI temperature on BN crystallinity [9]. Depositions were performed at 843, 900, 950, and 1050 °C. TEM images and SAED patterns were presented to show that crystallinity of the BN steadily improved with higher deposition temperatures.

6.5.5 Conclusions

The CVI process to deposit coatings of BN is known to be sensitive to air leaks, which can prevent the formation of high-quality films. Oxygen was flowed in during the CVI reaction between 3-25 sccm to simulate air leaks and observe how the coatings were affected. All flow rates of oxygen produced coatings which were covered in soot particles, presumed to be B_2O_3 formed from the gas-phase reaction between BCl_3 and O_2. In order to determine the threshold leak rate of oxygen that will prevent a proper coating from being deposited, experiments with lower flow rates are required. The effect of moisture content in the leak should be investigated as well. Here, SEM was used as the primary form of characterization. Future studies should measure the oxygen content of the coatings. Auger electron spectroscopy with sputtering can be used to see how the oxygen content changes through the depth of the coating. GIXRD, TEM, and SAED should also be used to see how the crystallinity of the deposited coatings is affected by oxygen and moisture. These techniques are more quantitative than SEM alone and will help determine the maximum allowable leak rate.

Heat treatments of BN coatings following the CVI process were shown to increase the BN crystallinity. Heating a ~350 nm coating to 1600 °C for 1 hour under nitrogen resulted in a weak and broad reflection to appear around 20-30° in the XRD pattern. This effect was much more significant in a sample having ~4 μm of BN after heat treating to 1800 °C. Future studies should investigate a broader range of post-annealing temperatures and times. CVI temperature

should also be varied. Higher CVI temperatures have been shown to yield more crystalline BN coatings [9]. This may facilitate further crystallization in the post-annealing process. Powder XRD is not the most effective gauge of BN crystallinity here because most of the powder samples are made up of the SiC fibers. A combination of GIXRD, TEM, and SAED will more clearly show the effect of heat treatments on the coatings.

Fully hexagonal BN has been previously deposited using plasma-assisted CVI without the use of post-annealing heat treatments. This has been primarily demonstrated on silicon wafers for semiconductor use. Future researchers are strongly urged to pursue this method of h-BN deposition on carbon and SiC fibers. Many references are available outlining how this has been done [84-91].

6.6 Pyrophoric Byproducts Created from the SiC Chemical Vapor Infiltration Process

The most common process for CVI of SiC uses methyltrichlorsilane as a single-source precursor, as outlined in **Section 3.2.1**. At industrial sized scales, this process is known to produce a hazardous byproduct in large quantities, which builds up in the piping after the furnace. The material is said to be yellow and waxy. It oxidizes violently when doused with water and exhibits pyrophoricity when sudden shock is applied. This 'pyrophore' has caused multiple workplace injuries and viable solutions for handling the material have not been published. Very little information on this pyrophore is publicly available. Any information on its formation and recommended handling are proprietary trade secrets.

Based on the nature of the CVI reaction and what is known about other single-source CVI reactions, the pyrophore is likely a mixture of partially decomposed oligomeric chloro-silanes. In the CVI of pyC, hydrocarbon gases are used as single-source precursors. Reactions begin in the gas phase where lighter molecules like CH_4 abstract hydrogen atoms and merge into C2 species. Some of these C2's will react at the substrate surface and deposit pyC and some will continue reacting in the gas phase to form heavier hydrocarbons. The heavy hydrocarbons that do not deposit as pyC are exhausted out the reactor and condensed in cooler sections of the system [92]. I am theorizing that a similar mechanism is occurring with MTS in the CVI of SiC. The presence of residual chlorine groups in the pyrophore is what would make it reactive towards oxygen and moisture.

There is a great need for methods of mitigating pyrophore formation and/or safely denaturing it. Mitigation may be possible through optimization of the CVI parameters—temperature, pressure, and flow rates. However, most SiC CVI reactors in industry are specially tuned to produce the desired SiC material and cannot be easily adjusted. Alternatively, the

pyrophore could be condensed in a trap during the CVI process and heated to high temperatures (>1000 °C) afterwards to fully decompose it. There may also be ways of further decomposing the material through reaction with other gases. Caution is advised with this method, because large pyrophore deposits may build up an inert scale that shields the inner pyrophore from decomposing. This creates a very dangerous situation for whoever cleans out the plumbing afterwards.

References

[1] Hatta, H.; Weiss, R.; David, P. "Carbon/Carbons and Their Industrial Applications" pp. 87-146 in *Ceramic Matrix Composites: Materials, Modeling and Technology*. Eds. N. P. Bansal and J. Lamon. John Wiley & Sons, Inc. (2015).

[2] Heidenreich, B. "C/SiC and C/C-SiC Composites" pp. 147-216 in *Ceramic Matrix Composites: Materials, Modeling and Technology*. Eds. N. Bansal and J. Lamon. John Wiley & Sons, Inc. (2015).

[3] Keller, K. A.; Jefferson, G.; Kerans, R. J. "Oxide-Oxide Composites" pp. 236-272 in *Ceramic Matrix Composites: Materials, Modeling and Technology*. Eds. N. P. Bansal and J. Lamon. John Wiley & Sons, Inc. (2015).

[4] Fan, S.; Xu, Y.; Zhang, L.; Cheng, L.; Yu, L.; Yuan, Y.; Zhang, F.; Tian, G.; Chen, Z.; Lou, J. "Three-dimensional needled carbon/silicon carbide composites with high friction performance". *Materials Science and Engineering: A*. 467, 53-58 (2007).

[5] Xu, Y.; Zhang, Y.; Cheng, L.; Zhang, L.; Lou, J.; Zhang, J. "Preparation and friction behavior of carbon fiber reinforced silicon carbide matrix composites". *Ceramics international*. 33, 439-445 (2007).

[6] Xu, Y.; Cheng, L.; Zhang, L. "Carbon/silicon carbide composites prepared by chemical vapor infiltration combined with silicon melt infiltration". *Carbon*. 37, 1179-1187 (1999).

[7] Chen, L.; Yin, X.; Fan, X.; Chen, M.; Ma, X.; Cheng, L.; Zhang, L. "Mechanical and electromagnetic shielding properties of carbon fiber reinforced silicon carbide matrix composites". *Carbon*. 95, 10-19 (2015).

[8] Baklanova, N.; Zaitsev, B.; Titov, A.; Zima, T. "The chemistry, morphology, topography of titanium carbide modified carbon fibers". *Carbon*. 46, 261-271 (2008).

[9] Dai, J.; Wang, Y.; Xu, Z.; Mu, R.; He, L. "Effect of temperature on the growth of boron nitride interfacial coatings on SiC fibers by chemical vapor infiltration". *Ceramics International*. 45, 18556-18562 (2019).

[10] Piquero, T.; Vincent, H.; Vincent, C.; Bouix, J. "Influence of carbide coatings on the oxidation behavior of carbon fibers". *Carbon*. 33, 455-467 (1995).

[11] Hillig, W. B. "Melt infiltration approach to ceramic matrix composites". *Journal of the American Ceramic Society*. 71, C-96-C-99 (1988).

[12] Panerai, F.; Helber, B.; Chazot, O.; Balat-Pichelin, M. "Surface temperature jump beyond active oxidation of carbon/silicon carbide composites in extreme aerothermal conditions". *Carbon*. 71, 102-119 (2014).

[13] Kerans, R. J.; Hay, R. S.; Parthasarathy, T. A.; Cinibulk, M. K. "Interface design for oxidation-resistant ceramic composites". *Journal of the American Ceramic Society*. 85, 2599-2632 (2002).

[14] Aggour, L.; Fitzer, E.; Ignotowitz, E.; Sahebkar, M. "Chemical vapour deposition of pyro-carbon, SiC, TiC, TiN, Si and Ta on different types of carbon fibres". *Carbon*. 12, 358-362 (1974).

[15] Chang, Y. H.; Hsu, H. Y.; Yeh, J. H.; Chen, W. C.; Fu, Y. C.; Chiu, H. T. "Synthesis and Characterization of Carbon Fiber-Reinforced Silicon Carbide Composites with an Interlayer of Amorphous Carbon Thin Film Prepared by Precursor Infiltration and Pyrolysis Processes". *Advanced Engineering Materials*. 21, 1800583 (2019).

[16] Brennan, J. J. "Interfaces in BN coated fiber reinforced glass-ceramic matrix composites". *Scripta Metallurgica et Materialia;(United States)*. 31, (1994).

[17] Poges, S.; Monteleone, C.; Petroski, K.; Richards, G.; Suib, S. L. "Preparation and characterization of an oxide-oxide continuous fiber reinforced ceramic matrix composite with a zinc oxide interphase". *Ceramics International*. 43, 17121-17127 (2017).

[18] Kim, D. P.; Economy, J. "Fabrication of oxidation-resistant carbon fiber/boron nitride matrix composites". *Chemistry of materials*. 5, 1216-1220 (1993).

[19] Li, D.; Zhang, C.; Li, B.; Cao, F.; Wang, S.; Li, J. "Preparation and properties of unidirectional boron nitride fibre reinforced boron nitride matrix composites via precursor infiltration and pyrolysis route". *Materials Science and Engineering: A*. 528, 8169-8173 (2011).

[20] Reutenauer, J. W.; Coons, T. P.; Hill, C. L.; Arpin, K. A.; Kmetz, M. A.; Suib, S. L. "Synthesis and characterization of polyvinylsilazane as a precursor for Si 3 N 4 based ceramic materials". *Journal of materials science*. 46, 6538-6544 (2011).

[21] Petroski, K.; Poges, S.; Monteleone, C.; Grady, J.; Bhatt, R.; Suib, S. L. "Rapid Chemical Vapor Infiltration of Silicon Carbide Minicomposites at Atmospheric Pressure". *ACS applied materials & interfaces*. 10, 4986-4992 (2018).

[22] Jiang, J.; Wang, S.; Li, W.; Chen, Z. "Fabrication of Cf/ZrC–SiC composites using Zr–8.8 Si alloy by melt infiltration". *Ceramics International*. 41, 8488-8493 (2015).

[23] Peterlik, H. "Carbon Fibers" pp. 27-39 in *Ceramic Matrix Composites: Materials, Modeling and Technology*. Eds. N. P. Bansal and J. Lamon. John Wiley & Sons (2015).

[24] Shirvanimoghaddam, K.; Hamim, S. U.; Akbari, M. K.; Fakhrhoseini, S. M.; Khayyam, H.; Pakseresht, A. H.; Ghasali, E.; Zabet, M.; Munir, K. S.; Jia, S. "Carbon fiber reinforced metal matrix composites: Fabrication processes and properties". *Composites Part A: Applied Science and Manufacturing*. 92, 70-96 (2017).

[25] Tang, S.; Hu, C. "Design, preparation and properties of carbon fiber reinforced ultra-high temperature ceramic composites for aerospace applications: a review". *Journal of Materials Science & Technology*. 33, 117-130 (2017).

[26] Yao, S.-S.; Jin, F.-L.; Rhee, K. Y.; Hui, D.; Park, S.-J. "Recent advances in carbon-fiber-reinforced thermoplastic composites: a review". *Composites Part B: Engineering*. 142, 241-250 (2018).

[27] Pierson, H. O. "*Handbook of Refractory Carbides & Nitrides: Properties, Characteristics, Processing and Apps*". William Andrew, 1996. Print.

[28] Dong, Z.; Li, X.; Yuan, G.; Cui, Z.; Cong, Y.; Westwood, A. "Tensile strength, oxidation resistance and wettability of carbon fibers coated with a TiC layer using a molten salt method". *Materials & Design*. 50, 156-164 (2013).

[29] Wang, K.; Li, M.; Liang, Y.; Wang, J.; He, L.; Du, S.; Huang, Z.; Huang, Q. "Interface modification of carbon fibers with TiC/Ti2AlC coating and its effect on the tensile strength". *Ceramics International*. 45, 4661-4666 (2019).

[30] Girolami, G. S.; Jensen, J. A.; Pollina, D. M.; Allocca, C. M.; Kaloyeros, A. E.; Williams, W. S. "Organometallic route to the chemical vapor deposition of titanium carbide films at exceptionally low temperatures". *Journal of the American Chemical Society*. 109, 1579-1580 (1987).

[31] Kato, A.; Yasunaga, M.; Tamari, N. "Growth rate of titanium carbide whiskers in chemical vapor deposition". *Journal of Crystal Growth*. 37, 293-300 (1977).

[32] Li, X.; Dong, Z.; Westwood, A.; Brown, A.; Zhang, S.; Brydson, R.; Li, N.; Rand, B. "Preparation of a titanium carbide coating on carbon fibre using a molten salt method". *Carbon*. 46, 305-309 (2008).

[33] "Standard X-ray Diffraction Powder Patterns". Monograph 2518, 73 (1981).

[34] Lamon, J. "Influence of Interfaces and Interphases on the Mechanical Behavior of Fiber-Reinforced Ceramic Matrix Composites" pp. 40-64 in *Ceramic Matric Composites: Materials, Modeling and Technology*. Eds. N. P. Bansal and J. Lamon. John Wiley & Sons (2015).

[35] Pierson, H. O. "*Handbook of chemical vapor deposition: principles, technology and applications*". William Andrew, 1999. Print.

[36] Lespiaux, D.; Langlais, F.; Naslain, R.; Schamm, S.; Sevely, J. "Correlations between gas phase supersaturation, nucleation process and physico-chemical characteristics of silicon carbide deposited from Si-CH-Cl system on silica substrates". *Journal of materials science*. 30, 1500-1510 (1995).

[37] Bian, G.; Wu, H. "Friction performance of carbon/silicon carbide ceramic composite brakes in ambient air and water spray environment". *Tribology International*. 92, 1-11 (2015).

[38] Oh, B. J.; Lee, Y. J.; Choi, D. J.; Hong, G. W.; Park, J. Y.; Kim, W. J. "Fabrication of carbon/silicon carbide composites by isothermal chemical vapor infiltration, using the in situ whisker-growing and matrix-filling process". *Journal of the American Ceramic Society*. 84, 245-247 (2001).

[39] Coons, T. P.; Reutenauer, J. W.; Flandermeyer, B.; Kmetz, M. A.; Prevost, E.; Suib, S. L. "An investigation into a multilayered BN/Si 3 N 4/BN interfacial coating". *Journal of materials science*. 48, 6194-6202 (2013).

[40] Naslain, R.; Dugne, O.; Guette, A.; Sevely, J.; Brosse, C. R.; Rocher, J. P.; Cotteret, J. "Boron nitride interphase in ceramic-matrix composites". *Journal of the American Ceramic Society*. 74, 2482-2488 (1991).

[41] Monteleone, C.; Poges, S.; Petroski, K.; Kerns, P.; Tobin, Z.; Policandriotes, T.; Suib, S. L. "Atmospheric pressure chemical vapor infiltration of a titanium carbide interphase coating on carbon fiber". *Ceramics International*. (2020).

[42] Sun, Z. "Progress in research and development on MAX phases: a family of layered ternary compounds". *International Materials Reviews*. 56, 143-166 (2011).

[43] Toray Composite Materials America Inc. *T300 Datasheet*. Rev. 6 (April 13, 2018).

[44] Yang, M.; SUN, J.-l.; REN, M.-s.; LI, H.; BAI, R.-c. "Nanohardness and Elastic Modulus of Pyrocarbon [J]". *Journal of Shanghai University (Natural Science Edition)*. 5, (2008).

[45] Fu, X.-a.; Dunning, J. L.; Zorman, C. A.; Mehregany, M. "Measurement of residual stress and elastic modulus of polycrystalline 3C-SiC films deposited by low-pressure chemical vapor deposition". *Thin Solid Films*. 492, 195-202 (2005).

[46] Chang, R.; Graham, L. J. "Low-temperature elastic properties of ZrC and TiC". *Journal of Applied Physics*. 37, 3778-3783 (1966).

[47] Weissmantel, S.; Reisse, G.; Keiper, B.; Schulze, S. "Microstructure and mechanical properties of pulsed laser deposited boron nitride films". *Diamond and Related Materials*. 8, 377-381 (1999).

[48] Hopcroft, M. A.; Nix, W. D.; Kenny, T. W. "What is the Young's Modulus of Silicon?". *Journal of microelectromechanical systems*. 19, 229-238 (2010).

[49] Drevet, B.; Eustathopoulos, N. "Wetting of ceramics by molten silicon and silicon alloys: a review". *Journal of Materials Science*. 47, 8247-8260 (2012).

[50] Zhang, D.; Li, K.; Li, H.; Jia, Y.; Guo, L.; Li, H. "Coefficients of thermal expansion of low texture and isotropic pyrocarbon deposited on stationary substrates". *Materials Letters*. 68, 68-70 (2012).

[51] Shackelford, J. F.; Han, Y.-H.; Kim, S.; Kwon, S.-H. "*CRC materials science and engineering handbook*". CRC press, 2016. Print.

[52] Yu, S.; Zhang, F.; Xiong, X.; Li, Y.; Tang, N.; Koizumi, Y.; Chiba, A. "Tribological properties of carbon/carbon composites with various pyrolytic carbon microstructures". *Wear*. 304, 103-108 (2013).

[53] Oberlin, A. "Pyrocarbons". *Carbon*. 40, 7-24 (2002).

[54] Vignoles, G.; Pailler, R.; Teyssandier, F. "The control of interphases in carbon and ceramic matrix composites". *Advanced Processing and Manufacturing Technologies for Structural and Multifunctional Materials VI*. 33, 11-23 (2012).

[55] Bourrat, X. "Pyrocarbon performances and characterization". (2009).

[56] Zhang, M.; Su, Z.; Xie, Z.; Chen, J.; Huang, Q. "Microstructure of pyrocarbon with chemical vapor infiltration". *Procedia Engineering*. 27, 847-854 (2012).

[57] Li, S.; Zeng, B.; Feng, Z.; Liu, Y.; Yang, W.; Zhang, L. "Effects of heat treatment on the microstructure of amorphous boron carbide coating deposited on graphite substrates by chemical vapor deposition". *Thin Solid Films*. 519, 251-258 (2010).

[58] Sezer, A. O.; Brand, J. "Chemical vapor deposition of boron carbide". *Materials Science and Engineering: B*. 79, 191-202 (2001).

[59] Suri, A.; Subramanian, C.; Sonber, J.; Murthy, T. C. "Synthesis and consolidation of boron carbide: a review". *International Materials Reviews*. 55, 4-40 (2010).

[60] Tallant, D.; Aselage, T.; Campbell, A.; Emin, D. "Boron carbide structure by Raman spectroscopy". *Physical review B*. 40, 5649 (1989).

[61] Zeng, B.; Feng, Z.; Li, S.; Liu, Y.; Cheng, L.; Zhang, L. "Microstructure and deposition mechanism of CVD amorphous boron carbide coatings deposited on SiC substrates at low temperature". *Ceramics International*. 35, 1877-1882 (2009).

[62] Sanc, I. "Pattern: 00-041-1478, Graphite-2H, Polytechna". *Foreign Trade Corporation, Panska, Czechoslovakia, ICDD Grant-in-Aid*. (1990).

[63] Hanawalt, J.; Rinn, H.; Frevel, L. "Chemical analysis by X-ray diffraction". *Industrial & Engineering Chemistry Analytical Edition*. 10, 457-512 (1938).

[64] Ashley, S. "Turbines on a dime". *Mechanical Engineering*. 119, 78 (1997).

[65] Hauser, R.; Francis, A.; Theismann, R.; Riedel, R. "Processing and magnetic properties of metal-containing SiCN ceramic micro-and nano-composites". *Journal of materials science*. 43, 4042-4049 (2008).

[66] Liew, L.; Zhang, W.; An, L.; Shah, S.; Luo, R.; Liu, Y.; Cross, T.; Dunn, M. L.; Bright, V.; Daily, J. W. "Ceramic MEMS". *American Ceramic Society Bulletin*. 80, 25 (2000).

[67] Yurkov, G. Y.; Shashkeev, K. A.; Kondrashov, S. V.; Popkov, O. V.; Shcherbakova, G. I.; Zhigalov, D. V.; Pankratov, D. A.; Ovchenkov, E. A.; Koksharov, Y. A. "Synthesis and magnetic properties of cobalt ferrite nanoparticles in polycarbosilane ceramic matrix". *Journal of Alloys and Compounds*. 686, 421-430 (2016).

[68] Fathy, A.; El-Kady, O.; Mohammed, M. M. "Effect of iron addition on microstructure, mechanical and magnetic properties of Al-matrix composite produced by powder metallurgy route". *Transactions of Nonferrous Metals Society of China*. 25, 46-53 (2015).

[69] Stabik, J.; Chrobak, A.; Haneczok, G.; Dybowska, A. "Magnetic properties of polymer matrix composites filled with ferrite powders". *Archives of Materials Science*. 98, 98 (2011).

[70] Kulbaba, K.; Resendes, R.; Cheng, A.; Bartole, A.; Safa-Sefat, A.; Coombs, N.; Stöver, H. D.; Greedan, J. E.; Ozin, G. A.; Manners, I. "Polyferrocenylsilane and magnetic ceramic microspheres". *Advanced Materials*. 13, 732-736 (2001).

[71] MacLachlan, M. J.; Ginzburg, M.; Coombs, N.; Coyle, T. W.; Raju, N. P.; Greedan, J. E.; Ozin, G. A.; Manners, I. "Shaped ceramics with tunable magnetic properties from metal-containing polymers". *Science*. 287, 1460-1463 (2000).

[72] Saha, A.; Shah, S. R.; Raj, R.; Russek, S. E. "Polymer-derived SiCN composites with magnetic properties". *Journal of materials research*. 18, 2549-2551 (2003).

[73] Szafran, M.; Konopka, K.; Bobryk, E.; Kurzydłowski, K. "Ceramic matrix composites with gradient concentration of metal particles". *Journal of the European Ceramic Society*. 27, 651-654 (2007).

[74] Gottlieb, R. E. "Advancements in Fiber, Interface, and Matrix Materials for Ceramic Matrix Composites". (2016).

[75] Kmetz, M. A.; Richards, G. C.; Suib, S. L.; Gottlieb, R. E. "Magnetic material and method therefor". (2015).

[76] Enghag, P. "*Encyclopedia of the elements: technical data-history-processing-applications*". John Wiley & Sons, 2008. Print.

[77] KION Defense Technologies Inc. *KDT Ceraset Polysilazane 20 Technical Data Sheet*. Accessed 2020 (http://www.industrycortex.com/datasheets/profile/1252255221).

[78] Zhang, D.; Zhu, J.; Zhang, N.; Liu, T.; Chen, L.; Liu, X.; Ma, R.; Zhang, H.; Qiu, G. "Controllable fabrication and magnetic properties of double-shell cobalt oxides hollow particles". *Scientific reports*. 5, 8737 (2015).

[79] Udayakumar, A.; Ganesh, A. S.; Raja, S.; Balasubramanian, M. "Effect of intermediate heat treatment on mechanical properties of SiCf/SiC composites with BN interphase prepared by ICVI". *Journal of the European Ceramic Society*. 31, 1145-1153 (2011).

[80] Alkoy, S.; Toy, C.; Gönül, T.; Tekin, A. "Crystallization behavior and characterization of turbostratic boron nitride". *Journal of the European Ceramic Society*. 17, 1415-1422 (1997).

[81] Le Gallet, S.; Rebillat, F.; Guette, A.; Naslain, R. "Oxidation resistance of CVD BN coatings: correlation with processing conditions and with precursor gas systems". (2001).

[82] Leparoux, M.; Vandenbulcke, L.; Clinard, C. "Influence of isothermal chemical vapor deposition and chemical vapor infiltration conditions on the deposition kinetics and structure of boron nitride". *Journal of the American Ceramic Society*. 82, 1187-1195 (1999).

[83] Misra, D.; Nemane, V.; Mukhopadhyay, S.; Chatterjee, S. "Effect of hBN and SiC addition on laser assisted processing of ceramic matrix composite coatings". *Ceramics International*. (2019).

[84] Rossi, F.; Schaffnit, C.; Thomas, L.; Del Puppo, H.; Hugon, R. "Plasma assisted chemical vapour deposition of boron nitride coatings from using BCl3–N2–H2–Ar gas mixture". *Vacuum*. 52, 169-181 (1999).

[85] Berns, D.; Cappelli, M. "Low energy ion impact-enhanced growth of cubic boron nitride in a supersonic nitrogen/argon plasma flow". *Journal of materials research*. 12, 2014-2026 (1997).

[86] Carreno, M.; Bottecchia, J.; Pereyra, I. "Low temperature plasma enhanced chemical vapour deposition boron nitride". *Thin Solid Films*. 308, 219-222 (1997).

[87] Chen, G.; Zhang, X.; Wang, B.; Yan, H. "The effects of substrate bias voltage and radio-frequency power on the growth of c-BN phase coatings". *Surface and Coatings Technology*. 113, 25-30 (1999).

[88] Durmazuçar, H. H.; Gündüz, G.; Toker, C. "Microstructure of boron nitride coated on nuclear fuels by plasma enhanced chemical vapor deposition". *Journal of nuclear materials*. 256, 207-212 (1998).

[89] Lang, N.; Hempel, F.; Strämke, S.; Röpcke, J. "Time-resolved quantum cascade laser absorption spectroscopy of pulsed plasma assisted chemical vapor deposition processes containing BCl3". *Japanese Journal of Applied Physics*. 50, 08JB04 (2011).

[90] Schaffnit, C.; Del Puppo, H.; Hugon, R.; Thomas, L.; Moretto, P.; Rossi, F.; Pauleau, Y. "Effect of H2 concentration on rf plasma-enhanced chemical vapour deposition of boron nitride coatings from the BCl3-N2-H2-Ar gas system". *Surface and Coatings Technology*. 80, 13-17 (1996).

[91] Schaffnit, C.; Thomas, L.; Rossi, F.; Hugon, R.; Pauleau, Y. "Plasma diagnostics of rf PACVD of boron nitride using a BCl3− N2− H2− Ar gas mixture". *Surface and Coatings Technology*. 98, 1262-1266 (1998).

[92] Delhaes, P. "Chemical vapor deposition and infiltration processes of carbon materials". *carbon*. 40, 641-657 (2002).